Landslide generated tsunamis - Numerical modeling and real-time prediction

Dissertation

zur Erlangung des akademischen Grades

Doktor der Naturwissenschaften (Dr. rer. nat.)

in der Wissenschaftsdisziplin Geophysik

eingereicht an der Mathematisch-Naturwissenschaftlichen Fakultät

der Universität Potsdam

vorgelegt von

Sascha Brune

Potsdam, den 29. Januar 2009

Abstract

Submarine landslides can generate local tsunamis posing a hazard to human lives and coastal facilities. Two major related problems are: (i) quantitative estimation of tsunami hazard and (ii) early detection of the most dangerous landslides. This thesis focuses on both those issues by providing numerical modeling of landslide-induced tsunamis and by suggesting and justifying a new method for fast detection of tsunamigenic landslides by means of tiltmeters.

Due to the proximity to the Sunda subduction zone, Indonesian coasts are prone to earthquake, but also landslide tsunamis. The aim of the GITEWS-project (German-Indonesian Tsunami Early Warning System) is to provide fast and reliable tsunami warnings, but also to deepen the knowledge about tsunami hazards. New bathymetric data at the Sunda Arc provide the opportunity to evaluate the hazard potential of landslide tsunamis for the adjacent Indonesian islands. I present nine large mass movements in proximity to Sumatra, Java, Sumbawa and Sumba, whereof the largest event displaced 20 km³ of sediments. Using numerical modeling, I compute the generated tsunami of each event, its propagation and run-up at the coast. Moreover, I investigate the age of the largest slope failures by relating them to the Great 1977 Sumba earthquake.

Continental slopes off northwest Europe are well known for their history of huge underwater landslides. The current geological situation west of Spitsbergen is comparable to the continental margin off Norway after the last glaciation, when the large tsunamigenic Storegga slide took place. The influence of Arctic warming on the stability of the Svalbard glacial margin is discussed. Based on new geophysical data, I present four possible landslide scenarios and compute the generated tsunamis. Waves of 6 m height would be capable of reaching northwest Europe threatening coastal areas.

I present a novel technique to detect large submarine landslides using an array of tiltmeters, as a possible tool in future tsunami early warning systems. The dislocation of a large amount of sediment during a landslide produces a permanent elastic response of the earth. I analyze this response with a mathematical model and calculate the theoretical tilt signal. Applications to the hypothetical Spitsbergen event and the historical Storegga slide show tilt signals exceeding 1000 nrad.

The amplitude of landslide tsunamis is controlled by the product of slide volume and maximal velocity (slide tsunamigenic potential). I introduce an inversion routine that provides slide location and tsunamigenic potential, based on tiltmeter

measurements. The accuracy of the inversion and of the estimated tsunami height near the coast depends on the noise level of tiltmeter measurements, the distance of tiltmeters from the slide, and the slide tsunamigenic potential. Finally, I estimate the applicability scope of this method by employing it to known landslide events worldwide.

Zusammenfassung

Submarine Erdrutsche können lokale Tsunamis auslösen und stellen somit eine Gefahr für Siedlungen an der Küste und deren Einwohner dar. Zwei Hauptprobleme sind (i) die quantitative Abschätzung der Gefahr, die von einem Tsunami ausgeht und (ii) das schnelle Erkennen von gefährlichen Rutschungsereignissen. In dieser Doktorarbeit beschäftige ich mich mit beiden Problemen, indem ich Erdrutschtsunamis numerisch modelliere und eine neue Methode vorstelle, in der submarine Erdrutsche mit Hilfe von Tiltmetern detektiert werden.

Die Küstengebiete Indonesiens sind wegen der Nähe zur Sunda-Subduktionszone besonders durch Tsunamis gefährdet. Das Ziel des GITEWS-Projektes (Deutsch-Indonesisches Tsunami-Frühwarnsystem) ist es, schnell und verlässlich vor Tsunamis zu warnen, aber auch das Wissen über Tsunamis und ihre Anregung zu vertiefen. Neue bathymetrische Daten am Sundabogen bieten die Möglichkeit, das Gefahrenpotential von Erdrutschtsunamis für die anliegenden indonesischen Inseln zu studieren. Ich präsentiere neun große Rutschungereignisse nahe Sumatra, Java, Sumbawa und Sumba, wobei das größte von ihnen 20 km³ Sediment bewegte. Ich modelliere die Ausbreitung und die Überschwemmung der bei diesen Rutschungen angeregten Tsunamis. Weiterhin untersuche ich das Alter der größten Hanginstabilitäten, indem ich sie zu dem Sumba Erdbeben von 1977 in Beziehung setze.

Die Kontinentalhänge im Nordwesten Europa sind für Ihre immensen unterseeischen Rutschungen bekannt. Die gegenwärtige geologische Situation westlich von Spitzbergen ist vergleichbar mit derjenigen des norwegischen Kontinentalhangs nach der letzten Vergletscherung, als der große Tsunami-anregende Storegga-Erdrutsch stattfand. Der Einfluss der arktischen Erwärmung auf die Hangstabilität vor Spitzbergen wird untersucht. Basierend auf neuen geophysikalischen Messungen, konstruiere ich vier mögliche Rutschungsszenarien und berechne die entsprechenden Tsunamis. Wellen von 6 Metern Höhe könnten dabei Nordwesteuropa erreichen.

Ich stelle eine neue Methode vor, mit der große submarine Erdrutsche mit Hilfe eines Netzes aus Tiltmetern erkannt werden können. Diese Methode könnte in einem Tsunami-Frühwarnsystem angewendet werden. Sie basiert darauf, dass die Bewegung von großen Sedimentmassen während einer Rutschung eine dauerhafte Verformung der Erdoberfläche auslöst. Ich berechne diese Verformung und das einhergehende Tiltsignal. Im Falle der hypothetischen Spitzbergen-Rutschung sowie für das Storegga-Ereignis erhalte ich Amplituden von mehr als 1000 nrad.

Die Wellenhöhe von Erdrutschtsunamis wird in erster Linie von dem Produkt aus Volumen und maximaler Rutschungsgeschwindigkeit (dem Tsunamipotential einer Rutschung) bestimmt. Ich führe eine Inversionsroutine vor, die unter Verwendung von Tiltdaten den Ort und das Tsunamipotential einer Rutschung bestimmt. Die Genauigkeit dieser Inversion und damit der vorhergesagten Wellenhöhe an der Küste hängt von dem Fehler der Tiltdaten, der Entfernung zwischen Tiltmeter und Rutschung sowie vom Tsunamipotential ab. Letztlich bestimme ich die Anwendbarkeitsreichweite dieser Methode, indem ich sie auf bekannte Rutschungsereignisse weltweit beziehe.

Contents

Chapter 1

Introduction

Tsunamis are water waves that are generated, when a significant body of water is rapidly displaced. This can be caused by submarine earthquakes, landslides, volcanic eruptions or asteroid impacts. The immense amount of energy that is involved in tsunami generation, propagation and run-up can have devastating effects on coastal communities.

Most tsunamis are induced at submarine convergent plate boundaries. Here, tectonic stresses are accumulated due to relative plate motion. During an earthquake, relaxation occurs instantaneously deforming the sea bottom. This results in uplift of the oceanic water column at certain places and in subsidence at others. Leveling of the ocean surface due to gravity transforms the potential energy of the water into kinetic energy, thereby creating a propagating wave field, the tsunami. Destructive earthquake-generated tsunamis took place in historic and recent times: In 1755, Lisbon was devastated by an earthquake and the following tsunami (Baptista et al. 1998). The Aleutian Island earthquake of 1946 excited a tsunami that led to large damages in Alaska and Hawaii (Okal et al. 2003). In 1960, the Chilean earthquake, with M_w=9.5 (USGS) the largest ever recorded seismic event, generated an ocean-wide tsunami that caused casualties in Chile, Hawaii, the Philippines and Japan (Barrientos and Ward 1990). In the Indian Ocean, the tsunami of the M_w=9.3 (Stein and Okal 2005) Sumatra-Andaman earthquake of 2004 led to huge damages and loss of life in Indonesia, Thailand, Sri Lanka and India, but also affected the Maldives, Somalia and Madagascar (Synolakis and Kong 2006).

Although many tsunamis can be associated with submarine earthquakes, a significant number of tsunamis (8 %; following the 2007 ITDB catalogue) is induced by submarine landslides. The term landslide hereby comprises all kinds of submarine mass movements: rotational slumps, translational mudflows and turbidity currents; for a short overview see Trifunac and Todorovska (2002). Several tsunamis of the 20th century could be attributed to landslides: In 1929, an earthquake off Newfoundland (M_s=7.2) triggered a large (200 km³) submarine slope failure that generated a tsunami with run-ups of at least 12 m (Hasegawa and Kanamori 1987; Trifunac et al. 2002). In the Mediterranean, landslide-generated tsunamis damaged coastal structures and claimed casualties in the Corinth Gulf,
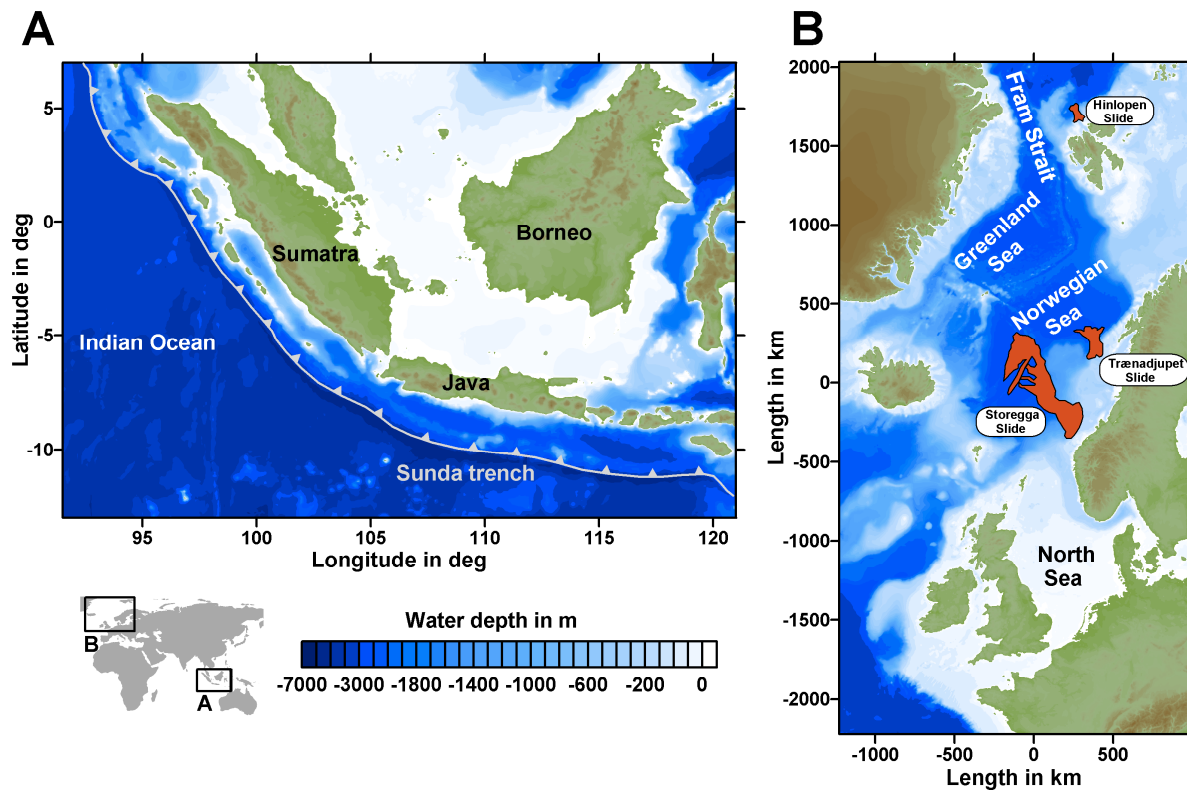
Figure 1.1 *Study areas. A) Sunda Arc off Indonesia. B) Atlantic off northwest Europe. Large scale historical landslides are shown in red (after Haflidason et al. 2004).*

Greece in 1963 (Papadopoulos et al. 2007), and near Nice, France in 1979 (Assier-Rzadkiewicz et al. 2000) The extreme local run-up of 26 m following the 1992 Flores earthquake in the village of Riangkroko, Indonesia, has been associated with submarine landsliding as well (Tsuji et al. 1995; Imamura et al. 1995). An event receiving large scientific interest was the 1998 tsunami off Papua New Guinea. An earthquake of magnitude M_w=7.1 led to a slope failure 30 km off Sissano lagoon that generated a tsunami with 15 m run-up at the nearby village (Lynett et al. 2003). Bathymetric and seismic data that where collected shortly after the event revealed a rotational slump of 600 m height and about 4 km width and length (Tappin et al. 2001; Sweet and Silver 2003). This discovery distinctly contributed to the awareness that submarine landslides are important agents of tsunami generation.

Certain conditions must be fulfilled in order to induce submarine slope failure. First, a large amount of sediments must be transported, so that a slope evolves into a critical stage and, secondly, a trigger has to induce the mass movement. The first condition is fulfilled near river estuaries and within submarine fans with high sedimentation rates, but also in the oceanic melting regions of continental glaciers. At subduction zones, steep submarine slopes are formed. Here, large amounts of sediments transported by the subducted plate are added to the accretionary prism of the overriding plate. Slopes may destabilize for two main reasons: due to an increase of the applied stresses (because of gravitational loading by sediments or

accelerations of an earthquake) or if the inner strength decreases (by means of increasing excess pore pressure, oversteepening or the melting of gas hydrates) (Hampton et al. 1996). If a slope is critical, a landslide can be theoretically initiated by any small perturbation, although in most cases, the final trigger is produced by an earthquake.

1.1 Aims of the study

The 2004 Sumatra tsunami once again showed the disastrous potential of tsunamis. The understanding of earthquakes and tsunamis is especially important for Indonesia, as it is located very close to the subduction zone of the Sunda Arc. Following the Sumatra earthquake, there was large scientific interest in the source process of megathrust Sunda earthquakes and their tsunamigenic potential. However, the tsunami hazard posed by submarine landslides for Indonesia has not been studied yet.

- In this thesis, I address the question, if landslide tsunamis can pose a danger to Indonesian communities at the Indian Ocean.
- I analyze location, geometry and failure mechanism of submarine landslides in this region. Thereby, I investigate if certain areas are more prone to submarine slope instability than others.
- I numerically model subrecent and hypothetical tsunami scenarios and quantify possible inundation heights at the coast.

There are well tested tools for tsunami early warning of earthquake tsunamis: Seismic waves of an earthquake can be recorded by seismometers and used to calculate the earthquakes magnitude, location and other source parameters. Based thereon, the tsunamigenic potential of an earthquake is estimated after several minutes and an appropriate warning can be issued. More advanced techniques involve GPS-measurements to deduce further earthquake parameters (Sobolev et al. 2007; Hoechner et al. 2008). A tsunamigenic landslide, however, cannot be easily detected by seismometers or GPS stations.

- The second focus of this thesis is the development of a new detection tool of large submarine landslides by means of a land-based tiltmeter array.
- I describe basic principles of the detection method.
- I compute hypothetical tilt recordings for a potential landslide off Spitsbergen in the North Atlantic.
- I analyze possible tsunami scenarios for the hypothetical Spitsbergen event.
- An inversion routine is introduced that permits to evaluate fundamental slide parameters like location, volume and velocity. I exemplify the routine using the historical Storegga slide off Norway.
- Finally, I test the scope of this method by applying it to known landslide events worldwide.
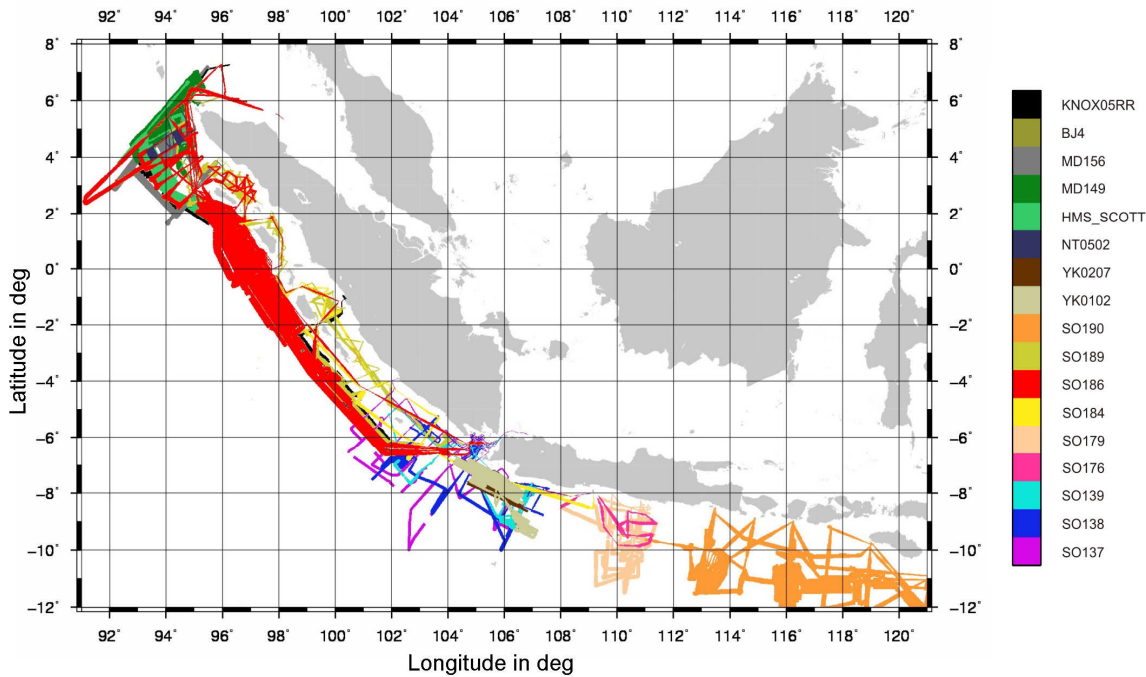
Figure 1.2 *Bathymetry coverage at the Indonesian part of the Sunda Arc. Data has been collected by RV Revelle (KNOX05RR), RV Baruna Jaya IV (BJ4), RV Marion Dufresne (MD156, MD149), HMS Scott, RV Natsushima (NT0502), RV Yukosuka(YK0207, YK0102) and RV Sonne (SO190-SO137).*

1.2. Study Areas

The new bathymetry data off Indonesia that I use in this study has been recorded in the aftermath of the Great Sumatra Earthquake. Naturally, the attention was focused on the Sunda Arc (Figure 1.1A). Here, the Indo-Australian plate subducts beneath the Sunda shelf. This process led to the creation of a large accretionary wedge west of Sumatra and the uplift of the Mentawai archipelago. The accretionary wedge south of Java, Bali, Lombok, Sumbawa and Sumba is smaller compared to that of Sumatra and no islands emerge at the forearc high. Largest water depths are reached at the trench with 5000 m off Northern Sumatra and 7000 m south of Sumbawa

Another area prone to landsliding is the North Atlantic off northwest Europe. Extensive glacial sediment supply during the stadials created continental slopes that have failed in several catastrophic events (Figure 1.1B). The best studied mass movement is the Storegga slide that took place 8200 years before present (BP) and dislocated 2400 km³ of sediment during one failure (Bondevik et al. 2005). Other events comprise the Hinlopen slide (probably pre-holocene) north of Svalbard and the Trænadjupet slide (4000 years BP) off Norway, involving 1350 km³ (Vanneste et al. 2006) and 500 km³ (Laberg et al. 2002), respectively.
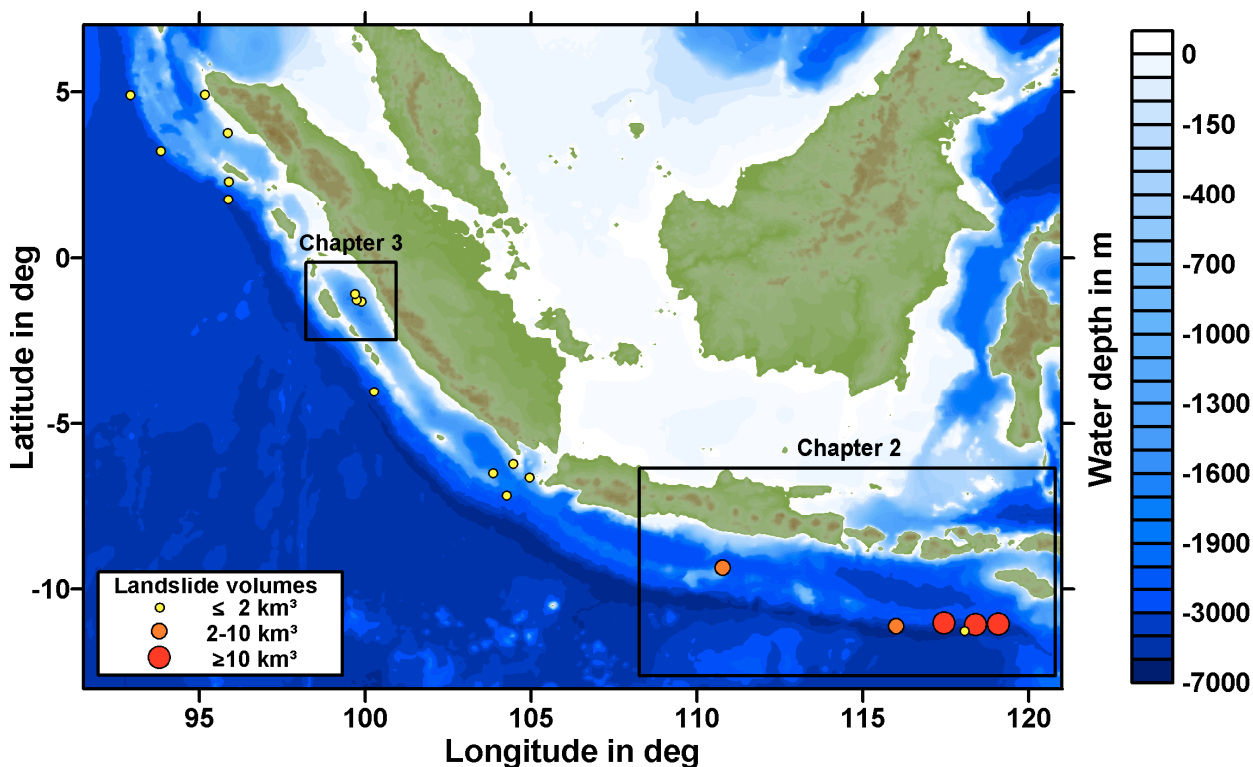
Figure 1.3 *Overview of identified landslides. In this thesis (chapter 2 and 3), I focus on the largest events.*

1.3. New Sunda Arc bathymetry data and identified landslides

The bathymetry measurements off Indonesia were conducted during several cruises of German, Japanese, French, British, American and Indonesian vessels (Figure 1.2). The data was compiled at the Federal Institute for Geosciences and Natural Resources (BGR, Hannover). Large portions of the trench area and the accretionary prism have been covered. However, especially in the forearc basins and south of Java the data is not complete. The landslides I discuss in this thesis have been identified based on data collected onboard the RV Sonne. The resolution of the recorded multibeam bathymetry data is 2°. This corresponds to 200 m in the deep sea (at 6000 m water depth) and 50 m in Sumatran forearc basins (at 1500 m water depth).

I analyzed the available bathymetry data, visually searching for characteristic head scarp walls and landslide deposit. I identified 20 events whose locations are mapped in figure 1.3. Assuming parabolic profiles for slide width and length, I estimated the volume of each mass movement. The approximated landslide sizes range between 0.1 km³ up to 20 km³. Events of possibly tsunamigenic size at the eastern Sunda margin and off central Sumatra are studied in detail in chapter 2 and 3, respectively.

1.4. Landslide tsunami modeling methods

During submarine mass movements, energy is invested in the displacement of the surrounding water. This might lead to the initiation of a series of tsunami waves that propagate towards the coast. I conduct the landslide tsunami modeling in two

distinct parts: The movement of the landslide together with the tsunami generation followed by the propagation of the tsunami:

1.4.1 Landslide modeling and tsunami generation

Depending on the applicability condition, we use two methods to model the slide movement and the tsunami generation.

(i) To study tsunami generation upon landslide, we are interested in the immediate change of a large mass. Thus, for simplicity, we do not consider slow moving precursors and prolonged turbidity currents. Instead, we approximate the event by a sliding solid body of Gaussian shape. This shape is designed to approximate length, width and height of the landslide. Further, it displays good stability properties during the computation of tsunami propagation. We apply prescribed slide motion which, in similarity to previously published models (Harbitz 1992; Løvholt et al. 2005), exhibits a symmetrical velocity profile, consisting of smoothly joined sinusoidal parts. As the slide propagates, the sea bottom change is projected towards the water surface and the wave is build up dynamically.

The applicability condition of this modeling approach has been investigated by Lynett and Liu (2002). Depending on the tsunami propagation model, the ratio of slide length to submergence depth has to be larger than 30 for shallow water simulations, or larger than 7 for Boussinesq codes. The mass movements considered in chapter 4 and 5 fulfill this condition. The landslide geometries used in chapter 2 and 3, however, do not satisfy the constraint. In these cases, we fall back on the following method.

(ii) Watts et al. (2005) and Grilli et al. (2005) derived a semi-empirical set of equations based on physical arguments and wave tank experiments. The input parameters slide length, width, height and slope angle can be extracted directly from the bathymetry data. The formulas yield the initial tsunami wave height and a characteristic wave length. Those values can be used to create an initial wave distribution as input for the tsunami propagation model. These equations are applicable, as long as wave breaking in the generation area can be excluded. Following Watts et al. (2005), this hold true, if the ratio of slide length to initial submergence depth is smaller than 17, which is fulfilled for the scenarios of chapter 2 and 3.

1.4.2 Tsunami propagation modeling

In this thesis, I apply two tsunami propagation models: TUNAMI-N2 (Imamura et al. 1997) and COULWAVE (Lynett and Liu 2002). Both of them numerically solve the continuity equation and the Euler's equations of fluid dynamics describing inviscid flow. Each model, however, uses different assumptions.

(i) TUNAMI-N2 applies the long-wave approximation, assuming that the ratio of water depth and wave length μ of the considered wave field is much smaller compared to 1: o(μ)<<1. In this case the vertical movement of particles is negligible. The leap-frog scheme is used for the finite difference discretization of time and space. It applies central differences for all involved derivatives except for the convection terms. Here, an upwind scheme is used to ensure computational stability (Imamura et al. 2006). The accuracy of this discretization is of the order of $(\varDelta t)^2$ in time and $\varDelta x$ in space, where $\varDelta t$ and $\varDelta x$ represent the temporal and spatial step sizes.

(ii) COULWAVE allows to describe a wider range of waves, as it assumes the square root of μ to be much smaller than 1: o(μ^2)<<1, called the Boussinesq approximation. This introduces frequency dispersion into the mathematical formulation (Lynett and Liu 2002). Furthermore, COULWAVE divides the water column into multiple layers, with each layer being governed by an independent velocity profile. Within the finite difference formulation, all spatial derivatives are differenced to fourth order accuracy $(\varDelta x)^4$. A high-order predictor-corrector scheme ensures an accuracy in time of $(\varDelta t)^4$. The high accuracy distinctly slows the computation process, but a parallelized version of the model is available for use on MPI-based clusters.

1.5 Tilt measurements and accuracy

Tiltmeters (or inclinometers) are used to measure the inclination of earth's surface. They are widely in use to monitor volcanic deformation, earth tides and postglacial rebound. Two kinds of inclinometers exist, the pendulum and the water-tube type:

The first type of tiltmeters uses a pendulum at its gravitational equilibrium point. The pendulum's position with respect to a reference frame is measured yielding the respective inclination. These tiltmeters can be relatively small and can be easily installed in boreholes. The ASKANIA borehole tiltmeter, for instance, measures 1.6 m in length and 14 cm in diameter. It resolves inclinations with an accuracy of 1 nrad (Gebauer et al. 2007). (To illustrate the dimensions, 1 nrad (corresponding to 10^{-9} rad or $5.73 \cdot 10^{-8}$ degree) is the angle that is formed, if a theoretical straight line of 1000 km length is lifted at one end by 1 mm.)

A water-tube tiltmeter follows the principle of a water-level to measure inclinations. It consists of an elongated water reservoir and the tilt is detected by accurately measuring the position of the water surface. This can be done using a capacitative sensor where one electrode is partially, the other totally submerged in water. Hence, the capacity between both electrodes depends on the submergence depth and thus on the position of the water surface. The long-base water-tube tiltmeter discussed by D'Oreye and Zürn (2005) provides tilt data with an accuracy of 0.005 nrad.

1.5. Structure of the thesis

My doctoral thesis is based on four manuscripts submitted to peer-reviewed international journals.

The first manuscript 'Submarine landslides at the eastern Sunda margin: observations and tsunami impact assessment' (S. Brune, S. Ladage, A. Y. Babeyko, C. Müller, H. Kopp, S. V. Sobolev) bases on six recently discovered submarine landslides at the eastern Sunda Arc. Three of these events involved very large sediment volumes of at least 60 km³. Conducting tsunami simulations, I estimated the associated run-up heights at nearby coasts. Four slides are located directly above the fault plane of the 1977 tsunamigenic M_w=8.3 Sumba earthquake. By comparing documented run-up data to modeling results, I investigate the possible correlation between this earthquake and the mass failures. Finally, I model whether tsunamigenic landslides at the trench off Bali could endanger the highly populated coasts of Bali or Lombok.

In the second publication 'Hazard assessment of underwater landslide generated tsunamis: a case study for the Padang region, Indonesia' (S. Brune, A. Y. Babeyko, C. Gaedicke, S. Ladage), I describe three newly found landslides located in 70 km distance to the important city of Padang in Western Sumatra, Indonesia. I model the generated tsunamis and estimate the run-up heights in Padang. Further, I assess the tsunami hazard at Padang, posed by potential future tsunamigenic landslides.

The third publication entitled 'Tsunami modeling of a submarine landslide in the Fram Strait' (C. Berndt, S. Brune, E. Nisbet, J. Zschau, S. V. Sobolev) investigates a possible tsunamigenic mass movement west of the Norwegian island of Spitsbergen. Here, at the Kongsfjorden Trough Mouth Fan, sediments of the last glaciation have not yet failed. The influence of Arctic warming on slope stability is discussed. I formulate four possible landslide scenarios and compute the induced tsunamis in the Greenland, Norwegian and North Sea. Further, I propose the use of tiltmeters to detect the event. Using the elastic half-space approximation, I model the response of land-based tiltmeters to the mass movement. The computed signals are clearly within the accuracy range of present day tiltmeters.

Within the fourth publication 'Towards early warning for tsunamis, generated by large submarine landslides' (S. Brune, A. Y. Babeyko, S. V. Sobolev), I expand the idea of detecting submarine mass movements by means of tiltmeters. I introduce an inversion technique which allows to identify the important landslide parameters location and tsunamigenic potential (the product of volume and maximal velocity). I illustrate this technique by applying it to the prominent Storegga slide west of Norway. Correct inversions are found for both deformed and undeformed slide bodies and for different aspect ratios of slide geometry. I conduct tsunami modeling and compare mareograms of inversion and original model. Finally, I analyze the applicability scope of this technique by employing it to a series of well-studied landslide events.

Chapter 2

Submarine landslides at the eastern Sunda margin: observations and tsunami impact assessment

Sascha Brune [1], Stefan Ladage [2], Andrey Y. Babeyko [1], Christian Müller [2], Heidrun Kopp [3], Stephan V. Sobolev [1]

[1]*Helmholtz Centre Potsdam GFZ German Research Centre for Geosciences, Potsdam, Telegrafenberg, 14473 Potsdam, Germany*
[2] *Federal Institute for Geosciences and Natural Resources (BGR), Stilleweg 2, 30655 Hannover, Germany*
[3] *Leibniz Institute of Marine Sciences at the Christian-Albrechts University of Kiel (IFM-GEOMAR), Wischhofstr. 1-3, 24148 Kiel, Germany*

Abstract
Our analysis of new bathymetric data reveals six submarine landslides at the eastern Sunda margin between central Java and Sumba Island, Indonesia. Their volumes range between 1 km³ in the Java fore-arc basin up to 20 km³ at the trench off Sumba and Sumbawa. We estimate the potential hazard of each event by modeling the corresponding tsunami and its run-up on nearby coasts. Four slides are situated remarkably close to the epicenter of the 1977 tsunamigenic Sumba M_w=8.3 earthquake. However, comparison of documented tsunami run-up heights with our modeling results neither allows us to confirm nor to decline the hypothesis that the earthquake triggered these submarine landslides. Finally, we investigate whether a slope failure at the trench off Bali could cause a dangerous tsunami at the highly populated coasts of Bali and Lombok.

2.1 Introduction
Tsunamis pose a major threat to population and structures in many coastal areas around the world. Although most tsunamis are generated by submarine earthquakes, underwater slope failures can be responsible for local tsunamis as well. Landslide-generated tsunamis comprise at least 8 % of all documented historical events worldwide (ITDB catalogue 2007). That makes the investigation

of submarine landslides a necessary step for future tsunami hazard assessment. One of the best studied historical events took place in Papua New Guinea, 1998, where a 4 km³ submarine slump was triggered by a comparatively small earthquake (Tappin et al. 1999; Sweet and Silver 2003). The generated tsunami inundated nearby coasts, leading to maximal run-up heights of 15 m (Lynett et al. 2003). Whether a submarine mass movement generates significant inundation, depends on slide volume, tsunami propagation distance and local bathymetry. If the tsunami propagation distance is of the order of a few kilometers, even small landslides (0.0024 km³ slide at Fatu Hiva, French Polynesia, 1999 (Hébert et al. 2002)) can cause significant damages to coastal communities. Very large events like the 200 km³ 1929 Grand Banks slide (Fine et al. 2005) or the 2400 km³ pre-historic Storegga slide (Bondevik et al. 2005) were capable of generating large run-up even at locations in several hundred kilometers distance.

Indonesia is especially endangered by tsunamis, due to its proximity to the Sunda subduction zone stretching over 5000 km from the Andaman Islands and Sumatra to Java, and the Lesser Sunda Islands. The subduction of the Indo-Australian plate beneath the Sunda shelf creates tectonic stresses which upon sudden release cause earthquakes of major magnitudes that potentially generate large tsunamis (Hamzah et al. 2000). The M_w=9.3 Sumatra-Andaman earthquake in December, 2004 rupured over 1000 km (Krüger and Ohrnberger 2005) and induced a catastrophic ocean-wide tsunami. Run-up heights reached more than 30 m in Aceh, Indonesia (Borrero et al. 2006) and nearly 20 m in Thailand (Tsuji et al. 2006). Off Java and the Lesser Sunda Islands, devastating tsunamis were induced by the M_w=8.3 Sumba earthquake of 1977, the eastern Java earthquake (M_w=7.8) of 1994 and the M_w=7.7 Pangandaran earthquake in 2006 (ITDB catalogue 2007). Maximum run-up values of respectively 8 m (Kato and Tsuji 1995), 14 m (Tsuji et al. 1995a) and 20 m (Lavigne et al. 2007; Fritz et al. 2007) have been identified.

By triggering submarine mass failures, however, even moderate earthquakes can induce dangerous tsunamis. Large local run-up during the 1979 tsunami at Lomblen Island and in 1992 at the northern coast of Flores Island has been explained by underwater mass failures (Tsuji et al. 1995b; Rynn 2002). Whether the above mentioned 20 m run-up during the 2006 Central Java tsunami was caused by a landslide, is currently discussed (Matsumoto et al. 2007). Submarine debris avalanches have been identified west of Sumatra (Tappin et al. 2007), at the toe of the accretionary prism. The overall slide volume of the largest event is with 1 km³ (Moran and Tappin 2006) comparably small which excludes it as a significant tsunami source (Tappin et al. 2007).

Our present study is based on new bathymetric data collected onboard the RV "Sonne" during the MERAMEX (2004) and SINDBAD (2006) surveys. The multibeam bathymetry data has a resolution of 2° (corresponding to 200 m at ocean depths of 6000 m). The cruises have been conducted by two German institutions: IFM-GEOMAR, Kiel, and the Federal Institute for Geosciences and
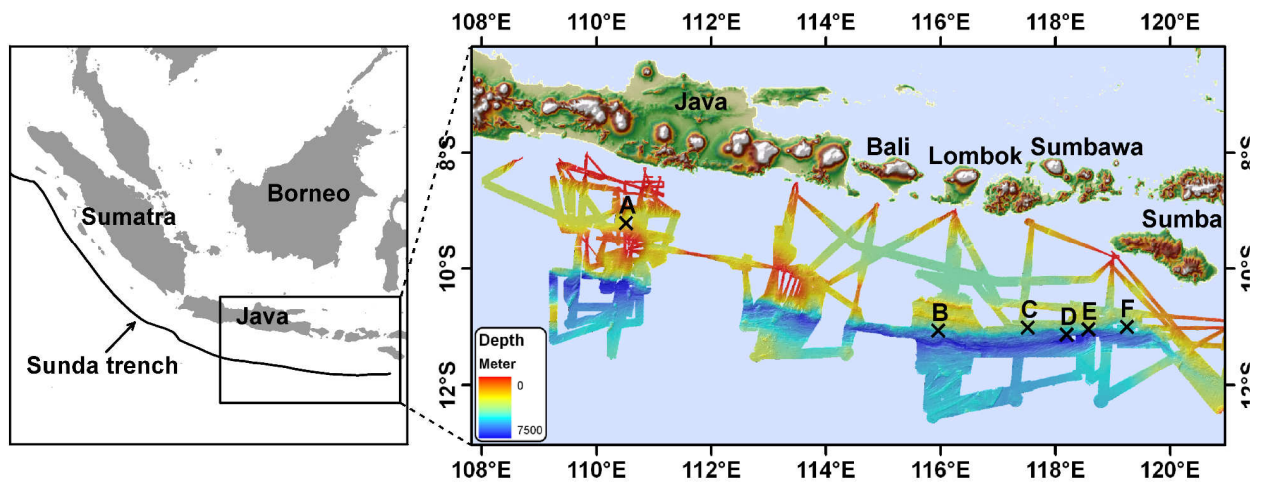
Figure 2.1 *Overview map showing bathymetric coverage and locations of slides A to F.*

Natural Resources (BGR), Hannover. Our study area comprises the eastern Sunda margin off Indonesia, between central Java and Sumba (Figure 2.1). Detailed analysis of the bathymetry data revealed evidences of six landslide events. We start with a short geological background of the studied area and proceed with detailed slide descriptions and numerical models of the tsunamis generated during these events.

2.2 Geological setting

The over 5000 km long Sunda margin extends from the Andaman Sea in the north to Sumba Island in the east. It is characterized by the subduction of oceanic lithosphere of the Indo-Australian plate beneath the Indonesian Archipelago. East of Sumba Island a transition to the Banda Arc and the collision with continental Australian crust takes place. Subduction initiated in the late to middle Tertiary (Hall 1997) and has formed a mature convergent margin with a well developed accretionary prism, an outer fore-arc high and fore-arc basins (Schlueter et al. 2002; Kopp and Kukowski 2003).

The eastern Sunda Arc sector from East Java to just west of Sumba Island resembles a unique segment of this subduction zone. Here, the oldest oceanic crust along the entire Sunda Arc of Late Jurassic age (155-145 Ma; Heine et al. 2004; Müller et al. 2008) subducts at a rate of up to 70 mm per year in nearly trench normal direction (Simons et al. 2007). With water depths reaching more than 7000 m, this is also the deepest segment of the Java trench. Off eastern Java the sediment thickness on the incoming plate and in the trench is less than 1 km (Kopp et al. 2003). Further east the oceanic crust and trench are largely devoid of sediments, except for a thin hemipelagic sediment cover. The accretionary wedge in the eastern segment is between 70-100 km wide and forms a discontinuous outer fore-arc high with maximal water depths exceeding 2000 m. Internally, the accretionary wedge is built up of a series of landward dipping imbricate thrust sheets of accreted and deformed rocks (Lueschen et al. 2009; van der Werff 1995).

11

	Slide A	Slide B	Slide C	Slide D	Slide E	Slide F
Longitude	110°31'E	115°57'E	117°52'E	118°12'E	118°34'E	119°15'E
Latitude	9°18'S	11°6'S	11°'4S	11°9'S	11°4'S	11°3'S
Width (km)	7	7	23	7	25	18
Length (km)	8	7	8	4	5	10
Height (m)	150	200	200	100	300	300
Volume (km³)	3	4	15	1	15	20
Depth (m)	2000	5300	5300	6000	6100	5000
Travel Distance (km)	6	4	12	4	5	10
Mean local slope angle (°)	4	15	10	8	15	5

Table 2.1 *Slide parameters. Longitude and latitude designate the estimated initial center of mass location. Width is measured perpendicular, and length parallel to the slope. Volume is inferred by parabolic shape approximation. Travel distance denotes the estimated movement of the slide's center of mass. Mean local slope angles are inferred from bathymetry cross-sections of slide areas.*

Off eastern Java the Roo Rise, elevated about 1500 m above surrounding sea floor, is recently subducting and causing frontal erosion of the accretionary wedge (Kopp et al. 2006). Further east the Java trench morphology is rugged and controlled by normal faulting of the oceanic crust with horst and graben structures along the outer trench wall. The faults are more than 60 km long and have a throw of 500 m. They strike slightly oblique to the trench and can be imaged deep beneath the slope toe. Subduction of these faults and horst and grabens contributes to local oversteepening of the slope toe with slumping (van der Werff 1995; Müller et al. 2008; Lueschen et al. 2009). The distribution and focal mechanisms of shallow seismicity along the Java trench clearly shows recent activity of these faults (Eva et al. 1988; Spence 1986).

2.3 Slide descriptions
We analyzed the bathymetric data searching for head scarp walls and associated landslide deposits. Six major subrecent landslides have been identified within the studied area. In the following, they will be designated alphabetically from A to F (Figure 2.1). Slide A is located within the Java fore-arc basin, 120 km off coast. Slide B was found at the accretionary wedge 240 km off Lombok and slides C to F near the trench, at a distance of 130 to 200 km to Sumba Island.

The deposition lobes of slides A and F are clearly visible (Figure 2.2). Their shape and proximity to the failure area suggest rotational slumping as probable failure mechanism. In the cases B, C, D, and E, the depositional area is barely observable. We analyzed backscatter data, 3.5 kHz sub-bottom - and multichannel-reflection seismic profiles. Landslide head scarps were identified, however associated landslide sediment deposits were not detectable.
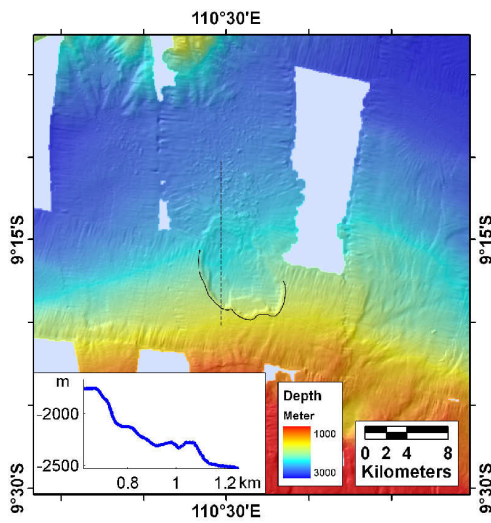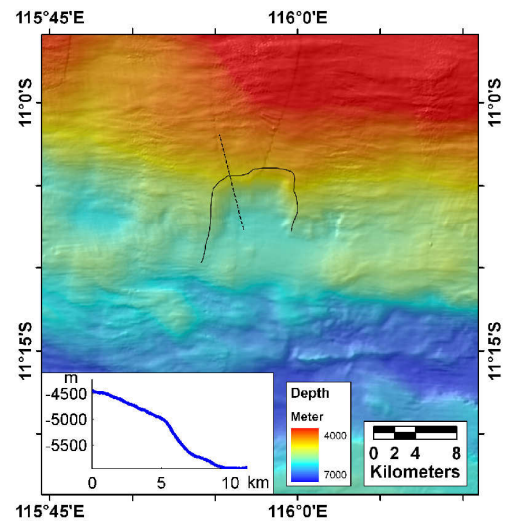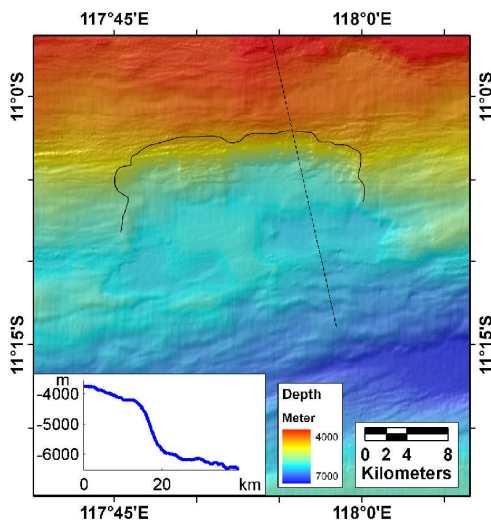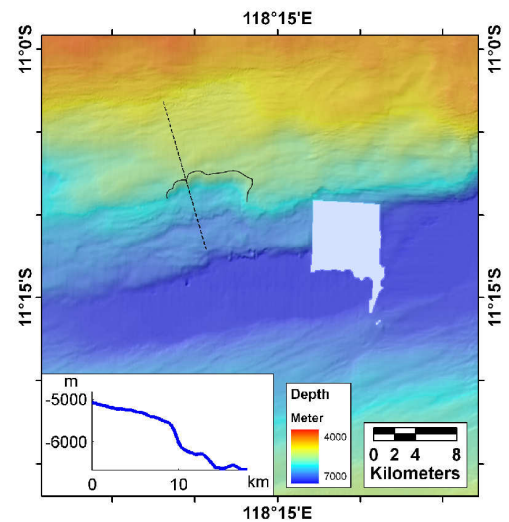
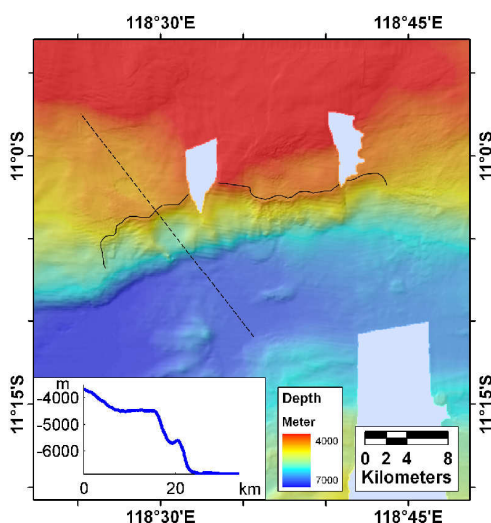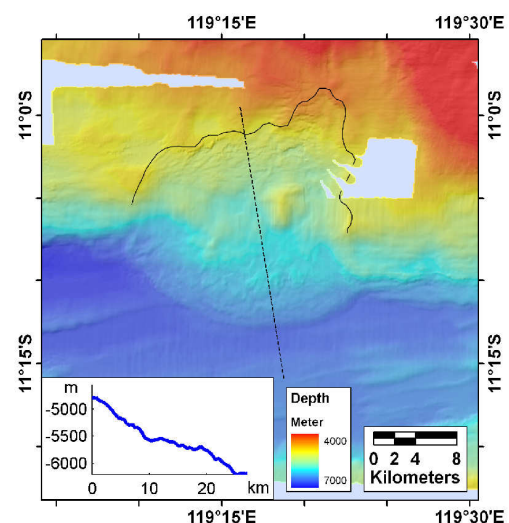*Figure 2.2* Bathymetry maps, interpretations of the escarpments (solid lines) and locations of cross sections (dashed lines). Corresponding profiles are shown in white inlets. Note the different depth scale for slide A. Slide locations are mapped in Figure 2.1.

The position of the slides and their geometrical parameters are deduced from the bathymetric maps and listed in Table 2.1. Slide dimensions perpendicular and parallel to the slope, denoted as width and length, respectively, range between 4 and 25 km. The travel distance which corresponds to the center of mass translation, is obvious only for the cases A and F, as they exhibit typical deposit lobes. Travel distances estimated for the other four slides comprise rather high uncertainties. We evaluate the slide heights by comparing the slope profile inside the slide zone and besides it. This yields values between 100 m for slide D and up to 300 m for slide E and F. Slide volumes of slides A to F (3 km³, 4 km³, 15 km³, 1 km³, 15 km³, and 20 km³, respectively) are estimated under the assumption of a parabolic slide shape.

It is very difficult to date underwater mass movements based on bathymetric images only. As submarine diffusion rates are notably smaller than on land, landscapes evolve much slower. So, even a "fresh" looking slide can be thousands of years old (McAdoo and Simpson 2005). Dating techniques involving the steepness of the head wall are only applicable if at least one additional independent failure date is provided by a secondary method (Kukowski et al. 2008). In this region, this has not been done so far. However, in section 2.5 we investigate the possibility that slides C to F have been triggered by the 1977 Sumba earthquake (M_w=8.3). If confirmed, this would also imply the age of the slumps.

Most submarine slope failures are caused by interplay of several factors like oversteepening of slopes and ground shaking due to an earthquake (Masson et al. 2006). At the position of slide A, basin slopes have been possibly steepened due to the subduction of a seamount located on the oceanic plate (Masson et al. 1990; Kopp et al. 2006). Concerning the other five events at the slope toe in the trench, oversteepening can be attributed to tectonic erosion (Kopp et al. 2006). For slopes close to failure, even a comparatively small earthquake is sufficient to induce a landslide.

2.4 Modeling of induced tsunamis
2.4.1 Methods
Our tsunami model consists of three distinct stages: generation, propagation and run-up. We describe tsunami generation using the technique of Watts et al. (2005) and Grilli et al. (2005). It provides a set of semi-empirical equations that are based on physical arguments and wave tank experiments. The initial tsunami wave height η_{2HD}, the wave length λ and the characteristic time t_0 (Table 2.2) are estimated based on landslide geometry parameters length, width, height, depth and travel distance as well as the mean local slope angle (Table 2.1).

Following Watts et al. (2003), an initial wave distribution can be used to approximate the sea surface deformation provoked by the mass movement. It is argued that during the acceleration phase of a slide, most of the tsunami energy is invested in potential energy. Only after the characteristic time t_0, when the slide

	Slide A	Slide B	Slide C	Slide D	Slide E	Slide F
Initial wave height η_{2HD} (m)	2.9	1.0	6.4	0.4	8.8	7.0
Characteristic wave length λ (km)	19	23	27	20	15	27
Characteristic time t_0 (s)	130	100	120	80	60	120

Table 2.2 Hotstart parameters defining the initial sea surface for the tsunami propagation model. Their calculation follows the technique of Watts et al. (2005).

does not accelerate any longer, the transformation of potential energy into kinetic energy takes place. The initial sea surface was constructed according to Watts et al. (2005) and Synolakis et al. (2002): Along slide direction, two Gaussian curves of different sign approximate the wave profile. Their heights correspond to η_{2HD} and the widths are defined by λ. Perpendicular to the slide direction, a solitary-like extrapolation proportional to $sech^2(3 \cdot y/(w+\lambda))$ is used, where w is the slump width and y the corresponding coordinate. The semi-empirical equations are applicable as long as wave breaking can be excluded. To ensure this, the ratio of slide length to initial submergence depth must be smaller than 17 (Watts et al. 2005). The corresponding values of slide A to F (4, 1.3, 1.5, 0.7, 0.8 and 2, respectively) clearly satisfy this condition.

Alternative formulations include a dynamic slide movement that continuously influences the surface wave, like the shallow water approach of Harbitz (1992) or the Boussinesq model of Lynett and Liu (2002) (see chapter 4 and 5 of this thesis). These models allow for a more detailed slide description, however, they are only valid if the ratio of slide length to submergence depth is bigger than 30 for shallow water models or 7 for Boussinesq simulations (Lynett and Liu 2002). In our case, with length to depth ratios between 0.7 and 4, these formulations cannot be used.

The tsunami propagation is modeled with the finite difference, nonlinear shallow water code TUNAMI-N2 (Imamura et al. 1997). The shallow water approximation is fulfilled, as all wave lengths are much larger than the water depth. Tsunami calculations are performed on a 3200×2200 grid using a spatial step size of 10 arc seconds (~309 m) and a time step of 0.5 s. Bathymetry is based on interpolated GEBCO data (IOC, IHO and BODC 2003).

Run-up heights are estimated using the formula of Chesley and Ward (2006): $R = A(d)^{4/5} \cdot d^{1/5}$, where A is the wave amplitude, measured at water depth d. This formula is based on the conservation of wave energy flux and can be used for both breaking and non-breaking waves (Ward and Asphaug 2003). In this paper we use

virtual gauges at depths of approximately 20 m. In section 2.8, we address the influence of the choice of water depth d on the run-up value R.

2.4.2 Results

Figure 2.3 presents distributions of the maximum tsunami heights for the slides A to F. Although events A, B and D involve significant slide volumes (3 km³, 4 km³, 1 km³, respectively) they do not generate significant tsunamis (run-up heights generally do not exceed 1 m). This is interesting, as the Papua New Guinea slump with a comparative volume of 4 km³ was far more efficient in tsunami excitation. The difference lies in slide geometry. While the Papua New Guinea slump had a thickness of 600 m and a length of 4000 m (Synolakis et al. 2002), our slides A, B and D exhibit heights of 100 to 200 m with lengths between 4000 and 8000 m. We investigate the influence of the slide thickness by a parameter study. We double the slide heights of events A, B and D, while correspondingly decreasing their lateral dimensions to keep the volumes constant. According to Watt's formula, the resulting initial tsunami wave height increases by a factor of approximately 7. Hence, a compact slump with larger thickness generates a much higher tsunami, than a broad slump of the same volume.

The volumes of slides C, E, and F (15 km³, 15 km³, 20 km³) are considerably larger than those mentioned before. Generated tsunamis feature initial wave heights of 6 to 7 m. As the tsunami propagates, it is influenced by the regional bathymetry (Satake 1988). So, the central part of the wave front is diffracted eastward by the underwater onset of the Sumba strait (Figure 2.3, slides C and E). Similarly, off-shore seafloor elevations focus the wave energy, as can be seen for Sumbawa (Slide C and E) and Sumba (Slide E). Computed run-up heights for each event are shown in Figure 2.3 by blue bars. Maximum run-up heights of nearly 6 m are computed on Sumbawa for slide C and E. A run-up of 7 m is reached in Ubuoleta on Sumba for slide F.

Tsunami arrival times vary between 20 and 30 minutes for all areas exposed to large wave heights (here arrival time corresponds to the first 1 cm sea surface anomaly). Arrival times for slide D are only shown at locations experiencing water elevations of more than 1 cm (Figure 2.3).

While slide width and length can be estimated from bathymetric data quite accurately, both height and travel distance are subjected to a higher uncertainty. If projected up to the coast, this uncertainty can be responsible for about 50 % run-up variation.
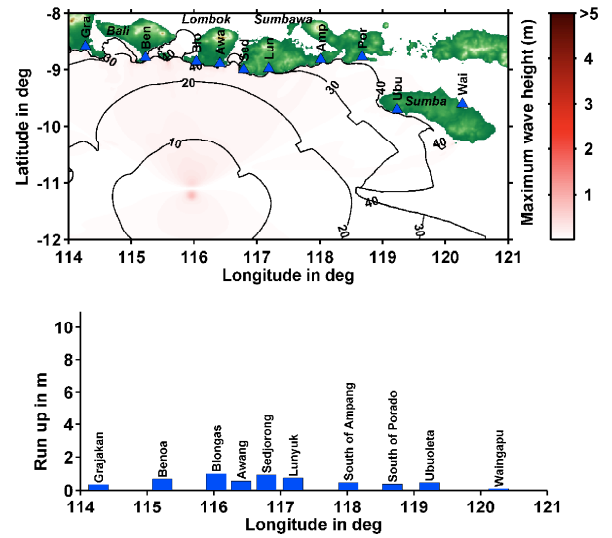
2.5 Triggering of landslides by the 1977 Sumba M_w=8.3 earthquake?

The 1977 Sumba earthquake (M_w=8.3; Lynnes and Lay 1988) was the biggest event in our study area during the 20th century (ITDB catalogue 2007), and one of the largest normal fault earthquakes ever recorded. Its epicenter (11° 8' S, 118° 14' E; CMT catalogue) is located about 200 km southwest of Sumba Island. The
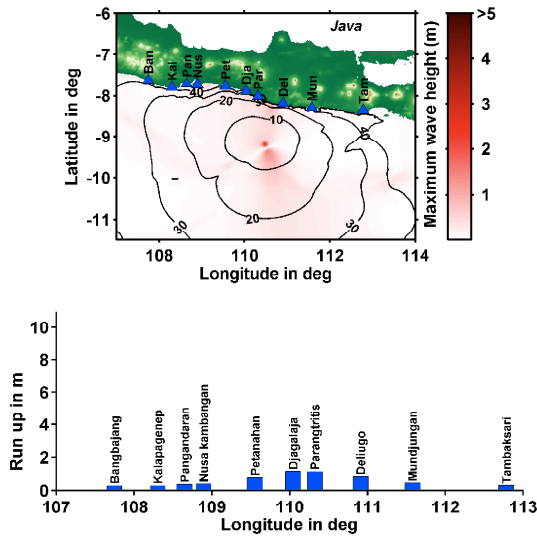
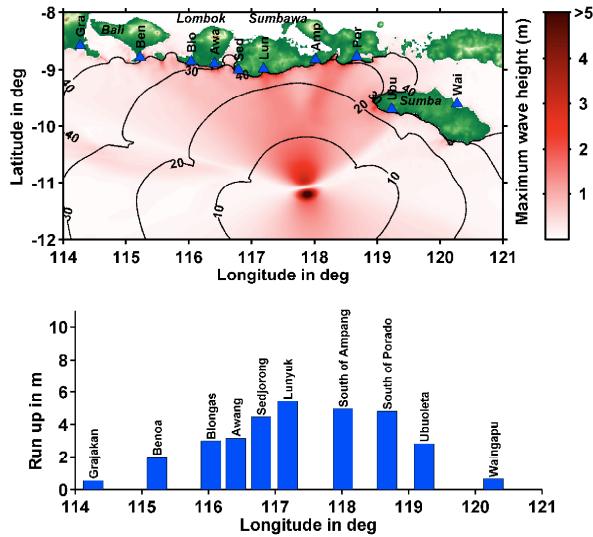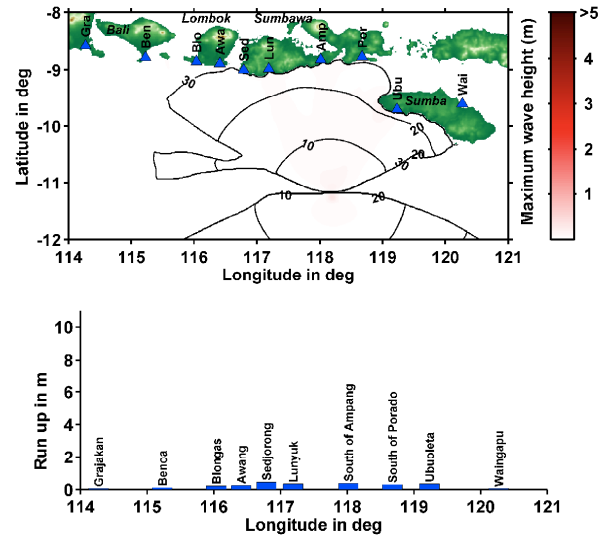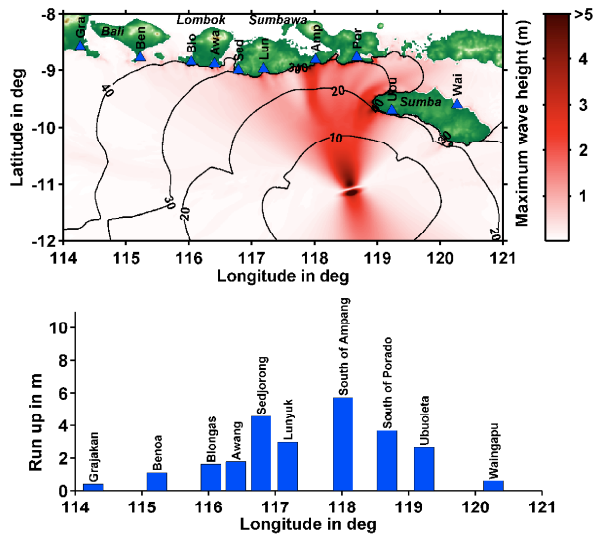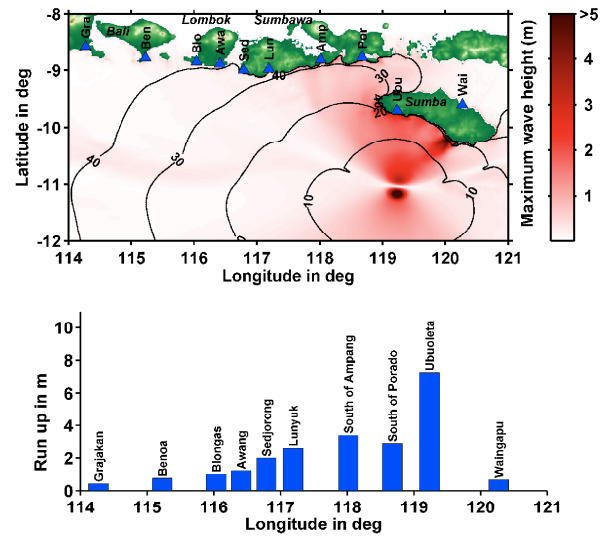**Figure 2.3** *Maximum wave height distributions after 4 hours, arrival times in minutes as well as corresponding run-up heights along the coast projected onto the longitude (bar plots). Locations of virtual gauge stations are mapped as blue triangles with abbreviated names.*

earthquake generated a tsunami which inundated the coasts of Sumba, Sumbawa, Lombok, and Bali resulting in 440 damaged houses and 161 casualties or missing (Kato and Tsuji 1995). In Figure 2.4, we mapped the epicenter location, the seven-days aftershock distribution and the assumed fault plane. Interestingly, slides C to F are located directly above the fault plane. Especially, the location of slide F coincides with an area of high aftershock intensity. This raises the question, if one or more slides might have been triggered by the earthquake. As our knowledge about the slumps is based on remote sensing only, we cannot determine the age of the events and whether they failed during the earthquake. However, an ITIC survey team and Indonesian investigators visited the tsunami affected areas and measured run-up heights (ITIC 1977). That gives us the opportunity to compare results of an earthquake tsunami model to real run-up data. Thereby, we can test if possible discrepancies might be explained by an additional landslide source.

The survey accessed eight locations on Bali and Lombok. Due to difficult accessibility, only two places on Sumbawa and three on Sumba have been visited, whereof two are situated on the far side of the island. Survey locations are mapped in Figure 2.4. Measured run-up values are given with respect to the sea level at time of measurements (ITIC 1977). For our study, we use run-up data that was corrected for astronomical tides (Kato and Tsuji 1995). These run-up values are shown in Figure 2.5a. If more than one run-up is given for the same location, minimal and maximal values are marked in deep and light blue, respectively.

Based on the aftershock distribution (Figure 2.4), we assess the following earthquake parameters: centroid location 118.5°E, 11.2°S, rupture extension 195 km, fault plane width 65 km and strike 70°. The fault plane is slightly wider as if one had used the empirical scaling relations of Wells and Coppersmith (1994). All other parameters are taken from the Global CMT Catalog: magnitude M_w 8.3, scalar moment $3.59 \cdot 10^{21}$ Nm, dip angle 67°, slip angle -98° and depth 23.3 km. In contrast to Kato and Tsuji (1995), we use the steeper of the two possible fault plane solutions which dips southward. In their paper, Kato and Tsuji (1995) assumed the Sumba event to be of the same type as the 1933 Great Sanriku earthquake and decided in favor of the shallow, northward dipping fault plane solution. However, a conjugate set of steeply northward and southward dipping normal faults dominate the morphology of the oceanic crust in the eastern Java trench (Müller et al. 2008; van der Werff 1995). The resemblance in strike and dip angle with the CMT fault mechanism of the 1977 Sumba earthquake clearly favors the southward dipping focal mechanism solution. Assuming a rigidity modulus of 30 GPa, we assess the co-seismic slip to be 9.5 m. Initial sea surface deformation is calculated according to Okada (1985), using the software AVI-NAMI v1.2 (Pelinovsky et al. 2006). We compute maximal subsidence of -3.3 m towards southeast and maximal uplift of 1.1 m in the opposite direction. Calculated run-up heights at surveyed locations are shown in Figure 2.5b. They exhibit only minor discrepancies to measured values (compare with Figure 2.5a).
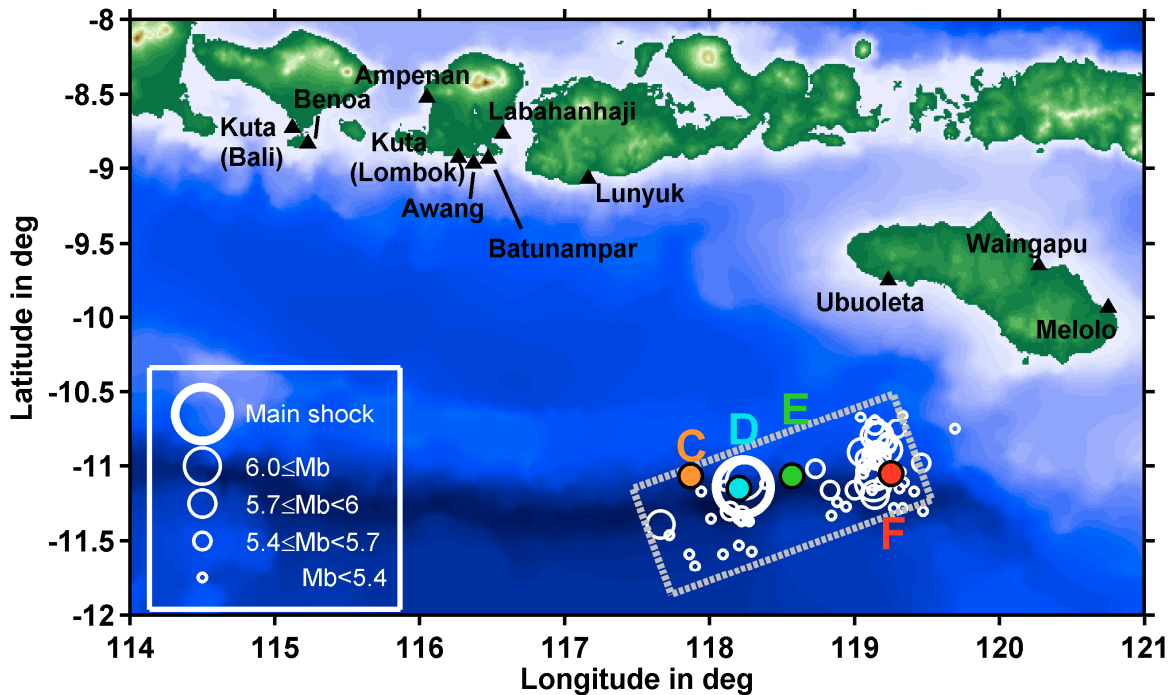
Figure 2.4 *1977 Sumba earthquake: Main shock location, seven-days aftershock distribution and assumed fault plane (dotted rectangle). Also designated are positions of slides C to F as well as locations of the measured run-up (black triangles).*

Interestingly, modeled results for the second, perpendicular fault plane solution of the CMT catalog are quite similar. The initial maximal depression amounts to -3.6 m and the maximum elevation is 0.9, the distribution appears to be shifted slightly southward, but the overall shape is likewise. This explains why the tsunami model calculated by Kato and Tsuji (1995) exhibited similarly good correspondence with measured run-up values.

To test whether the presented landslides were triggered by the Sumba earthquake, we also calculate tsunami run-up heights for slides C, E, and F at the survey locations. As slide D induces only a negligible tsunami (maximum run-up is 40 cm), it will not be discussed. Results are depicted in Figure 2.5c, d and e, respectively. The run-up distribution due to slide C exhibits a similar pattern as the earthquake. The same is true for slide E, but with somewhat smaller amplitudes. If one of these slides were triggered by the earthquake, the corresponding wave fields would superpose at each time step. This does not mean that the maximum run-up values have to be added at each location. They rather depend on the exact timing of the slide failure with respect to the earthquake's main shock. If the largest slide-induced wave arrives several minutes after the highest wave of the earthquake tsunami, it might not contribute to the run-up distribution. As the earthquake tsunami simulation corresponds well with the surveyed run-up values, we can only conclude, that no such superposition can be evidently observed at the given locations.

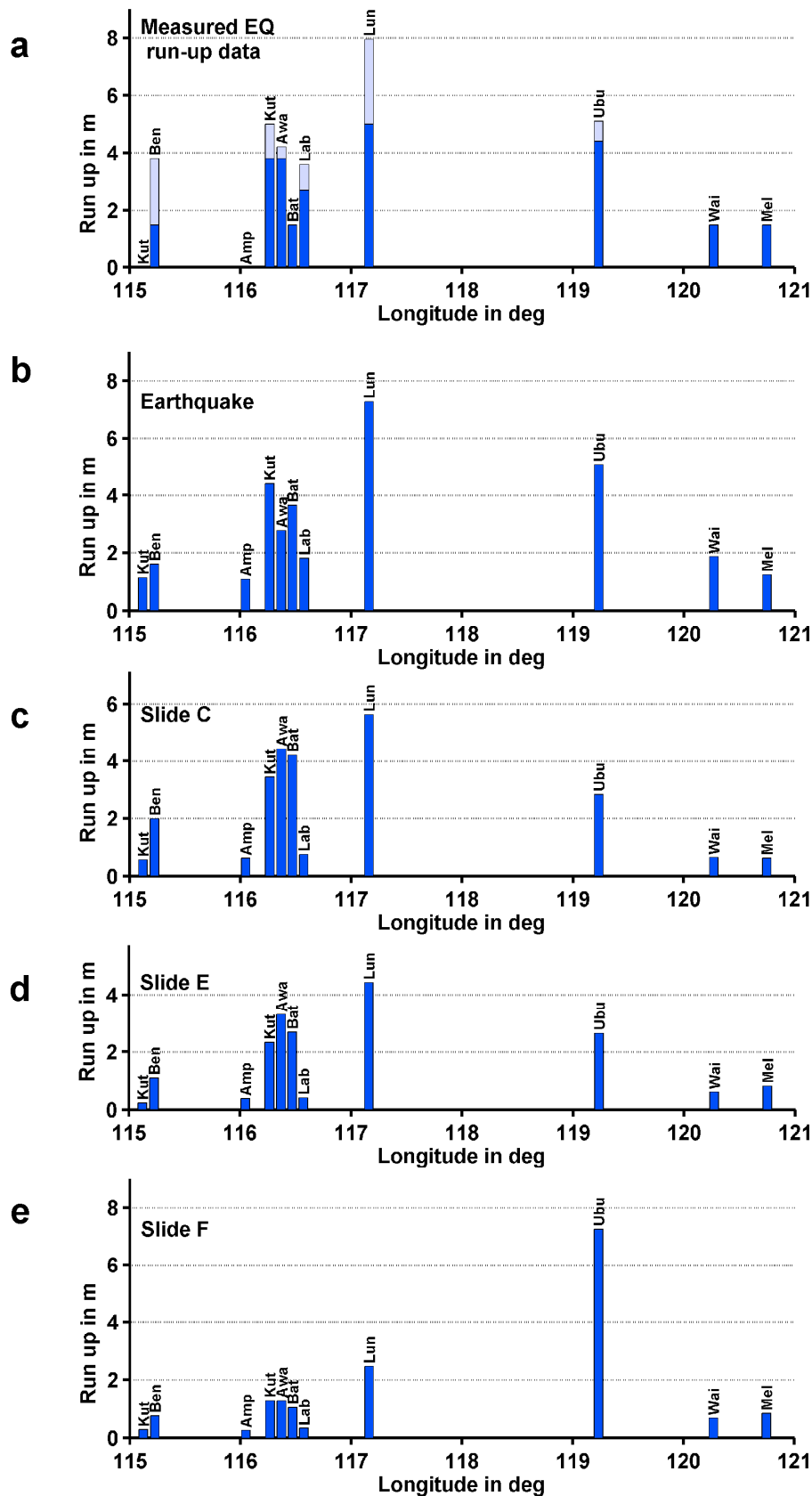**Figure 2.5** *Run-up distributions.* **(a)** *Measured run-up of the 1977 Sumba earthquake. If more than one value was measured at a location, light blue bars show the maximum run-up, while dark blue bars correspond to the minimum run-up.* **(b)** *Computed run-up caused by the 1977 Sumba earthquake.* **(c,d,e)** *Modeled landslide-generated run-up heights for slides C, E and F, respectively. Measurement locations are mapped in Figure 2.4.*
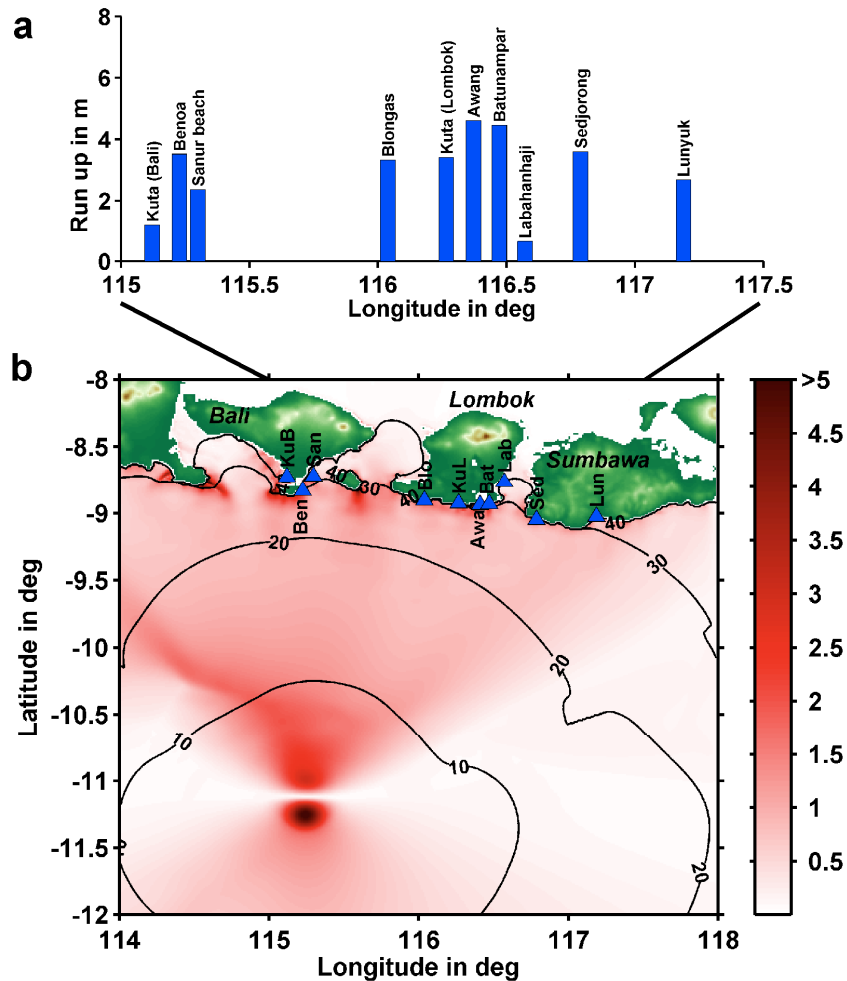
Figure 2.6 *Maximum wave heights, arrival times and run-up distribution for a hypothetical 20 km³ event off Bali. Calculation time was 4 hours. Virtual gauge locations are marked with blue triangles and abbreviated names.*

Slide F however, shows a different picture. In this case, run-up at Ubuoleta exceeds the measured value by about 2 m. One could deduce that this slide was not induced by the 1977 earthquake. However, this conclusion would be based on one data point only and, regarding the intrinsic error range of the model (section 2.4.2), appears to be premature.

2.6 Hypothetical slide event in the Bali/Lombok region

In present day bathymetry, no landslide evidences could be found off Bali or Lombok. As both islands feature high population densities, we investigate the possible impact of a slope failure south of Bali. Assuming that sediment properties are similar, we model an event that resembles slide F in volume and geometry, but is located 250 km south of Bali, at the seaward slope of the accretionary wedge (115.25° E, 11.12° S). Slide F constitutes the largest event in our study region (20 km³), so this test event can be considered as a worst case scenario.

As mapped in Figure 2.6b, the first wave arrives at Bali and Lombok after almost 30 minutes. Offshore wave heights reach 2 m off Bali, 1.5 m off Lombok and decrease rapidly when entering the straits between the islands. Calculated run-up heights (Figure 2.6a) reach nearly 4 m in Benoa, 2 m at Sanur beach and only 1 m in Kuta, which appears to be sheltered by the Bukit peninsula. Run-up on the southern coast of Lombok ranges around 4 m. These values somewhat depend on the assumed failure location. Moving the slide 70 km westward increases the run-up in Benoa up to 5 m while decreasing it in Lombok down to 2 m. Alternatively, moving the event 70 km eastward yields 3 m for Bali and 5 m for Lombok. Depending on current tidal conditions, these run-up values could be modified by ±1 m (UHSLC).

In a recent publication (see this thesis, chapter 5), we address the possibility of real-time submarine landslide detection by means of coastal tiltmeters. This technique relies on the fact that a displacement of several cubic kilometers of sediments leads to considerable and measurable land surface inclination inside some predicted radius. We apply this technique to check if a motion of our hypothetical slide could be tracked by tiltmeters on Bali or Lombok Island. Unfortunately, the distance to the coast appears to be so large, that even most accurate land-based tiltmeters cannot detect the event.

2.7 Conclusions

We identified six submarine landslides in new, high-resolution bathymetry data along the eastern Sunda trench. Three small events which involved between 1 and 4 km³ of sediments are located off Java, Lombok and Sumbawa. The remaining three landslides of significantly larger volumes (between 15 and 20 km³) are found at the margin toe off Sumba and Sumbawa.

Numerical modeling of landslide-generated tsunamis suggest that the largest events might have generated run-up heights of 7 m at Sumba, more than 5 m on Sumbawa and 3 m at Lombok Island. Maximum run-up on Bali and Java did not exceed 2 m.

As four slides are located directly above the assumed fault plane of the 1977 Sumba M_w=8.3 earthquake, we investigated if evidences for seismic landslide triggering could be revealed with the help of numerical modeling. Comparison of the measured run-up heights to our tsunami simulations show that the earthquake tsunami model alone adequately explains the observations. This fact cannot, however, exclude co-seismic landslide triggering: the potential landslide tsunami might have propagated shortly after the earthquake tsunami so that the waves did not measurably superpose at the survey point. Hence, based on the available data, we can neither support, nor decline the hypothesis of seismic triggering by the 1977 Sumba earthquake.

As the largest landslides are located off Sumba, the resulting run-up at the highly populated islands of Bali and Lombok was comparatively small. To estimate the

potential impact of a large-size slope failure near Bali and Lombok, we modeled an event similar to slide F (20 km³) but located 250 km off Bali. Despite the large distance to the coast, this landslide could generate a tsunami with run-up heights of about 4 m at both islands, thus posing a significant hazard to the population and industry centers.

2.8 Auxiliary material: Study of run-up estimation

The run-up formula that we apply can be evaluated at any depth d that is bigger than the wave height itself (Chesley and Ward 2006): $R = A(d)^{4/5} \cdot d^{1/5}$, where A is the wave amplitude, measured at water depth d. To check the stability of run-up predictions in our models, we systematically vary the depth d between 250 m and 20 m while observing the resulting run-up heights. This parametric study is done near Sedjorong, southwest Sumbawa, as it is located in the center of our study area (see Figure 2.3). Other places, however, show very similar characteristics. The run-up formula is applied at six different positions off-shore (Figure 2.7a) for five tsunami models, generated by slides B to F (Figures 2.7b to 2.7f, respectively). In these figures, the input wave height $A(d)$, which is the maximum wave height from the propagation simulation, is shown by the black portion of each bar. The whole bar represents estimated coastal run-up R. As indicated above the bars, gauges are sorted from left to right with decreasing depth d.

Off-shore wave heights $A(d)$ increase continuously by a factor of at least 2 during the shoaling process. Predicted run-up tends to increase as well, however, with distinctly smaller amplification factors. Generally, run-up estimates of the same event vary not more than 20 %. This means that the run-up formula can be applied at any depth between 250 m and 20 m without significantly affecting the final result.
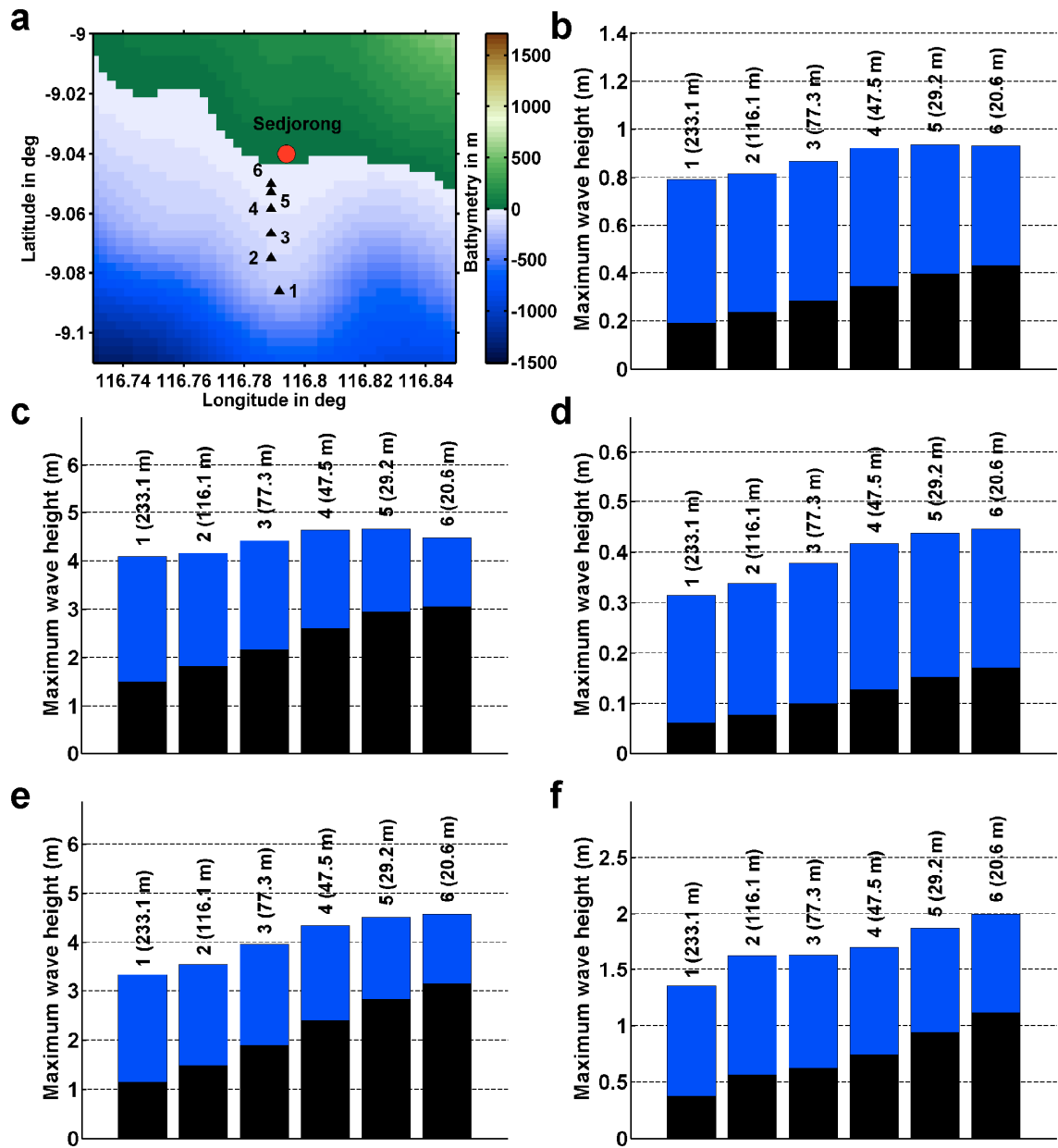
Figure 2.7 *Testing run-up predictions according to the relation of Chesley and Ward (2006) for consequently decreasing depths of reference points. (a) Virtual gauge positions. The location of Sedjorong is mapped in Figure 2.3. (b-f) Black bars designate computed offshore wave heights (at reference points). Blue bars show extrapolated run-up values. Labels are gauge numbers with respective depths. Subplot numbers b to f correspond to slide scenarios B to F, respectively.*

Chapter 3

Hazard assessment of underwater landslide generated tsunamis: a case study for the Padang region, Indonesia

Sascha Brune [1], Andrey Y. Babeyko [1], Christoph Gaedicke [2], Stefan Ladage [2]

[1]*Helmholtz Centre Potsdam GFZ German Research Centre for Geosciences, Potsdam, Telegrafenberg, 14473 Potsdam, Germany*
[2] *Federal Institute for Geosciences and Natural Resources (BGR), Stilleweg 2, 30655 Hannover, Germany*

Abstract
Submarine landslides can generate local tsunamis with high run-up, posing a hazard to human lives and coastal facilities. Both historical (giant Storegga slide off Norwegian coast, 8200 years BP) and recent (Papua New Guinea, 1998) events show high potential danger of tsunamigenic landslides and the importance of mitigation efforts. This contribution presents newly discovered landslides 70 km off Padang (Western Sumatra, Indonesia), based on recent bathymetry measurements. This highly populated city with over 750.000 inhabitants exhibits high tsunami vulnerability due to its very low elevation. We model tsunamis that might have been induced by the presented landslide events. Estimation of the corresponding inundation heights for the Padang area and other locations in the northern Mentawai fore-arc basin yields maximum run-up heights of about 2 m. We also provide a systematic parametric study of landslide-induced tsunamis which allows to distinguish potentially dangerous scenarios for Padang. Inside the fore-arc basin, scenarios involving volumes of 0.5 to 25 km³ could endanger Padang. Apart from slide volume, the hazard distribution mainly depends on three landslide parameters: distance to Padang, water depth in the generation region and slide direction.

3.1 Introduction

Tsunamis can arise from submarine earthquakes or landslides, threatening human lives and infrastructures in coastal areas. Large parts of Indonesia are particularly prone to tsunami danger as being located adjacent to the Sunda subduction zone. Here, the Indo-Australian plate subducts beneath the Sunda continental subplate at convergence rates of about 6 cm/yr (Chlieh et al. 2008). The continuing accumulation of stress leads to a high earthquake potential (Hamzah et al. 2000). In 1994, an earthquake generated a tsunami off Eastern Java that reached a maximal run-up of 14 m (Tsuji et al. 1995a). Ten years later, the Great Sumatra-Andaman Earthquake of December, 2004 generated a tsunami that inundated the coasts of Indonesia, Thailand, Sri Lanka and India, but also of several East African countries (Synolakis and Kong 2006). In 2006, Central Java experienced an earthquake tsunami with maximum inundation heights of more than 20 m (Lavigne et al. 2007; Fritz et al. 2007). But even moderate earthquakes can induce tsunamis by triggering submarine mass failures. The most prominent event of this kind is the 1998 Papua New Guinea tsunami, where an underwater slump of 4 km³ led to maximum wave heights of 15 m at the 30 km distant coast line (Tappin et al. 2001; Sweet and Silver 2003). In Indonesia, the involvement of submarine landslides has been proposed for the 1979 tsunami at Lomblen Island as well as for the 1992 event at the northern coast of Flores Island (Tsuji et al. 1995b; Rynn 2002). Bathymetry measurements at the trench off Sumba Island revealed large landslides with estimated volumes of up to 95 km³ (This thesis, chapter 2). Whether the extreme run-up at Nusa Kambangan during the Central Java tsunami of 2006 should be attributed to a landslide, is current matter of debate (Matsumoto et al. 2007). West of Sumatra, submarine slides have been discovered during the cruises that followed the 2004 earthquake. Moran and Tappin (2006) describe blocky debris avalanches at the foot of the accretionary prism west of the Aceh basin. The largest out-runner block measures 2 km in length and 1 km in width.

In recent years, numerical modeling has become a useful tool to estimate the hazard due to submarine landslides. Several landslide tsunami models have been developed and applied anywhere in the world. For detailed descriptions, see Harbitz (1992), Imamura and Imteaz (1995), Tinti et al. (1997), Grilli and Watts (1999), Pelinovsky (2001), Lynett and Liu (2002) and references therein.

In this study, we investigate the hazard potential of landslide-generated tsunamis near the city of Padang, situated in West Sumatra at the northern part of the Mentawai fore-arc basin. Padang, with more than 750.000 inhabitants, is one of the largest cities of Sumatra. As it is located on low coastal plains, its vulnerability in the case of tsunami arrival is particularly high. Moreover, recent studies indicate an elevated probability of a large earthquake in this region due to long-period strain accumulation by plate coupling (Chlieh et al. 2008) and Coulomb stress transfer after the 2004 and 2005 Sumatran earthquakes (McCloskey et al. 2008).

After a short description of the geological background, we present new high-resolution bathymetry data collected by the RV "Sonne" in 2006 exhibiting three landslide events inside the Mentawai basin, 70 km off Padang. Derived landslide parameters are then employed for the numerical modeling of potentially generated tsunamis. Finally, we provide a systematic parametric study of landslide-induced tsunamis offshore Padang. The idea of this study is to derive landslide and tsunami scenarios which might be dangerous for the city of Padang.

3.2 Geological background

Our study area comprises the northern part of the Mentawai Basin which is one of several depositional basins located off Sumatra along the Sunda Arc. The latter is a classical convergent margin system that stretches over 5000 km from Sumba Island in the southeast to Burma in the north. The arc is the geological expression of the convergence between the Indo-Australian and the Eurasian Plate where oceanic lithosphere is being subducted beneath the Indonesian island arc as well as the Andaman and Nicobar Islands. The Mentawai Basin is the widest and longest fore-arc basin off Sumatra extending over 550 km from the southern tip of Sumatra to the Batee Islands in the north. To the west, it is bordered by the outer arc high that, merging above sea level, forms the Mentawai Islands (from Siberut to Enggano). The basin has a maximum width of 140 km between the island of Siberut and Sumatra. The Battee Islands separate the Mentawai Basin from the northerly located Nias basin. West off the Sunda Strait the outer arc high broadens forming a slightly shallower ridge that separates the Mentawai Basin from the West Java Basin (Susilohadi et al. 2005).

Geometry is uniform in the entire basin. The depth of the sea floor reaches 1700 m in the Mentawai Basin off Padang. The sediments are up to 4.8 s two-way travel time (TWT) thick, which, assuming a sound speed of 1500 m/s (Hamilton 1985) corresponds to approximately 3600 m. The minimum thickness along the basin axis is 3.5 s TWT, or roughly 2600 m. The acoustic basement underlying the sedimentary succession dips from the Sumatran shelf to the south-east where the maximum depth is reached close to the outer arc high.

The basin fill consists of terrigenous hemipelagic sediments with parallel, highly continuous reflections of medium to strong amplitude. Within the basin fill, some minor unconformities occur. Along the Sumatra margin multiphase sea level changes are documented in prograding and retrograding delta complexes below the shelf. This delta wedge gives evidence that Sumatra is the main source area for sediments deposited in the Mentawai Basin. Slump structures and debris flows exhibited in multi-channel seismic profiles give evidence for ancient slope failures in these delta complexes (Neben and Gaedicke 2006).

Ground motions during earthquakes pose the main trigger for submarine landslides (Masson et al. 2006). The Mentawai segment of the Sumatra subduction zone is capable of producing earthquakes with magnitudes bigger than 8.5. This happened
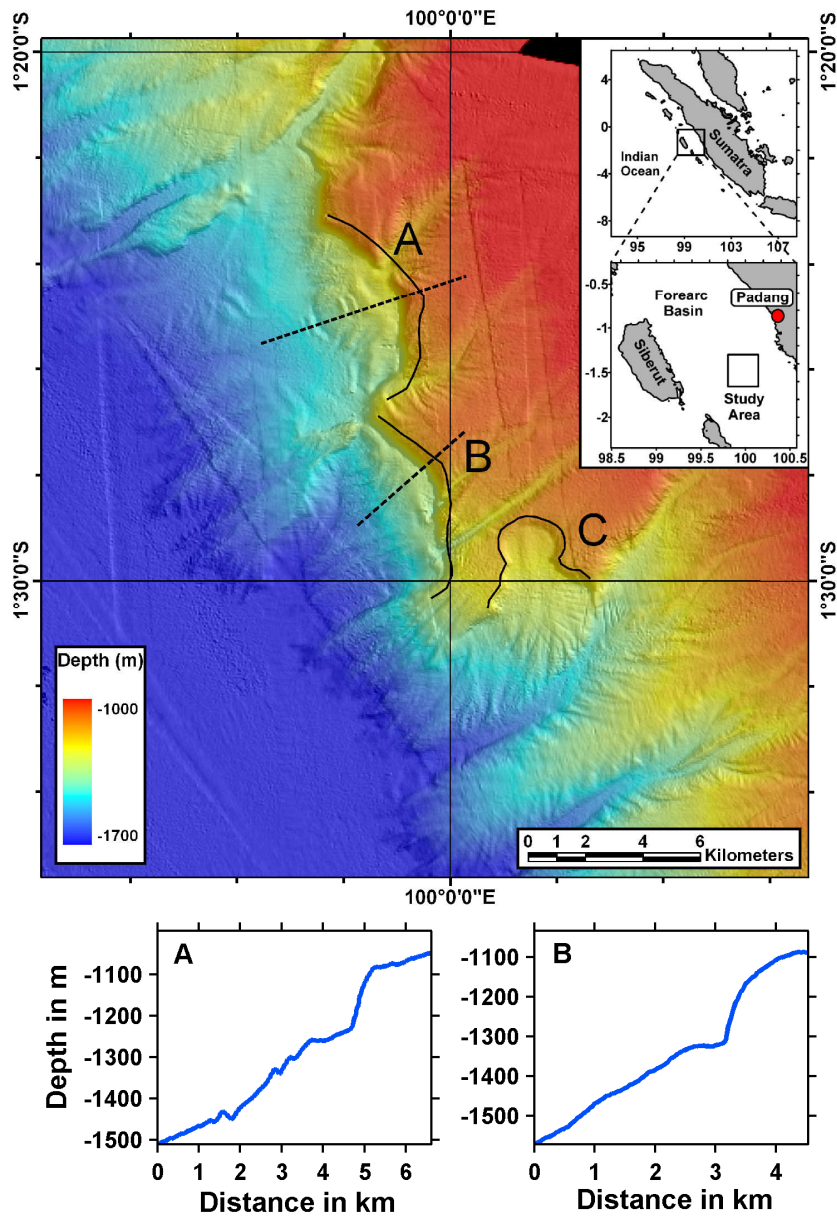
Figure 3.1 *Bathymetry map of submarine landslides 30 km off Padang. Solid lines are head scarp interpretations. Dashed lines indicate locations of cross sections profiles of the events A and B.*

both in 1797 and in 1833, generating large tsunamis (Natawidjaja et al. 2006). It is current matter of debate, whether a comparable event in this area could recur soon (McCloskey et al. 2008; Chlieh et al. 2008). In September 2007, a series of earthquakes occurred west of Bengkulu, within the fault area of the 1833 rupture. Although magnitudes of 8.4 and 7.9 were reached, these events did not release the stress that was accumulated since 1833 (Lorito et al. 2008; Borrero et al. 2007; Chlieh et al. 2008).

3.3 Slide descriptions
During the SO189 cruise of the RV Sonne, west of Sumatra, new high-resolution bathymetry data was collected. Resolution in the fore-arc basins amounts to about

	Slide A	Slide B	Slide C
Width w (km)	6	6	2.5
Length (km)	3	2	2.5
Height (m)	100	100	50
Volume (km³)	0.7	0.5	0.1
Depth (m)	1200	1300	1300
Travel Distance (km)	2	1.5	2
Mean local slope angle (°)	5	6.5	3
Initial wave height η_{2HD} (m)	2.0	2.1	0.2
Characteristic wave length λ (km)	7	5	9
Characteristic time t_0 (s)	60	40	70

Table 3.1 Geometric landslide parameters. Width is measured perpendicular, and length parallel to the slope. For volume estimations, a parabolic slide form is assumed. Travel distance designates the approximate center of mass dislocation length. Mean local slope angles are inferred from bathymetry cross-sections of slide areas. The tsunami hot start parameters (initial wave height, wave length and characteristic time) have been calculated according to Watts et al. (2005).

50 m. The new data reveals a landslide site at the foot of the eastern fore-arc basin slope, within 70 km distance to the city of Padang. The site consists of three sub-events exhibiting concave head scarps up to 150 m height (Figure 3.1). In the following, we will refer to them as slide A, B, and C, respectively.

At the foot of slide A, compressional features can be clearly observed in the bathymetry. We interpret them to be the lower end of the failure surface and suggest rotational slumping as a corresponding failure mechanism. The slump width and length amount to 6 km and 3 km, respectively (Table 3.1). By comparing disturbed and undisturbed profiles, the thickness of the slump was estimated to be 100 m. Event B shows similar parameters to slide A, except for a shorter length of approximately 2 km. The last sub-event, slide C, which is located at south-east, is much smaller than the previous ones. The height of the head scarp amounts to 50 m. Furthermore, the head wall is divided into several segments indicating that failure took place in multiple stages. Assuming parabolic cross sections, we estimate the volumes of slide A, B, C to be 0.7, 0.5, and 0.1 km³, respectively.

Available parasound data lines cross the slide locations A and B (not shown here). Within the slide areas, parasound data display undisturbed, stratified sediments. The penetration depth in the sediments is 0.06 ms TWT which (if we assume a

sound speed of 1500 m/s (Hamilton 1985)) corresponds to 50 m. Thus, the failure surface lies deeper than 50 m which is in agreement with our previous height estimation of 100 m. As the parasound lines are located perpendicular to the slide directions, no information can be obtained about the rotation angle of the slumps. Side scan images have been evaluated, as well. They clearly show head scarps, but do not display any additional details.

Dating of submarine landslides, based only on bathymetric data is difficult. However, the escarpments of event A and B are disturbed by small canyons. As these erosional features evolve quite slowly, the events must have happened a relatively long time ago.

3.4 Modeling of induced tsunamis
3.4.1 Methods
We model landslide-generated tsunamis in three distinct stages: generation, propagation and run-up. For the generation phase, we follow the wavemaker technique of Watts et al. (2005) and Grilli et al. (2005). Combining physical arguments and wave tank experiments, they produced a set of semi-empirical equations for two horizontal dimensions (2HD) that yield the initial tsunami wave height η_{2HD}, wave length λ and a characteristic time t_0. According to the wavemaker technique, the influence of a submarine mass movement on the sea surface can be approximated by an initial wave distribution. During the acceleration phase of a slide, the most important part of wave energy is used for the build-up of the wave. When the slide does not accelerate anymore, i.e. after the characteristic time t_0, this potential energy is transformed into kinetic energy. We construct the initial wave distribution by analogy to Synolakis et al. (2002) and Watts et al. (2005): The first-order impact of a submarine mass failure on the sea surface consists of vertical uplift in direction of the movement and subsidence in backward direction. First, we consider a slide for one horizontal dimension (1HD). We approximate the elevated and the subsided water surface using two Gaussians. The amplitude of each curve is the initial wave height η_{1HD}, and its width equals to the characteristic wave length λ. Their center points are located at a distance of one wave length from each other. This waveform would be feasible for 1HD simulations. 2HD formulation additionally requires a waveform description in the direction perpendicular to the slide movement. Watts et al. (2005) proposed a solitary-like extrapolation proportional to sech²$(3 \cdot y/(w+\lambda))$, where w is the slump width and y the coordinate perpendicular to the slide direction. Hereby, due to mass conservation, the wave amplitude has to be modified. Watts and his coworkers suggest the multiplication of η_{1HD} with $w/(w+\lambda)$, to obtain the 2HD wave amplitude η_{2HD}. The values of η_{2HD}, λ and t_0 for slides A, B, and C are listed in Table 3.1.

The scope of application for this method is discussed in Watts et al. (2005). The ratio of initial submergence depth to slide length must be larger than 0.06 in order

to avoid wave breaking effects, which are not included in the model. For our slides A to C, this ratio amounts to 0.29, 0.32, and 0.43, clearly satisfying the condition.

Alternative 2HD formulations exist that use a submerged slide body which dynamically builds up a surface wave (see chapter 4 and 5 of this thesis). They have been implemented in either shallow-water (Harbitz 1992) or Boussinesq approximation (Lynett and Liu 2005). Although these formulations allow to implement specific features of a landslide, their validity is restricted by submergence depth and length of the slide. As shown by Lynett and Liu (2002), shallow-water models of dynamic landslides are only feasible, if the ratio of slide length to submergence depth is larger than 30. More accurate Boussinesq formulations are valid if the ratio exceeds 7. These values hold true for symmetrical slide geometries, as discussed in Lynett and Liu (2002). In our case though, the length to depth ratios are clearly below the threshold: 2.5, 1.5 and 1.9 for slide A to C, respectively. For a detailed numerical study of deep or small slides, the usage of fully 3D, or 2HD-vertical models based on Reynolds averaged Navier–Stokes equations (RANS) (Yuk et al. 2006) or Fully Nonlinear Potential Flow (FNPF) (Grilli et al. 2002) would be promising. It is worth noting that the semi-empirical formulation used in the present study was validated by a FNPF model (Grilli et al. 1999) and is an efficient means for rapid estimation of characteristic parameters of landslide-generated tsunamis.

Tsunami wave propagation is calculated using the finite difference model TUNAMI-N2 (Imamura et al. 1997). This nonlinear shallow water code uses the staggered leap-frog scheme for discretization of time and space. The shallow water approximation is fulfilled, as all wave lengths are much bigger than the water depth. Wave propagation is calculated on a 920×760 grid using a spatial step size Δx of 10 arc seconds (~309 m) and a time step Δt of 0.5 s. The influence of resolution was tested by variation of both Δx and Δt, further refinement did not change the results. Bathymetry is based on interpolated GEBCO data (IOC, IHO and BODC 2003).

We extrapolate offshore wave heights to final run-up values using the formula of Chesley and Ward (2006): $R = A(d)^{4/5} \cdot d^{1/5}$, where $A(d)$ is the wave amplitude, measured at water depth d. This formula was developed based on the conservation of wave energy flux and tested for both breaking and non-breaking waves (Ward and Asphaug 2003). In this study, we apply the run-up formula at water depths of about 50 m.

3.4.2 Results
First, we consider each slide independent of the others. Slide A induces a wave reaching Siberut after 20, and Padang after 25 minutes (Figure 3.2). The maximum wave height at the virtual gauge off Padang, in a water depth of 50 m, is 0.35 m. This corresponds to a run-up of about 0.9 m at Padang. The highest run-up of 2.3 m is found south of Padang, in Pasar Sungainjalo. Run-up at the Siberut Island
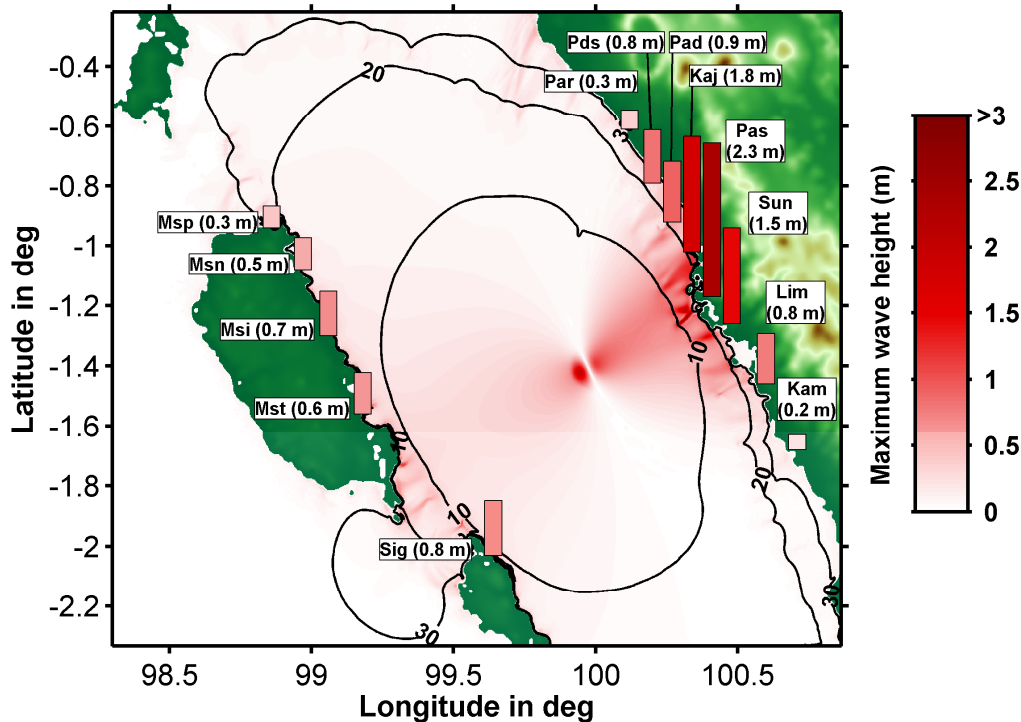
Figure 3.2 Tsunami generated by slide A. Maximum wave height distributions after 2 hours and arrival times in minutes. Run-up along the coast is mentioned in parentheses and depicted as colored bars. Abbreviations stand for following places: Par: Pariaman, Pds: Padangsarai, Pad: Padang, Kaj: Kajuara, Pas: Pasar Sungainjalo, Sun: Sungaitalang, Lim: Limaumanis, Kam: Kambang, Sig: Sigoisooinan, Mst: Muarasiberut, Msi: Muarasaibi, Msn: Muarasikabaluan, Msp: Muarasigep.

does not exceed 0.7 m. The slightly smaller slide B shows similar results (Figure 3.3). It generates 2.1 m run-up in Pasar Sungainjalo as well as 0.6 m in Padang and at Siberut. The third event, slide C, induces only a small tsunami. Although we do not take into account multiple stage failure, which would further reduce the wave heights, run-up values do not exceed 0.3 m.

The next model assumes simultaneous failure of the events A and B. As the two landslides are located alongside, an earthquake that led to the failure of one slide might have also triggered the other. The natural worst case scenario hereby consists of the superposition of both initial wave forms at the same moment. This scenario yields a maximum run-up of 3.2 m in Pasar Sungainjalo and 2.3 m at Sungaitalang (Figure 3.4). Both places are located in a zone where run-up values are significantly augmented by positive interference. However, some places experience negative interference. For example, in Kajuara, the run-up of the combined scenario is smaller than that for every single event.

The above run-up values are obtained without considering tidal oscillations. As high tides reach approximately 0.7 m above mean zero (UHSLC), the worst case run-up might be nearly 2 m at Padang and 3 to 4 m at locations south of Padang. Waves of this size are capable to endanger people and probably damage small
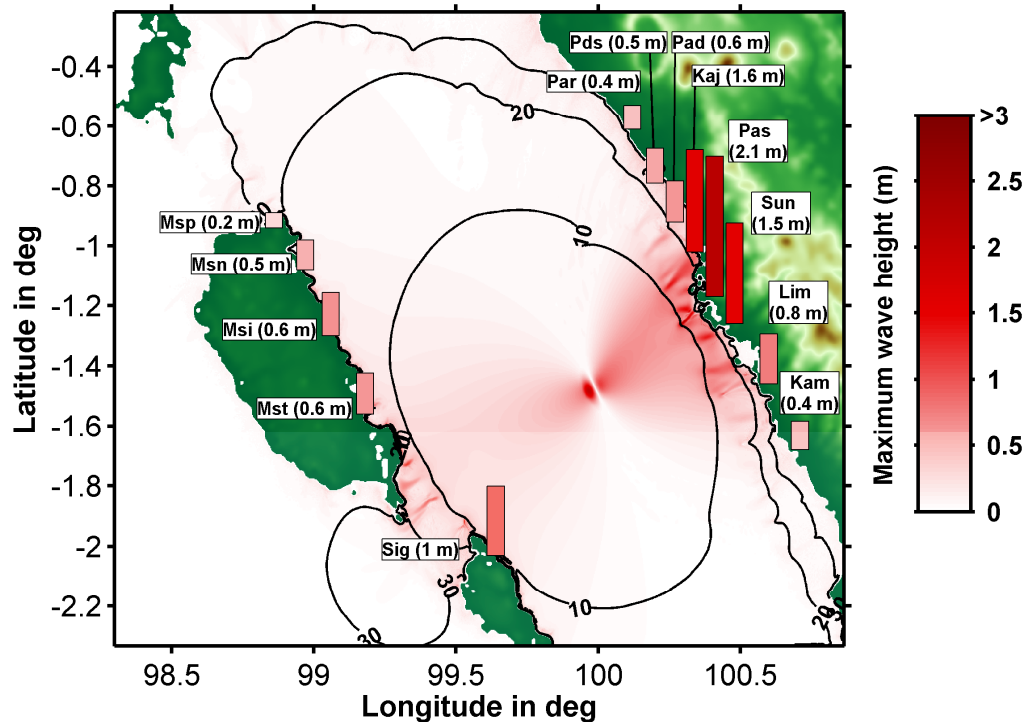
Figure 3.3 *Tsunami generated by slide B. Maximum wave height distributions after 2 hours, arrival times in minutes and run-up along the coast. For abbreviated place names, see caption of Figure 3.2.*

vessels and structures near the coast line (Papadopoulos and Imamura 2001). Additionally, if slides are triggered by an earthquake, superposition of the waves to an earthquake tsunami is possible.

While slide geometry and travel distance of event A can be estimated from bathymetric data quite accurately, both length and travel distance of slide B are subjected to a higher uncertainty. Parameter studies show that this uncertainty could be responsible for run-up variations of ~20 % for slide A and ~50 % for slide B.

3.5 Spatial aspect for landslide hazard assessment
In the previous section, we calculate tsunamis of given landslides and estimate whether they could have posed a danger for the city of Padang. In this section, we go a step further and investigate the tsunamigenic potential of a broad spectrum of hypothetical events in the Padang area. Hypothetical run-up in Padang depends not only on the size of the landslide, but also on its geographical location in the Mentawai Basin. The latter determines not only the distance to Padang, but also submergence depth and slope direction. The main question we want to address is: how large must a submarine landslide at a given location be, in order to induce dangerous (>2 m) run-up at Padang.

To answer this question, we systematically model landslides located on the nodes of a 0.25-degree structured grid off Padang (Figure 3.5). We ignore locations at the
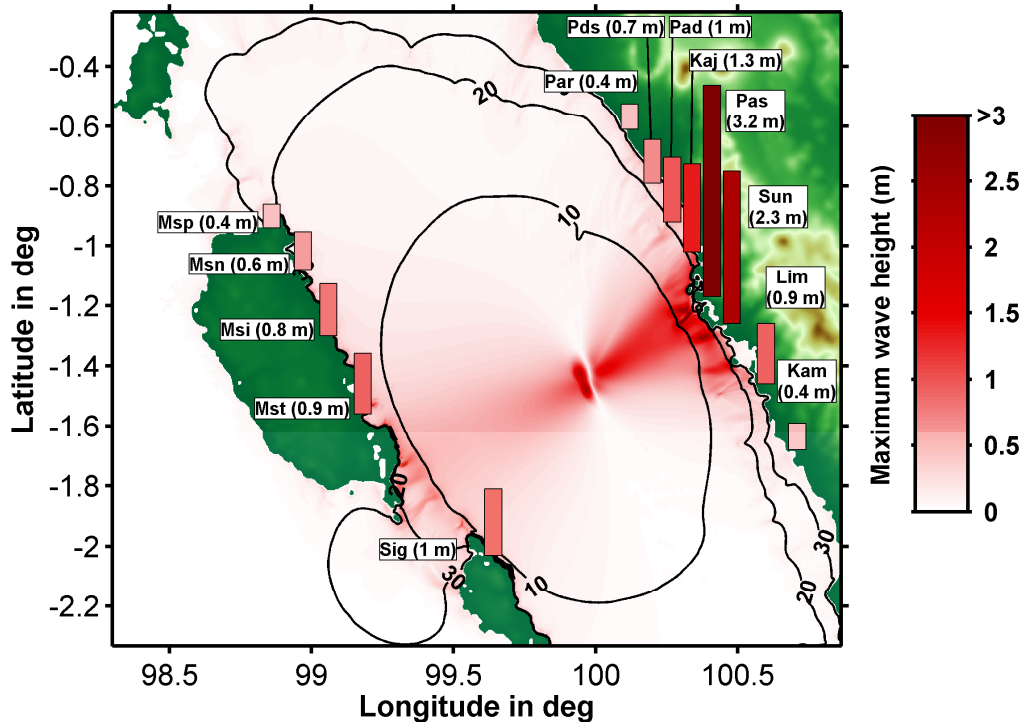
Figure 3.4 *Worst case tsunami generated by slides A and B simultaneously. Maximum wave height distributions after 2 hours, arrival times in minutes and run-up along the coast. For abbreviated place names, see caption of Figure 3.2.*

bottom of the fore-arc basin due to vanishing slope angles as well as places of very shallow water depth, where the model applicability mentioned in section 3.4.1 is exceeded. At each of the 32 resulting positions, we simulate 14 landslides of different volumes, ranging from 0.5 to 25 km³. We prescribe the direction of motion to be down slope along the negative bathymetry gradient. In order to minimize the number of parameters, we consider events with radial symmetry and a constant width. All these synthetic events follow properties of the real events A and B. Namely, we assume rotational slumping as fault mechanism, a slump width and length of 5 km and fix the center-of-mass travel distance to 2 km. Landslide thickness varies between 13 m and 640 m to reach slide volumes from 0.5 km³ to 25 km³, respectively. Theses large slide heights are realistic, as the Papua New Guinea event involved a height of 600 m as well (Tappin et al. 2001; Sweet and Silver 2003). We mark a landslide as dangerous if it induces at least 2 m run-up in Padang.

Whether a landslide at a certain location can induce a dangerous tsunami in Padang, is primarily dependent on its volume. Figure 3.5 maps the smallest landslides which generate more than 2 m run-up in Padang. An event at the same location, but with a larger volume will always generate a larger tsunami. Thus, the scenario with the smallest volume represents the lower end of the hazard potential at this position.
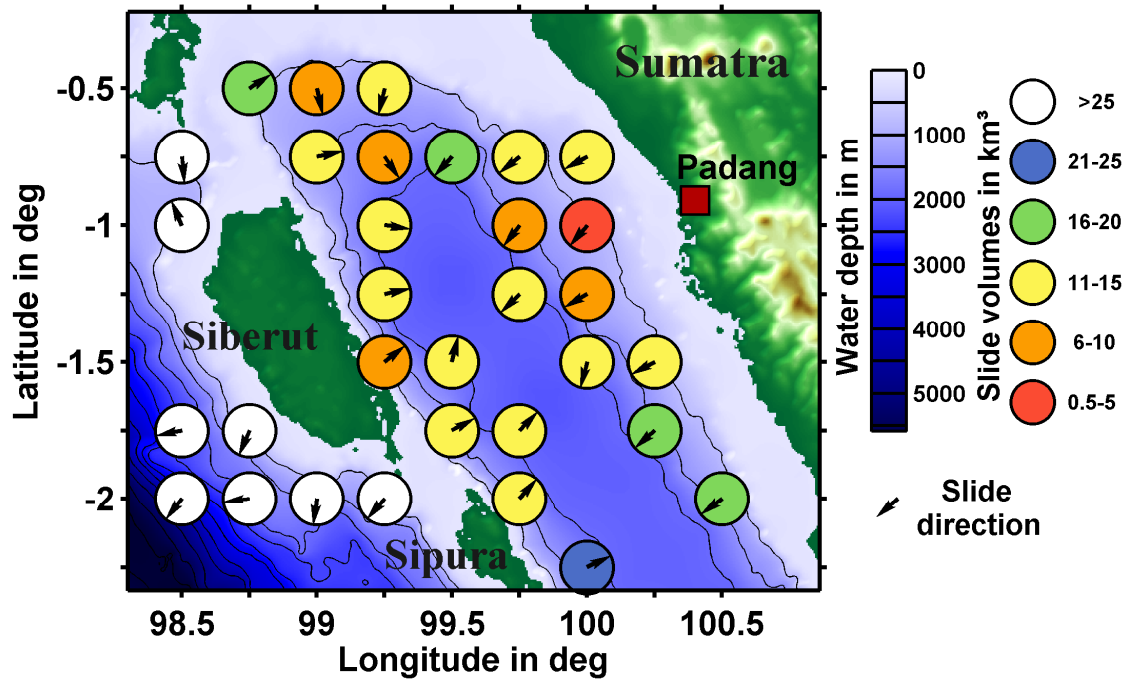
Figure 3.5 *Spatial hazard assessment for landslide-generated tsunamis off Padang. Colored circles represent the location and the* smallest *volume of a landslide capable to generate 2 m run-up in Padang. Arrows inside the circles depict slide directions. Contour lines show water depths at 500 m intervals.*

Analysis of Figure 3.5 shows that the water depth in the generation region is a major parameter. Initial wave heights decrease for increasing depth. The reason lies in the dynamical build up of the wave. The tsunami propagation velocity augments with water depth. If this velocity becomes larger than the speed of the submarine slide itself, the generated tsunami wave starts to spread out while the slide movement still modifies the water surface. As a result, deeper slides generally cause smaller initial wave heights.

A second major parameter is the distance between the landslide and Padang. The amplitudes of landslide tsunamis decay comparatively fast, due to geometrical spreading of the wave and the dipolar slide nature (Okal and Synolakis 2003). Thus, it is mainly the interplay of depth and distance that results in the complex distribution shown in Figure 3.5. At areas where both depth and distance to Padang increase their effects interfere positively. This is the case directly off Padang. At the location (100°, -1°), even a comparatively small volume suffices to yield dangerous run-up. Further off shore, slide volumes have to increase in order to induce more than 2 m run-up. At the opposite site of the fore-arc basin, the situation perspective is mirrored. Here, larger distance implies shallower depth. As a result, a smaller but shallower (600 m water depth) slide at (99.25°, -1.5°) is as dangerous as a larger but much deeper (1500 m water depth) event located closer to Padang (99.5°, -1.5°).

A parameter that locally influences the hazard distribution is the slide direction. A landslide-generated tsunami is largest in the direction of slide motion, and, due to refill, in the negative direction as well. In the perpendicular direction, waves interfere destructively. This can be seen for example in the maximum wave height distributions at Figures 3.2, 3.3 and 3.4. The same holds true for the scenario at (100°, -1) and its northern neighbor (100°, -0.75°) (Figure 3.5). In case of the latter event, the zone of negative interference is directed towards Padang. Thus, despite similar water depth (600 m and 300 m, respectively) and equal distance to Padang, the minimal dangerous slide volume is much larger for the northern event. A similar situation can be found for the locations (98.75°, -0.5) and (99°, -0.5), with respective water depths of 600 and 700 m. The eastern scenario releases its energy into the basin and requires a much smaller volume than the former event.

Possible landslides outside the fore-arc basin pose no danger for Padang within the studied volume range. Siberut Island and the outer fore-arc high reflect most of the wave energy into the open ocean and thereby shield the coast of Sumatra.

In this study, we focus on the hazard assessment. To deduce the associated risk, one has to consider the probability of an event. Little is known about the frequencies of submarine landslides in this region, due to their low detectability. Apart from the landslides presented in this paper, we found five additional events within bathymetry data of the fore-arc basins near Sumatra. None of these events exceeded a volume of 5 km³. Thus, we estimate that the probability of an event to be larger than 5 km³, is rather low, but no statistical evaluation is possible due to the small number of events.

3.6 Conclusions

Three landslides have been detected in the Mentawai fore-arc basin, 70 km off Padang. Their volumes were estimated to be 0.7 km³, 0.5 km³ and 0.1 km³. The slides show erosive features, so a recent failure can be excluded. We numerically modeled the generated tsunamis using a semi-empirical technique for the evaluation of initial wave height and characteristic wave length. Tsunami propagation was computed with a non-linear, finite difference, shallow water code. Finally, we applied an empirical law to calculate run-up at the coast. Our results show 1 m run-up in Padang for the two largest events A and B. Maximum run-up of about 2 m was calculated south of Padang, in Pasar Sungainjalo, which is located closer to the slide area. The third landslide did not generate a significant tsunami. Under high tide conditions, run-up would increase by roughly one meter. If the two large events happened simultaneously, the resulting tsunami waves would superpose, possibly reaching run-up heights of more than 3 m.

Finally, we performed a hazard assessment study for the city of Padang, answering the question of how large a submarine landslide at a given location has to be, in order to generate dangerous (>2 m) run-up at Padang. Inside the fore-arc basin, dangerous scenarios exhibit volumes between 0.5 and 25 km³, while outside the

basin volumes smaller than 25 km³ do not pose any danger for Padang. The main three landslide parameters which control the hazard distribution of landslide-generated tsunamis are: distance to Padang, water depth in the generation region and slide direction.

Acknowledgements

Chapter 4

Tsunami modeling of a submarine landslide in the Fram Strait

Christian Berndt [1], Sascha Brune [2], Euan Nisbet [3], Jochen Zschau [2], and Stephan V. Sobolev [2]

[1] *IfM-Geomar, Wischhofstr. 1-3, 24148 Kiel, Germany; and National Oceanography Centre, European Way, Southampton, SO14 3ZH, U.K.*
[2] *GeoForschungsZentrum Potsdam, Telegrafenberg E3, 14473 Potsdam, Germany*
[3] *Department of Earth Sciences, Royal Holloway University of London, Egham, Surrey, TW20 0EX, U.K.*

Abstract
The present geological setting west of Svalbard closely parallels the situation off mid-Norway after the last glaciation, when crustal unloading by melting of ice induced very large earthquakes. Today, on the modern Svalbard margin, increasing bottom water temperatures are destabilizing marine gas hydrates, which are held in continental margin sediments consisting of inter-layered contourite deposits and glacigenic debris flows. Both unloading earthquakes and hydrate failure have been identified as key factors causing several mega-landslides off Norway during early Holocene deglaciation. The most prominent event was the Storegga slide 8200 years BP which caused a tsunami up to 23 m high on the Faroe and Shetland Islands. Here we show by numerical tsunami modeling that a smaller submarine landslide west of Svalbard, 100 m high and 130 km wide, would cause a tsunami capable of reaching northwest Europe and threatening coastal areas. We propose a novel tsunami warning tool based on tiltmeters yielding a warning time of one to four hours.

4.1 Effects of global warming on the Arctic
Continental margins that are influenced by glacial processes are subject to large-scale slope failures primarily at their trough mouth fans. The Norwegian margin
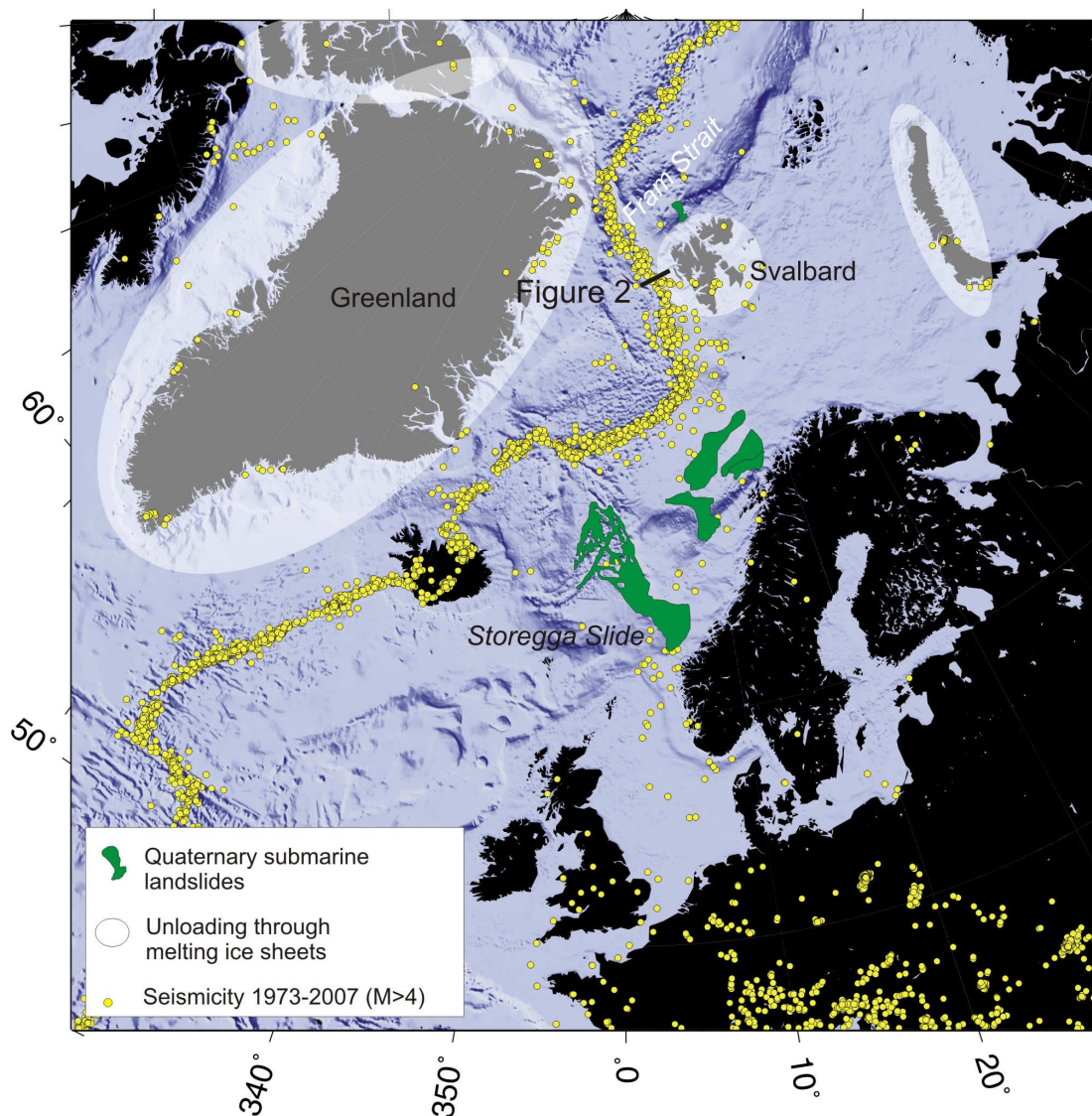
Figure 4.1 *Overview map of the Atlantic off northwest Europe, seismicity and quaternary landsides. The Fram Strait is located between the major ice-retreat areas of Greenland and Svalbard. Earthquakes occur on the rims of the ice sheets and along the mid ocean ridges. Shaded relief based on IBCAO.*

has experienced slope failures north of the North Sea Fan (Storegga slide) (Bugge et al. 1987; Haflidason et al. 2004, 2005). The 8.2 ka BP Storegga slide was associated with a very great earthquake such as the one that ruptured the whole crust over several hundered km (Arvidsson 1996). Other failures occurred at the termination of the Trænadjupet cross shelf trough (Trænadjupet Slide) (Laberg et al. 2003), at the end of the Andøya cross shelf trough (Andøya Slide) (Laberg et al. 2000; Lindberg et al. 2004), and on the Bear Island Fan (Bear Island Slide) (Laberg and Vorren 1993). Except for the Bear Island Slide all these slope failures occurred after the last deglaciation. The reasons for these slope failures are not fully understood, but the vulnerable interlayering of glacial debris flows and hemipelagic sediments, combined with mega-quake seismicity due to postglacial rebound were both probably important (Bryn et al. 2005; Kvalstad et al. 2005). A vital facilitating factor for destabilizing submarine slopes appears to be
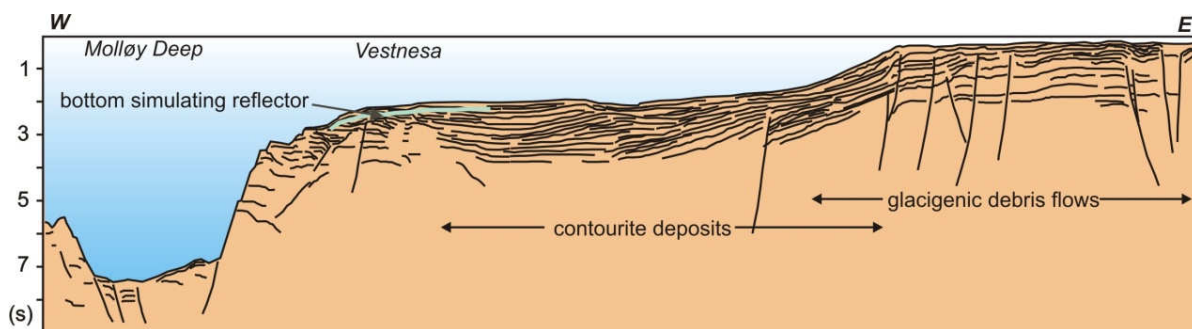
Figure 4.2 *Line-drawing of a transect from the Svalbard shelf through the gas hydrate province into the Molløy Deep, west of Spitsbergen (after Eiken et al. 1994).*

development of pore water overpressure for example after gas hydrate dissociation (Yung and Vogt 2001; Micallef et al. in press).

In this paper we investigate what would happen if the Kongsfjorden Trough Mouth Fan (KTMF) failed. The KTMF is located in the Fram Strait on the west coast of Svalbard (Figure 4.1), and is one of the few trough mouth fans that have not failed since the last deglaciation.

By the end of this century, average Arctic surface temperature may increase by 5 °C (Kattsov et al. 2004). Climate warming is causing loss of polar ice and glacier retreat (Rignot and Kanagaratnam 2006), and the reduction of ice load is already causing low frequency earthquakes that are significantly stronger than ice flow-related earthquakes in the past (Ekström et al. 2003; Turpeinen et al. 2008). Isostatic readjustment to the reduced ice load will cause the lithosphere to flex back or snap, as in the Storegga event (Arvidson et al. 1996) potentially triggering a large earthquake capable of setting off submarine landslides.

As well as sudden events, sea-bottom warming will also destabilize gas hydrate deposits (Westbrook et al. 2008b). Similar rapid warming happened before to northwest Europe at the end of the last glaciation. Gas hydrate dissociation releases free gas, increases pore pressure, and reduces effective stress and slope stability (Sultan et al. 2004). The system becomes primed for submarine slope failure, set off by a triggering earthquake. Although this mechanism is not proven so far, there is geomorphological evidence of hydrate involvement in the evolution of the Storegga slide (Micallef et al. in press).

The continental margins in the Fram Strait closely resemble the Norwegian margin prior to the Storegga slide (Figure 4.2): (a) both are characterized by an inter-fingering of glacial debris flow and interglacial hemipelagic sediments deposited at the mouth of a cross-shelf trough (Vanneste et al. 2005), (b) both have active fluid flow systems (Knies et al. 2004), (c) both are major gas hydrate provinces on the Atlantic margin of Europe (Westbrook et al. 2008a), and (d) both undergo rapid

uplift as the result of postglacial rebound. In particular, the inter-layering of glacial and interglacial sediments makes the slope less stable as the glacial sediments inhibit the normal dewatering of the water-rich interglacial sediments and allow pore pressure build up (Solheim et al. 2005b). As a result the Svalbard glacial margin has previously failed in giant landslides such as the Hinlopen Slide 300 km northeast of the Fram Strait (Vanneste et al. 2006). The fluid flow and in particular the warming of gas hydrates add to the risk of overpressure generation in the sediments (Sultan et al. 2004).

The present rate of uplift in Svalbard is 4-5 mm/yr (Sato et al. 2006). This is a superposition of the signal from the last glaciation and the present acceleration due to melting of ice. Similarly, 100 km³ ice per year are being lost from glaciers in Greenland and Iceland (Luthke et al. 2006). A rebound-related earthquake probably triggered the Storegga slide (Kvalstad et al. 2005) and it has been shown that earthquakes become more frequent in the Svalbard area as Greenland and Iceland adapt to the diminishing load (Ekström et al. 2003).

The sedimentation history and geometry, the presence of gas and the likelihood for future earthquakes as a trigger are all important prerequisites for a submarine landslide. However, whether the slope is indeed unstable also depends on the presence of weak layers, but their presence can only be established by expensive deep sea drilling. For this work we assume that these layers are present, because they developed in many other trough mouth fans: off Hinlopen, in the Bjoernoya Fan, off Andøya, in the Trænadjupet Fan, and in the North Sea Fan. Obviously the risk for future landslides is highest for the remaining fans that have not failed yet. Current geological and geophysical data suggest that the fan off Kongsfjorden has an active fluid flow system (Bünz et al. 2008; Westbrook et al. 2008a) and that there is significant seismicity in the area (Ekström et al. 2003). Because such evidence is lacking for other trough mouth fans in this region, we propose that it is the most likely site for a future failure of trough mouth fans in the North Atlantic.

The part of the slope off the KTMF that could be affected by slope failure is 30 to 130 km wide in east-west direction including the KTMF proper and the continental slope west of it including a continental promontory called Vestnesa. The north-south extent of a potential landslide is somewhat uncertain because the Arctic ice coverage limits the geological information available for the western side of the Yermak Plateau, but at least 130 km of slope show a similar geological setting as the margins that were affected by the Storegga and Trænadjupet slides (Bünz et al. 2008, Westbrook et al. 2008a).

Scenario	Volume (km³)	Lateral dimensions (km)	Travel distance (km)	Peak speed (m/s)	Maximal Froude number	Initial acceleration (m/s)
1	500	50 × 100	95	35	0.25	0.026
2	1000	70 × 130	60	35	0.35	0.039
3	1000	70 × 130	60	20	0.2	0.013
4	1000	70 × 130	95	35	0.25	0.026

Table 4.1 *Key modeling parameters. Travel distance designates the approximate center of mass dislocation length. Froude number is defined as the ratio of wave velocity to slide speed.*

4.2 Methods and results
4.2.1 Tsunami propagation
We use the finite difference, fully nonlinear Boussinesq code COULWAVE (Lynett and Liu 2002) to calculate tsunami wave propagation. The model can be applied, as long as the ratio of slide length to submergence depth is larger than 7. With a ratio of at least ~25, this is clearly the case. The change in sea floor topography due to dislocation of sediments is projected towards the sea surface. Thus the tsunami wave is build up dynamically as the slide propagates. We use North Atlantic bathymetry based on GEBCO (www.gebco.org), interpolated to 2.5 km bin size.

We approximate the sliding body with a two dimensional Gaussian surface. The lateral dimensions define the 'Full Width at Half Maximum' values of the Gaussian package. With the landslide slopes of a Gaussian curve being very gentle, the induced water movement is considered to be solely vertical. The sediment movement itself is approximated through a kinematic slide model. We adopt a velocity profile based on Løvholt et al. (2005) who composed the velocity function from sinusoidal curves so that the acceleration and deceleration curves are smooth. The velocity function is composed of parts of sinusoidal curves in a way that the acceleration/deceleration curve is smooth. The velocity profile is symmetrical and the sliding stops after approximately one hour. The shape of the velocity profile is relevant for the resulting tsunami (Hornbach et al. 2007), but as there are no contradicting geological constraints available for the study area, the Løvholt et al. (2005) model which was calibrated against the measured run-up heights of the Storegga slide is the most appropriate analogue.

We model four slope failure scenarios at the Svalbard margin. Scenario 1 consists of a 500 km³ landslide at the Svalbard slope that moves in westerly direction into the Fram Strait. It is restricted to the presently proven occurrence of gas hydrates with a 100 km long headwall and 50 km width (Vanneste et al. 2005; Westbrook et al. 2008a). The slide of 100 m incision transports sediments over a distance of 95 km and stops in the Fram Strait, when slope angles tend to zero. In Scenario 2, we assume that a significant part of the slope west of Kongsfjorden is unstable.
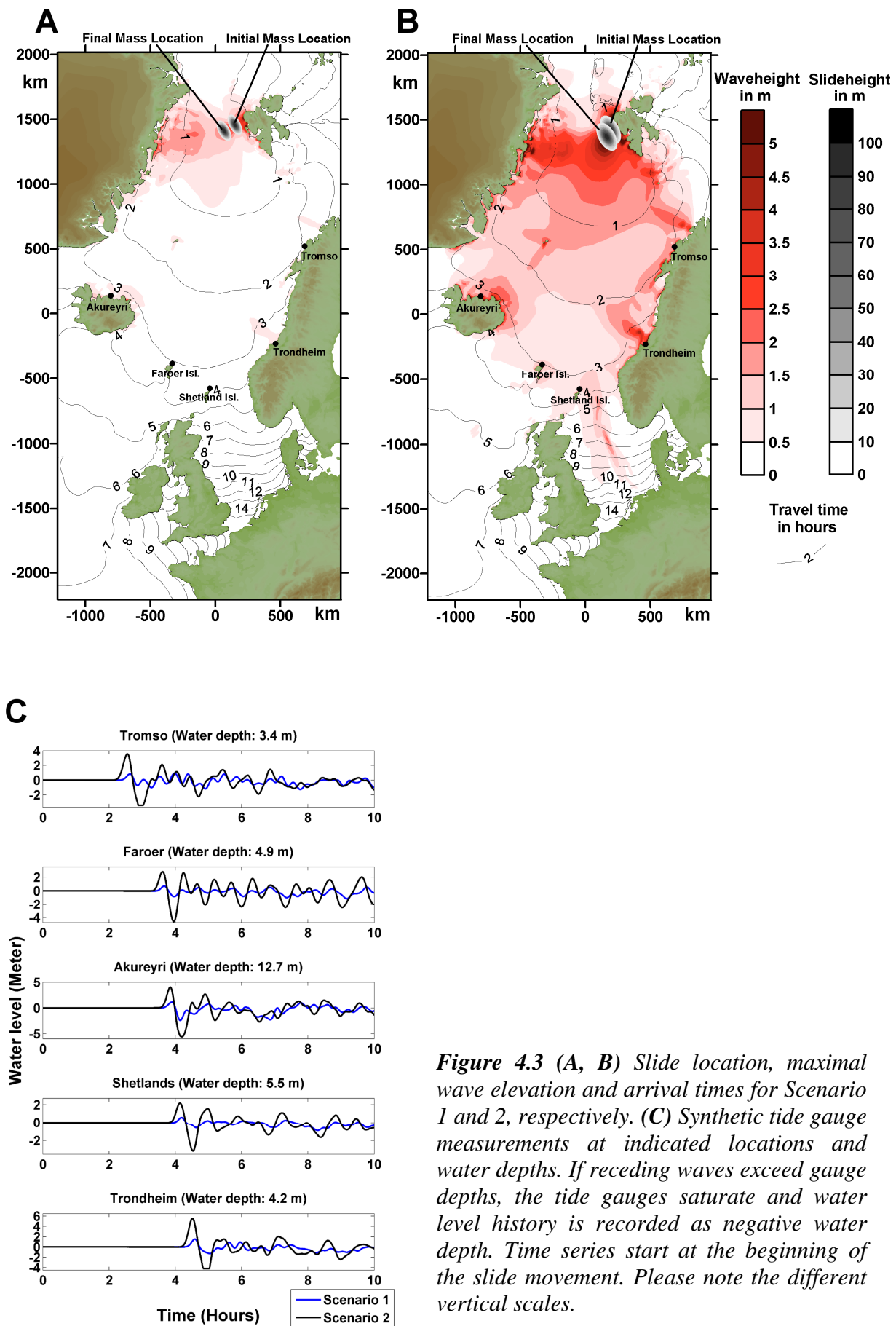
Figure 4.3 (A, B) Slide location, maximal wave elevation and arrival times for Scenario 1 and 2, respectively. (C) Synthetic tide gauge measurements at indicated locations and water depths. If receding waves exceed gauge depths, the tide gauges saturate and water level history is recorded as negative water depth. Time series start at the beginning of the slide movement. Please note the different vertical scales.

Scen-ario	Tromsø (Depth 3.4 m)	Faroer (Depth 4.9 m)	Akureyri (Depth 12.7 m)	Shetlands (Depth 5.5 m)	Trondheim (Depth 4.2 m)
1	0.9 m	0.7 m	1.1 m	0.6 m	1.5 m
2	3.6 m	2.8 m	4.0 m	2.2 m	5.6 m
3	1.7 m	1.2 m	1.8 m	1.0 m	2.8 m
4	1.7 m	1.3 m	2.4 m	1.0 m	2.6 m

Table 4.2 Maximal wave heights. Water depths of virtual gauges are indicated below the place names.

The size of this slide is based on the extent of contourite deposits on the slope as imaged by new bathymetric data (Bünz et al. 2008). It involves an area of 130 km width and 70 km length and moves in southwesterly direction. The landslide of Scenario 2 mobilizes 1000 km³ of sediments, which is still less than half of the Storegga slide's volume (Haflidason et al. 2004). The maximal slide height is assumed again to be 100 m which is close to the Storegga slide's 120 m (Kvalstad et al. 2005) and significantly less than the Hinlopen Slide's 1400 m (Vanneste et al. 2006). The mass movement stops at a distance of 60 km down-slope. In both scenarios, the maximal velocity is assumed to be 35 m/s. This celerity is based on the modeling results for Storegga (Løvholt et al. 2005), which we assume to be a good analogue for the sediment properties off Svalbard. The shape of the slide will also have an effect on the resultant tsunami (Ward et al. 2001), but as there are no further constraints on this we assume oval shaped slides which will result in average tsunami parameters.

Exact parameters of an event are hard to predict. So, Scenario 3 and 4 include variations of the important parameters volume, celerity and initial acceleration. Scenario 3 is similar to Scenario 2, the difference lies in the maximal slide speed and the initial acceleration. Scenario 4 uses the location and dynamical properties of Scenario 1, while moving twice as much sediment volume. The parameters for each scenario are listed in Table 4.1.

4.2.2 Modeling results

The maximum wave height distributions of each scenario are presented together with the slide form in Figure 4.3A, 4.3B, 4.4A and 4.5A. While the wave heights of Scenario 1 are small, Scenario 2 generates a large tsunami. Tsunami heights are calculated for cities on the Norwegian coast, the Faroe and Shetland Islands, and Iceland. In this context it must be noted that actual run-up depends strongly on local topography (Hornbach et al. 2008), especially in fjords and can be significantly smaller or larger than the computed maximal wave heights. Mareograms for selected locations are depicted in Figure 4.3C. The results show waves of nearly 6 m. Although the Norwegian Sea coasts are rocky and population densities are low, it is clear that a tsunami of this size would cause significant damage to communities in Norway, Iceland and Eastern Greenland.
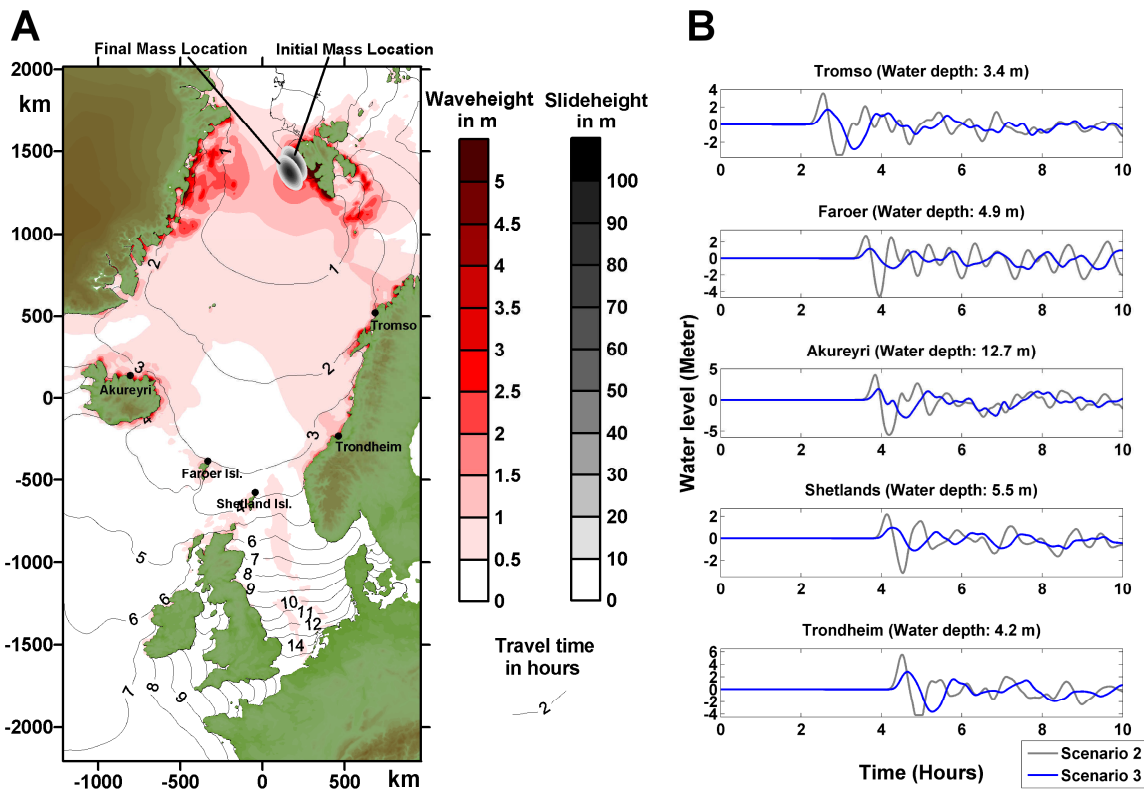
Figure 4.4 (A) Slide location, maximal wave elevation and arrival times for Scenario 3. (B) Mareogram comparison between Scenario 2 (35 m/s maximal velocity) and 3 (20 m/s). Please note the different vertical scales.
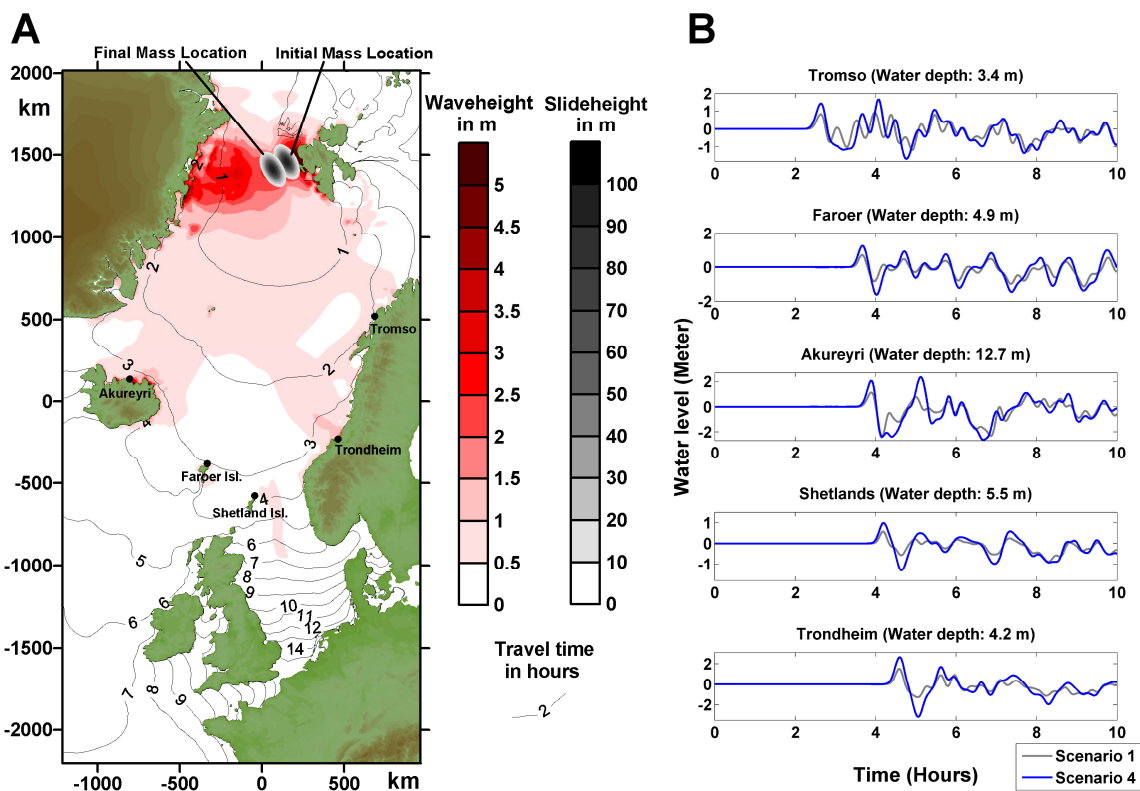

Figure 4.5 (A) Scenario 4 slide location, maximal wave elevation and arrival times. (B) Mareogram comparison between Scenario 1 (500 km³ volume) and Scenario 4 (1000 km³), where all other parameters are identical. Please note the different vertical scales.

The comparison of Scenario 2 and 3 (Figure 4.4B) shows the influence of the slide speed. By decreasing the maximum slide velocity from 35 m/s to 20 m/s, wave heights lower by a factor of more than two (Table 4.2). This nonlinear dependence can be explained by describing the build-up phase of the wave. If the slide moves much slower than the water waves, the slide-induced uplift of the water surface levels quickly. For fast slides, the uplift of each time step superposes onto the wave, increasing its height significantly. Therefore, the ratio of wave velocity to slide speed, termed Froude number, can be regarded as a measure for the effectiveness in tsunami excitation of a slide (Table 4.1 and Ward et al. (2001)). The control of slide volume on a tsunami can be seen by comparing Scenario 1 and 4 (Figure 4.5B, Table 4.2). An increase of the volume by a factor of two doubles the resultant maximum wave heights, indicating a linear dependency within this parameter range.

The slide direction strongly influences the wave radiation pattern. The Scenarios 1 and 4 with a westward slide direction radiate a significant part of the energy towards Greenland, leaving northwest Europe with relatively small wave amplitudes. A slide moving towards Southwest (Scenarios 2 and 3), however, releases the leading wave energy directly into the Norwegian and Greenland Sea. Although the basin topography has a defocusing effect on the tsunami, wave heights in northwest Europe double compared to the slides in westward direction. Unfortunately, the general southwesterly dip direction of the Svalbard margin between Prins Karl Forlandet and Vestnesa make a southwesterly direction for the slide more likely than a westward direction.
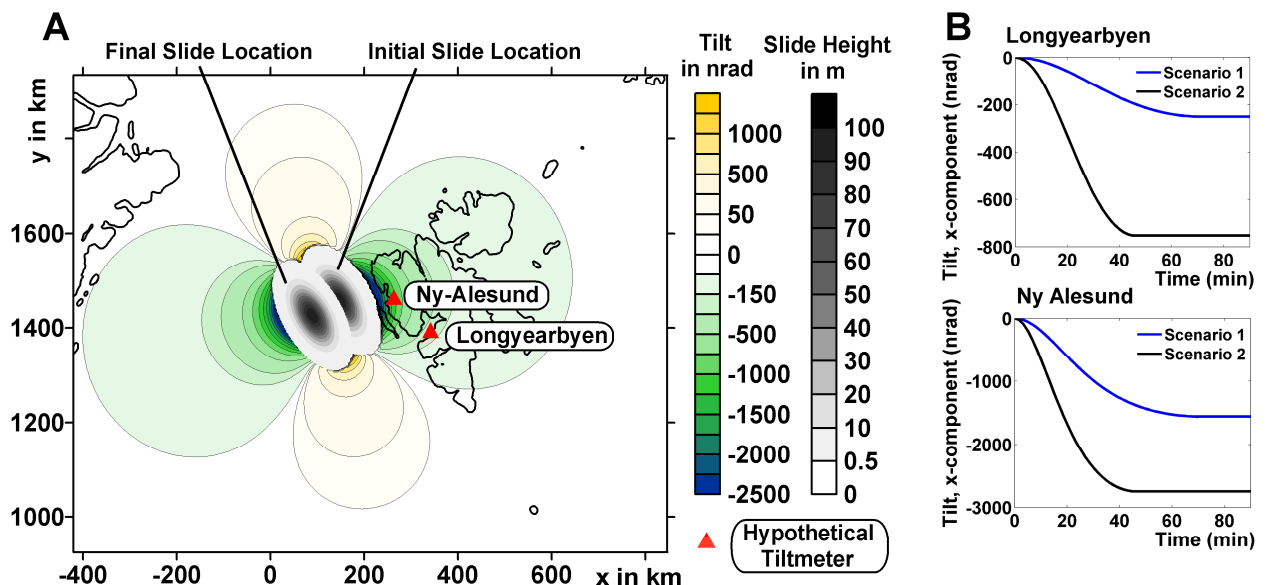

Figure 4.6 (A) *Surface tilting in x-direction for landslide of Scenario 1.* (B) *X-component of theoretical tiltmeter measurements. Scenario 1 and 2 are clearly distinguishable. Please note the different vertical scales.*

49

4.3 Implications for a tsunami warning system

With respect to the impact on coastal communities, a tsunami warning facility would be worthwhile. Unfortunately, predicted surface displacements (around 10 cm, maximum) can be only marginally detected by real-time GPS observations. Thus, the otherwise very efficient tsunami warning technique based on near-field GPS observations (Sobolev et al. 2007) is not suitable in this case. We propose a new tool for Landslide Tsunami Early Warning. The method is based on the fact that a mass displacement of $\sim 10^{15}$ kg will lead to a notable surface deformation. Following the assumption of the elastic half-space, we estimate the amount of surface tilting using an analytical solution (Melchior 1966; Boussinesq 1878):

$$\alpha_{1,2} = \frac{\partial u_3}{\partial x_{1,2}}$$

$$u_3 = -\left[\frac{1-\nu}{2\pi G} + \frac{f}{g^2}\right]\Phi$$

$$\Phi = \iint \frac{P(\varsigma_1,\varsigma_2)}{R(x_1,x_2,0,\varsigma_1,\varsigma_2)} d\varsigma_1 d\varsigma_2$$

$$R(x_1,x_2,0,\varsigma_1,\varsigma_2) = \left[(x_1-\varsigma_1)^2 + (x_2-\varsigma_2)^2\right]^{1/2}$$

These formulas allow to calculate the tilt signal in x- and y-direction ($\alpha_{1,2}$) due to a load distribution (P). We apply it to the initial and the final sediment distribution. The measurable change in surface tilt during the landslide is computed as the difference between final and initial tilt signal. Further involved variables and parameter are: u_3 - Vertical displacement (z-axis directed upwards), $x_{1,2}$ - Point of observation, $\zeta_{1,2}$ - Point of load, R - Distance, f - Gravitational constant ($6.67 \cdot 10^{-11}$ Nm^{2}kg^{-2}), g - Standard gravity (9.81 ms^{-2}), ν - Poisson ratio (0.25), G - shear modulus ($7 \cdot 10^{10}$ Pa).

As the deformation due to the slide involves large lithospheric portions, the involved parameters of the elastic half-space are evaluated at lithospheric depths: The Poisson ratio of 0.25 is a lithospheric average and the value of the shear modulus is estimated at a depth of 100 km which corresponds to the distance between tiltmeter and load. We implement biaxial tiltmeters. One leg measures tilts in positive x-direction (East), the other in positive y-direction (North).

The overall tilt distribution for the x-component is depicted in Figure 4.6A. Tilt measurements of hypothetical inclinometers positioned at Longyearbyen and Ny-Ålesund are shown in Figure 4.6B. Occurring tilt amplitudes of the order of 1000 nrad are extremely well within the accuracy range of several nanorad for today's tiltmeters (D'Oreye and Zürn, 2005; Gebauer et al. 2007).
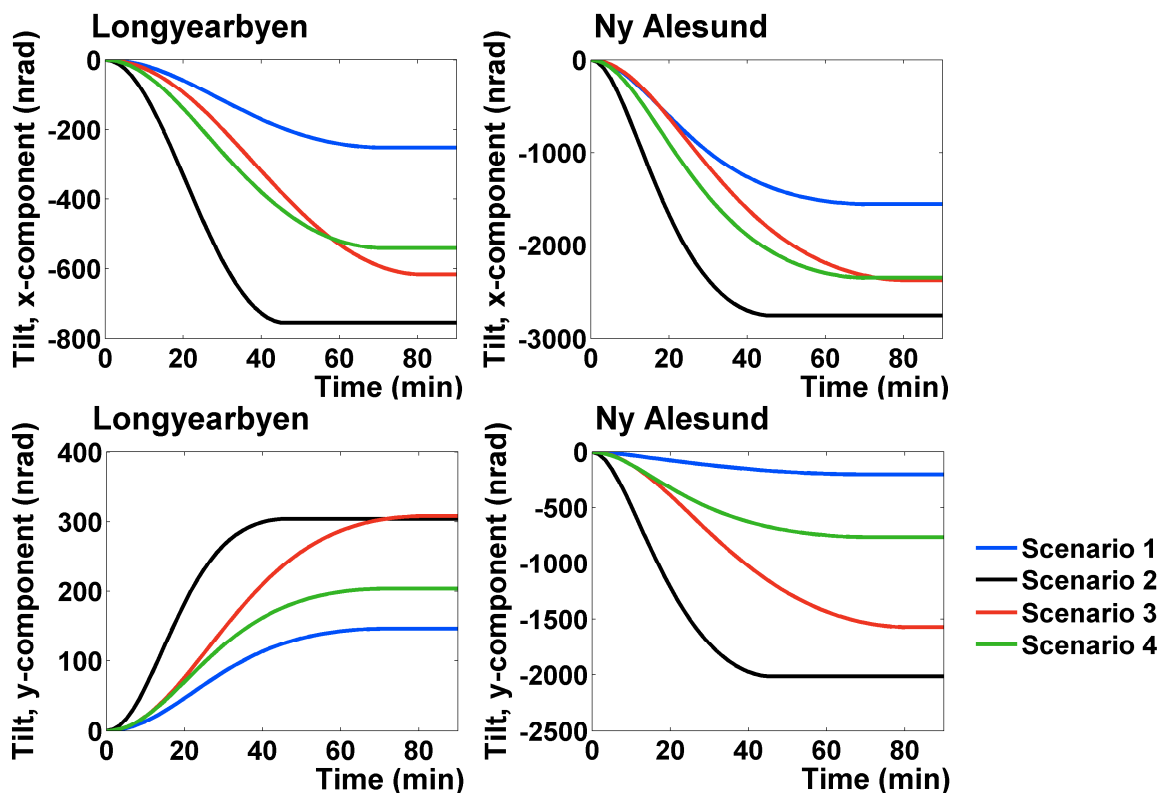
Figure 4.7 Hypothetical tiltmeter measurements. Shown are x-and y-components of each scenario. Please note the different scales.

For each of the four scenarios, Figure 4.7 depicts the components of the computed tilt vector in x- and y-direction. The time series of the x-components for Scenario 3 and 4 are very similar, however, they can be distinctly discriminated via the y-component. Out of these possible events, the most hazardous Scenario 2 can be clearly recognized.

By implementing inclinometers at Spitsbergen, a large submarine mass movement can be reliably detected a few minutes after slide initiation. We envisage a setup in which the tiltmeter response and the range of likely tsunamis is modeled for several realistic landslide scenarios before installation of the tiltmeters. In this case tsunami-relevant parameters like displaced mass, travel distance and velocity will be accessible as soon as the bulk of the mass has moved, i.e. approximately after one hour. Obviously slow precursors or run-out of turbidites may occur over a longer time span, but as the tsunami is linked to the main acceleration of the bulk of the landslide only this information is necessary for the tsunami warning system (Figure 4.6B).

4.4 Conclusions
From modeling different tsunami scenarios we conclude that a landslide in the Fram Strait has the potential to create a tsunami that would affect northwest Europe. Present global warming increases the probability for such an event. We calculate the effect that such a slope failure would have on tiltmeters. We conclude

that the installation of these instruments on the west coast off Svalbard would constitute an efficient warning tool that gives several hours of advance warning before a tsunami would strike the coasts of Norway, Iceland, the Faroe and Shettland Islands.

Chapter 5

Towards early warning for tsunamis, generated by large submarine landslides

Sascha Brune, Andrey Y. Babeyko, Stephan V. Sobolev

Helmholtz Centre Potsdam GFZ German Research Centre for Geosciences, Potsdam, Telegrafenberg, 14473 Potsdam, Germany

Abstract

Large submarine landslides can generate dangerous tsunamis. Due to their long period signal, the detection of landslides by common seismological methods is difficult. Here, we present a method of detecting submarine landslides by using an array of tiltmeters. The displacement of a large volume of sediment during landsliding produces a detectable elastic response of the lithosphere. We propose a technique to calculate this response and to invert for tsunami relevant parameters like slide location, volume and velocity. We exemplify our method by applying it to the historical Storegga slide west of Norway and other tsunamigenic landslide events. The amplitude of the generated tsunami wave is controlled by the product of slide volume and its velocity (slide tsunamigenic potential), the parameter which can be most robustly estimated from tiltmeter array measurements. The accuracy of the inversion of this parameter and the estimated tsunami height near the coast depends on the noise level of tiltmeter measurements, distance of the tiltmeters from the slide, and slide tsunamigenic potential. The tsunamigenic potential of the most dangerous slides like Storegga can be estimated well by tiltmeters at the coast if the measurement noise level does not exceed 50 nrad.

5.1 Introduction

Most tsunamis are generated by underwater earthquakes. But although submarine earthquakes in areas like the North Atlantic including the Norwegian Sea are small, the tsunami hazard can not be neglected. Some of the worlds largest submarine

landslides have been identified in this region: the Storegga slide at the Norwegian continental slope (8200 years BP), the Hinlopen slide north of Spitsbergen (probably pre-Holocene) and the Trænadjupet slide off Norway (4000 years BP) involving volumes of 2400 km³ (Bondevik et al. 2005), 1350 km³ (Vanneste et al. 2006) and 500 km³ (Laberg et al. 2002), respectively. The Storegga slide has been extensively studied (Bugge et al. 1987; Solheim et al. 2005a), due to Norwegian oil-recovery interests in the head scarp area. Tsunami deposits of the Storegga event have been found in lake sediments of Norway, the Faroe Islands and on Scottish coasts. Run-up was reported as 10 m in Norway and even 20 m on the Shetland Islands (Bondevik et al. 2005). While these huge landslides occurred in the North Atlantic, there are numerous examples of tsunamigenic landslides in other parts of the world (Yalçiner et al. 2003; Papadopoulos et al. 2007a; Tinti et al. 2004; Okal et al. 2003, McAdoo et al. 2000). Especially large events of the 20th century were the 1929 Grand Banks slide off Canada and the 1998 Aitape slump off Papua New Guinea. During these events sediment volumes of 200 km³ and 4 km³, respectively, failed (Fine et al. 2005; Sweet and Sliver 2003). Also, as discussed in this thesis (Chapter 4), a large slide west of Spitsbergen is possible.

While source parameters of tsunamigenic earthquakes can be determined in real-time with reasonable accuracy by classical seismological (Lomax et al. 2007) or novel GPS techniques (Sobolev et al. 2007), it is still very difficult to detect submarine landslides in the course of the event. Broadband seismic stations are not effective due to the comparatively small release of seismic energy and the long period signal. Although T waves of landslides can be identified in hydroacoustic and seismic records in the aftermath (Okal 2003), this technique is not yet applicable in real-time. GPS-buoys or ocean bottom pressure sensors are able to measure a tsunami during its passage, but to quantify wave height and wave length, the arrival of the wave crest has to be waited for. If endangered coastal locations are close to the tsunami source, this loss of time is not acceptable. An effective local tsunami early warning system requires the derivation of source parameters already during the tsunami excitation. In the present paper, we propose a method to assess location, volume and velocity of submarine landslides in real-time. We illustrate our method by applying it to the Storegga event and discuss its accuracy with respect to tsunami early warning.

5.2 Mathematical models
5.2.1 Tilting and Storegga slide models
A mass displacement produces an elastic deformation of the nearby lithosphere. Viscous effects are negligible, if the relevant time scale is much smaller than the Maxwell relaxation time which is in the order of 100 years for crust and upper mantle. Thus, with landslides lasting minutes to hours, elasticity clearly dominates. We calculate tilt responses within the elastic half space approximation (Melchior 1966, Boussinesq 1878):

$$\alpha_{1,2} = \frac{\partial u_3}{\partial x_{1,2}}$$

$$u_3 = -\left[\frac{1-\nu}{2\pi G} + \frac{f}{g^2}\right]\Phi$$

$$\Phi = \iint \frac{P(\varsigma_1,\varsigma_2)}{R(x_1,x_2,\varsigma_1,\varsigma_2)} d\varsigma_1 d\varsigma_2$$

$$R(x_1,x_2,\varsigma_1,\varsigma_2) = \left[(x_1-\varsigma_1)^2 + (x_2-\varsigma_2)^2\right]^{1/2}$$

The involved variables and parameter are: $\alpha_{1,2}$ - tilt in x- and y-direction, u_3 - vertical displacement (z-axis directed upwards), $x_{1,2}$ - point of observation, $\zeta_{1,2}$ - point of load, P - load distribution function, R - distance between $x_{1,2}$ and $\zeta_{1,2}$, ν - Poisson's ratio (here: 0.25, lithospheric average), f - gravitational constant ($6.67 \cdot 10^{-11}$ Nm^2kg^{-2}), g - standard gravity (9.81 ms^{-2}), G - shear modulus (here: $7 \cdot 10^{10}$ Pa, corresponding to 100 km depth).

The measured surface inclination will be the result of two superposing effects, the removal of sediment and its deposit. Both are calculated with above formulas, whereas the removal contributes with a negative sign. The distance between the slide center of mass at the start and at the end of the movement, will be further on referred to as travel distance. This parameter has a crucial influence on the deformation. For small travel distances, like for slumps, removal and deposition areas overlap. Hence, only a small resulting inclination of the free surface takes place. Assuming a constant sediment density, the load pressure distribution P is directly proportional to the slide shape. In this paper we focus on landslide detection and not on detailed modeling of morphological features. So we use a simple non-deformable slide shape parameterized by its height, length, width and orientation angle. Cross sections of the slide body consist of smooth polynomials, whose values and derivatives are zero at the edges. The full width at half maximum value corresponds exactly to a half of the overall length.

We exemplify this method by applying it to the Storegga event. In accordance with published bathymetry data and previous Storegga slide models, especially of Løvholt et al. (2005), the modeled slide body has a volume of 2400 km³ with a slide height of 220 m, length of 260 km and width of 180 km (Bryn et al. 2005; Bondevik et al. 2005). The center of mass moves from 4° 8' E, 63° 45' N to 2° 3' E, 64° 45' N. Figure 5.1 depicts the movement in stereographically projected coordinates. The velocity profile is symmetrically composed out of sinusoidal segments. The sliding starts with an acceleration of 0.016 m/s², reaches a maximal velocity of 35 m/s and travels 150 km. These parameters have been calibrated against measured run-up heights of the Storegga slide (Løvholt et al. 2005).
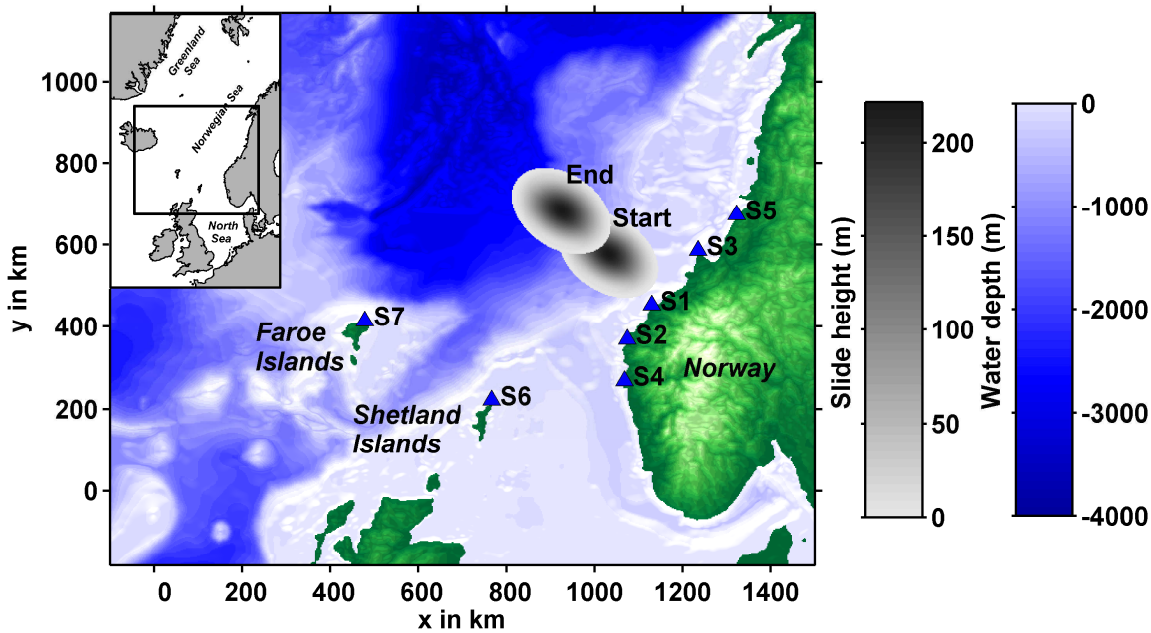
Figure 5.1 *Storegga slide model. Sediment distributions at the beginning and the end of the event are shown in gray. Blue triangles depict locations of virtual tiltmeter stations S1 to S7.*

5.2.2 Inversion technique

In the previous section, we proposed a model that computes tilt signals for a given landslide event. To invert observed tilt signals into landslide parameters, we use this forward model together with the Matlab nonlinear minimization routine fminsearch (Matlab Version 7.1; Lagarias et al. 1998) and minimize the root mean square of the difference between calculated and input tilt. To get a more stable inversion, we assume a rotationally symmetric slide shape parameterized by one variable only - the volume. The shape consists of smooth polynomials and is scaled self-similarly to match the given volume. The width to height ratio is 1500, so a 2400 km³ slide is 250 km wide and long, as well as 165 m high. Other inversion variables are initial slide position as well as the time-dependent displacement history of the slide.

5.2.3 Tsunami propagation model

We model tsunami propagation with the nonlinear Boussinesq code COULWAVE, using two vertical layers (Lynett and Liu 2002). The applicability condition (ratio of slide length to submergence depth must be larger than 7) is fulfilled due to a corresponding value of roughly 70. We project the sea bottom change, due to the mass movement, directly towards the sea surface. So the propagating slide dynamically builds up the surface wave. The tsunami is calculated on a 900×750 grid with a spatial step size of 2500 m and a time step of 3 s. Flow depths are estimated based on Green's law extrapolation from 10-20 m depth to 1 m depth. We use the flow depth values to compare the tsunami impact of different scenarios. They should not be mistaken for run-up heights whose computation requires modeling on a refined grid and detailed knowledge on topography.
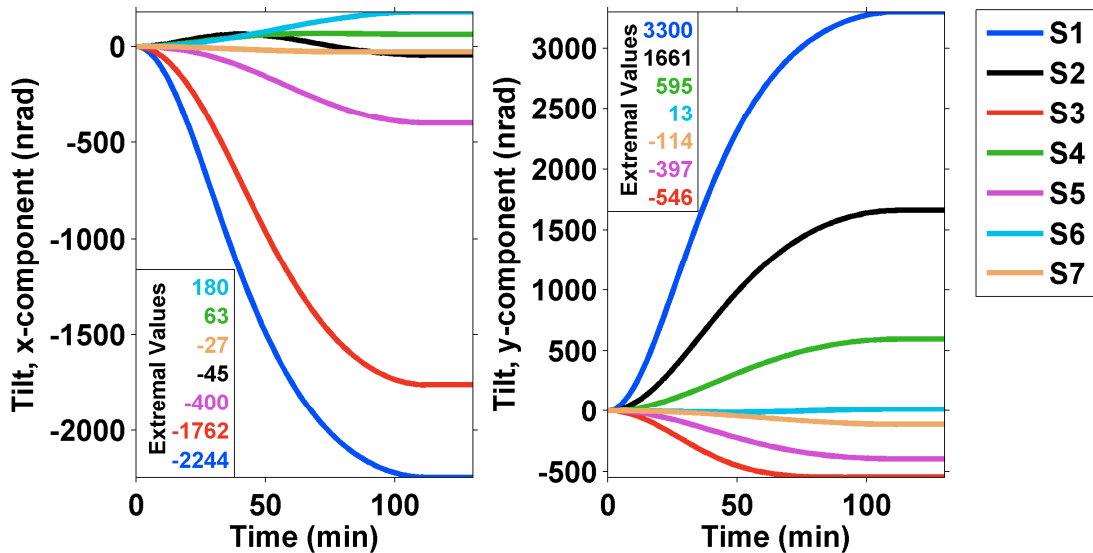
Figure 5.2 *Computed tilt signals in x- and y-direction of the Storegga event. Positions of tilt stations S1 to S7 are mapped in Figure 5.1.*

5.3 Landslide remote sensing via tiltmeters

5.3.1 Landslide real-time detection

Figure 5.2 shows calculated tilt signals of our Storegga slide model. Virtual stations S1 to S5 are located in Norway, S6 on the Shetland Islands and S7 on the Faroes. All stations consist of two-axis tiltmeters which are oriented towards east and north for x- and y-direction, respectively. Station S1, which is nearest to the slide, exhibits maximum tilt values of approximately -2000 nrad for the x-component and 3000 nrad in y-direction. Regarding a present day tiltmeter accuracy of several nanorad (D'Oreye and Zürn 2005; Gebauer et al. 2007), a huge landslide of the Storegga-scale will be clearly detectable. The surface deformation due to the landslide reaches the station nearly instantaneously enabling the real-time detection of the event.

5.3.2 Inversion for tsunami relevant parameters

As noted in section 5.2.2, we want to invert observed tilt signals into tsunami-relevant slide parameters such as initial position, volume and time-dependent displacement history. The modern tiltmeter precision of several nanorad allows not only for landslide detection, but also for recording of tides, heavy rain and other events. These processes superpose to landslide signals and thus degrade the quality of inversion. The latter will depend on the ability to exclude the secondary effects from tilt records. Advanced models can be used to correct for solid earth tides (McCarthy and Petit 2004). Furthermore, characteristic times of landslides movement range between several minutes for small events up to about one hour in case of huge slides. Filtering for the corresponding frequency range will exclude noise signals of different time periods.
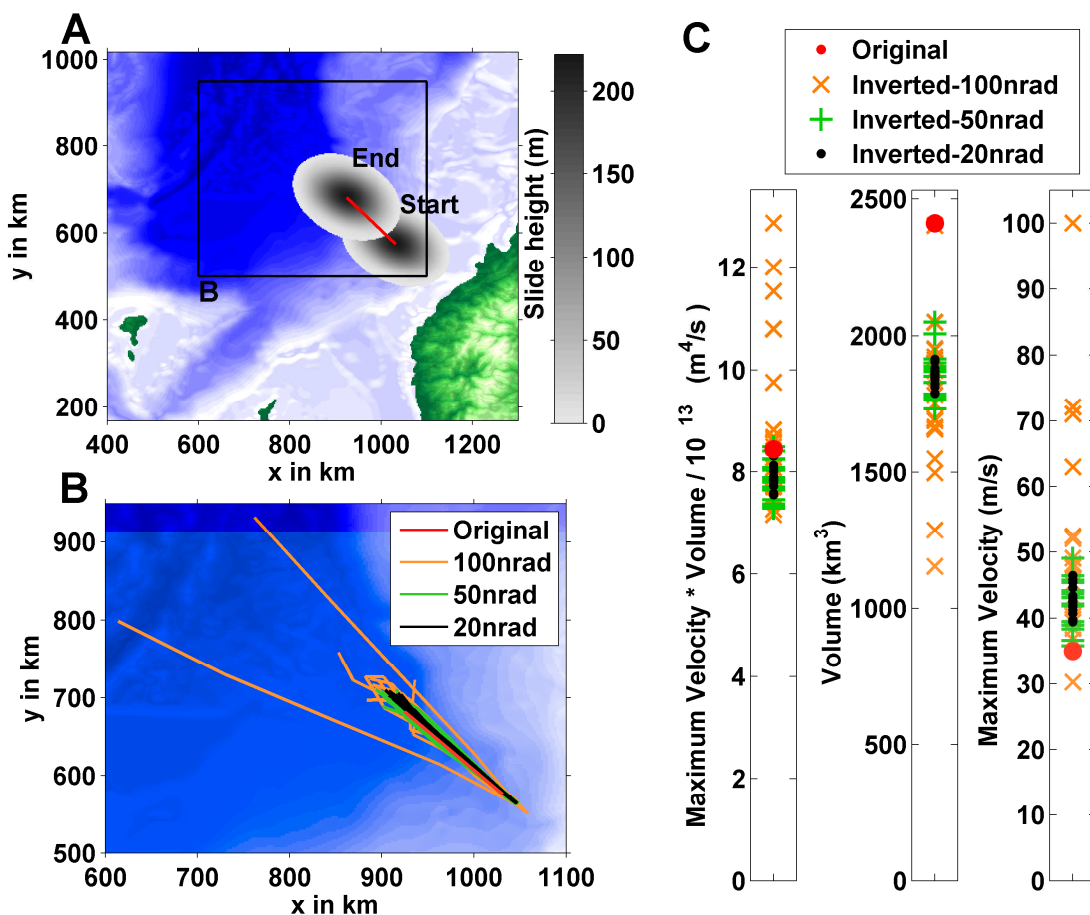
Figure 5.3 Storegga slide inversion: Influence of noise level *(A)* Storegga slide model setup. The red line indicates the center of mass trajectory. *(B)* Original (see A) and inverted center of mass trajectories for noise amplitudes of 20, 50 and 100 nrad. *(C)* Inverted and original values for the tsunami-relevant product of volume and maximum velocity and both of them alone.

Despite these correction routines, a certain amount of "effective" noise will remain within the data. We investigate how this residual perturbance affects the inversion by adding white noise to the synthetic tilt data of our model before inverting. We examine three noise amplitudes: 20, 50 and 100 nrad, and invert 20 different data samples for each noise level. Inversion results together with the original model are shown in Figure 5.3B. We find good inversion results for the noise levels of 20 and 50 nrad, and rather poor results for 100 nrad.

The product of maximum velocity and volume is a measure for the slide tsunamigenic potential (Løvholt et al. 2005). As depicted in Figure 5.3C, this parameter deviates not more than 10 % from the original value in cases of 20 and 50 nrad. A noise amplitude of 100 nrad again does not yield satisfying correspondence. Interestingly, volume and maximum velocity are under- and overestimated, respectively. This discrepancy results from different geometries of the original scenario (elongated source) and the rotationally symmetrical forward model of the inversion. Tsunami predictions based on the inversion results are discussed in section 5.4.
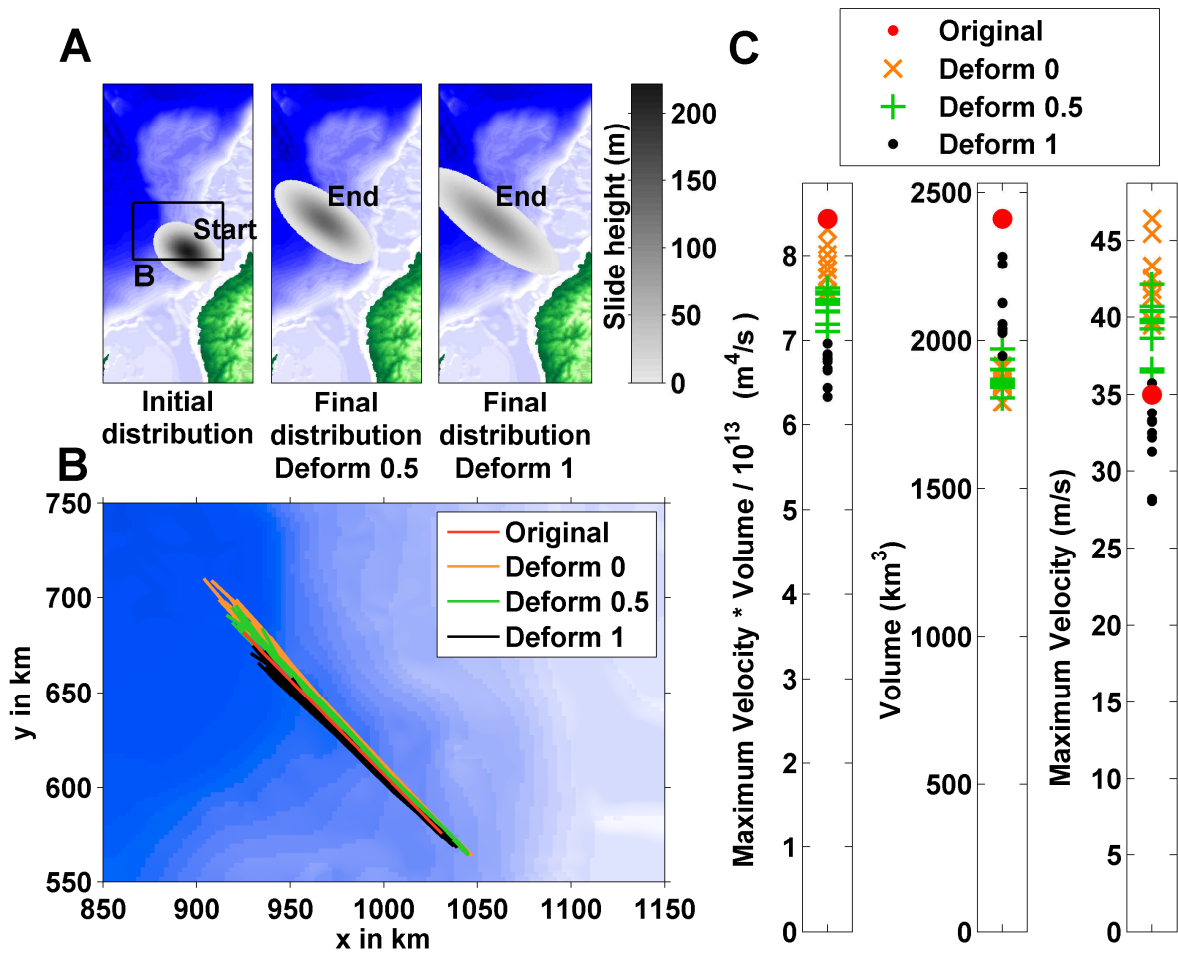
Figure 5.4 Influence of slide deformation on inversion results (Noise level: 20 nrad). (A) Slide models with identical volumes, but different deformation factor (see section 5.3.2): Deform= 0, 0.5, 1. Thereby Deform=0 corresponds to the original Storegga discussed before. (B) Inverted and original center of mass trajectories. (C) Product of volume and maximum velocity (tsunamigenic potential) and each of them alone.

Large submarine slide bodies tend to disintegrate during the landslide event (Haflidason et al. 2005). Effectively, the disintegration leads to a dynamic decrease of slide height and an increase of slide length (the slide dimension parallel to the slope). To test the possible effect of the slide disintegration, we model the slide deformation during the movement by enlarging the length of our Storegga slide body while simultaneously adjusting its thickness to conserve the volume. Dynamic slide deformation is described by the following law:

$$l(t) = l(0) + 2 \cdot \textbf{\textit{Deform}} \cdot s(t)$$

where *l(t)* is time-dependent slide length, *h(t)* slide width, *s(t)* travel distance and *Deform* is a non-dimensional parameter varying between 0 and 1. *Deform* = 0 conserves the slide length, while *Deform* = 1 produces maximum deformation. For values larger than 1, the upper slide end would propagate up-slope which is unphysical. In case of the Storegga slide with 150 km travel distance, maximal deformation (*Deform* = 1) corresponds to a slide length increase from 260 km to 560 km while the height decreases from 220 m to 100 m.
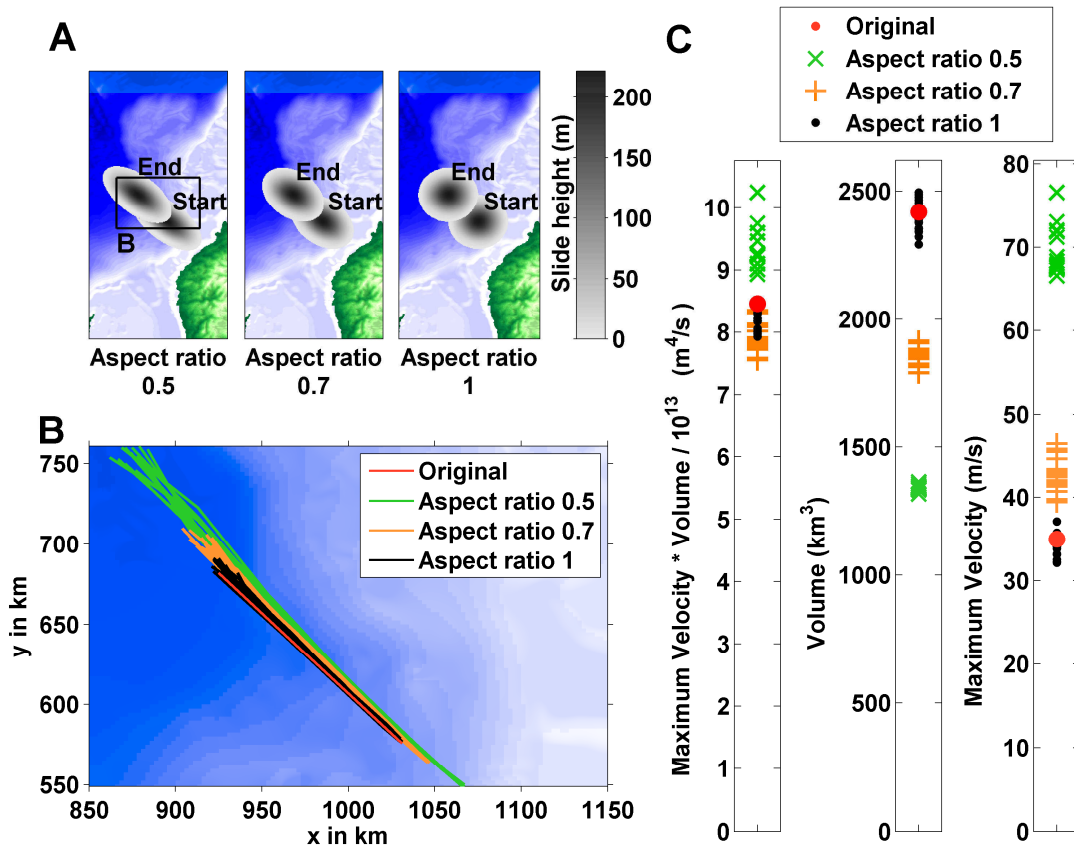
59

Figure 5.5 *Influence of slide geometry on inversion results (Noise level: 20 nrad). **(A)** Slide models with identical volumes, but different aspect ratios: 0.5, 0.7 (as described in section 5.2.1) and 1. **(B)** Inverted and original center of mass trajectories. **(C)** Product of volume and maximum velocity (tsunamigenic potential) and each of them alone.*

Figure 5.4 shows the influence of the slide deformation on our inversion results. We compare inversion results for three equal-volume but different shaped models (*Deform* = 0, 0.5 and 1). Generally, inversion results demonstrate low sensitivity to the slide deformation. Inverted trajectories (Figure 5.4B) as well as maximum velocities and volumes (Figure 5.4C) differ only slightly. The influence on the tsunamigenic potential is also rather small: the product of volume and maximum velocity decreases by 10 % for *Deform*=0.5 and ~20 % for *Deform*=1.

Finally, we address the question of reliability of our inversion for different slide geometries. Since it seems hardly problematic to derive the exact shape of a landslide in real-time, we invert tilt observations using a rotationally symmetric slide body as described in section 5.2.2. Moreover, this constraint gives us more stable inversion results. To check reliability and robustness of this assumption, we apply our inversion procedure to slide bodies with aspect ratios of 0.5, 0.7 and 1 while keeping the volume and height constant (Figure 5.5). Large slides like Storegga (aspect ratio 0.7, see section 5.2.1) tend to be elongated in direction parallel to the slide movement, so we focused on this direction of elongation. As expected, our inversion yields best results for the forward model with aspect
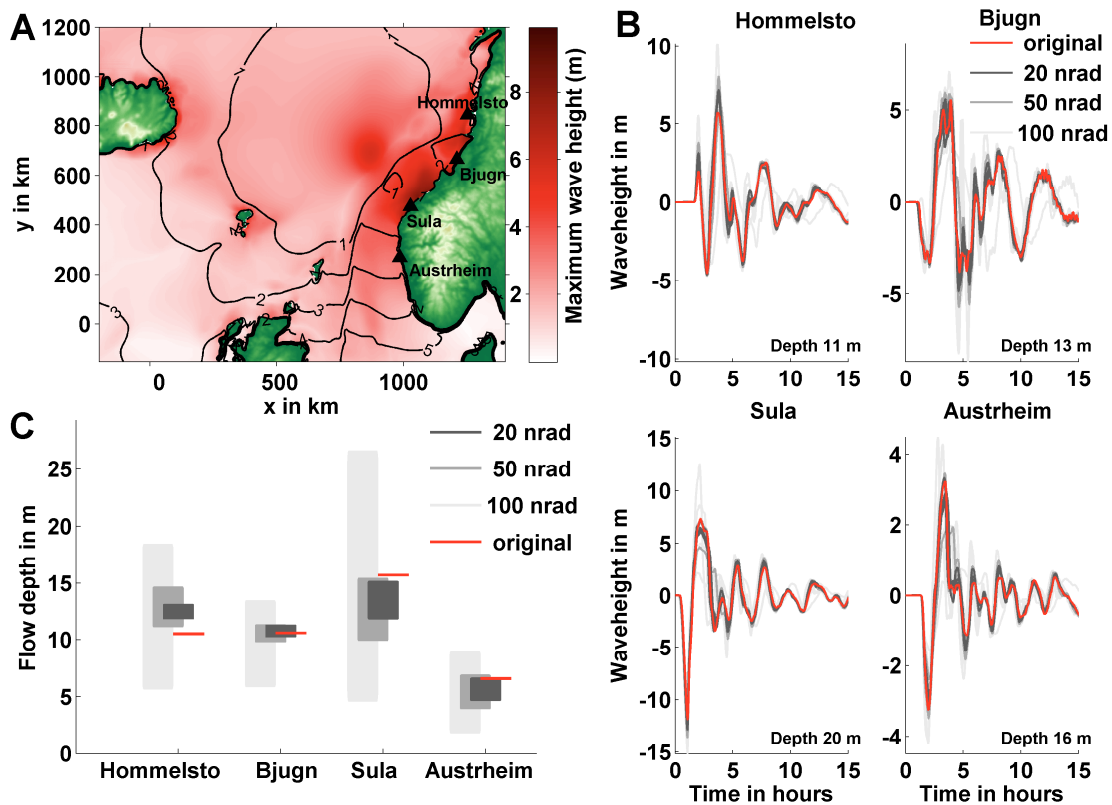
Figure 5.6 *Tsunami prediction based on inversion results. (A) Maximum tsunami wave heights and arrival times of the original scenario. Positions of virtual tide gauges are marked by black triangles. (B) Virtual mareograms of original and inverted tsunami scenarios. (C) Scattering range of flow depths for original and inverted data. Flow depths are evaluated at one meter water depth by extrapolation with Green's Law.*

ratio 1, which corresponds to the rotationally symmetric slide body of the inversion procedure. The discrepancies of location, volume and maximal velocity grow up to 50 % for strong elongated slides. However, the tsunamigenic potential of the event, which is the product of volume and maximum velocity, was estimated within 20 % of the original value. Thus, we can conclude that the tsunamigenic potential of a landslide of any shape can be predicted rather reliable and robustly even if the original geometry strongly differs from rotationally symmetrical.

5.4 Tsunami prediction
The previous section shows that despite some under- and overestimation of particular slide parameters, the inversion procedure, nevertheless, yields good results for the tsunamigenic potential of a landslide. To further illustrate this idea, we directly compare resulting tsunami impact from the original Storegga model with that of inverted models with 20, 50 and 100 nrad noise (compare Figure 5.3). The maximum wave height of the tsunami for the original scenario is shown in Figure 5.6A. Near-shore maximum wave heights reach up to 7 m in Norway. Arrival times are 1.5 to 4 h at the Norwegian coast, about 1 h at the Shetland and Faroe islands, 2 h for Iceland and 3 to 5 hours for the Scottish mainland.
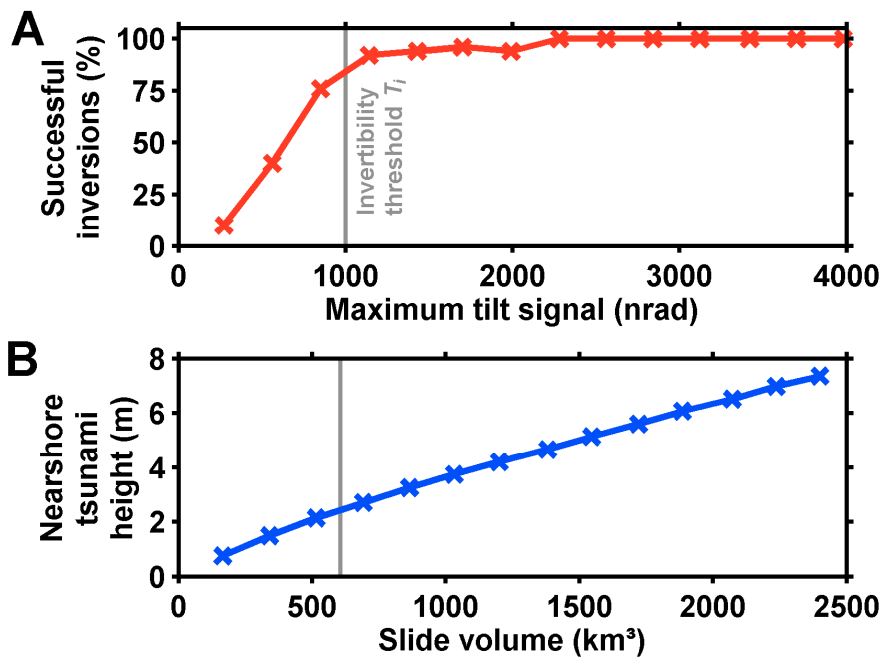
Figure 5.7 *Defining the invertibility threshold for Storegga-like scenarios of volumes between 165 km³ and 2400 km³ (original Storegga size). (A) Percentage of successful inversions (white noise amplitude: 20 nrad) and invertibility threshold. (B) Invertible scenarios exceed 600 km³ and exhibit wave heights larger than 2.5 m.*

To check inversions against the original model, we perform tsunami calculations based on the inverted slide parameters of each considered noise level (20, 50 and 100 nrad). Therefore, five representative scenarios (including end members) where chosen among the 20 inversion results of each noise level (see section 5.3.2). Outliers for noise of 100 nrad which show unreasonably high velocities of 100 m/s were excluded from the tsunami simulations. Mareograms of the considered scenarios are compared to the original scenario in Figure 5.6B. Arrival times and wave forms correspond very well, while the amplitude increases with noise from about 10 % for 20 and 50 nrad, to 40 % for 100 nrad. The corresponding ranges of flow depth values, calculated with Green's law for every noise level, are displayed as gray bars in Figure 5.6C. The flow depth of the original scenario, for comparison, is shown in red. Again, we find satisfying correspondence between original scenario and 20 nrad as well as 50 nrad noise data.

5.5 Estimating the applicability scope

The Storegga event was exceptionally large. In this section, we study the applicability of our method to mass movements with smaller slide volumes. Therefore, we first define two distinct qualities: (a) We call an event detectable if the slope failure generates a tilt signal that is larger than the detectability threshold T_d. (b) We assume the existence of an invertibility threshold T_i, that has to be exceeded by a tilt amplitude, in order to ensure the invertibility for correct location and tsunamigenic potential. In principle, both T_d and T_i depend on the concrete

Event (year)	Volume (km³)	Travel distance (km)	Distance to coast (km)	References
Aitape, Papua New Guinea (1998)	4	0.84	30	(Sweet and Silver 2003)
Nice, France (1979)	0.15	5	5	(Assier-Rzadkiewicz et al. 2000)
Unimak, Alaska, USA (1946)	120	179	80	(Watts 2003)
Grand Banks, Canada (1929)	200	200	280	(Fine et al. 2005)
Oshima-Oshima, Japan (1741)	2.5	10	5	(Satake and Kato, 2001)
Hinlopen, Norway (4000 BP)	1350	100	100	(Vanneste et al. 2006; Winkelmann et al. 2006)
Palos Verdes, California, USA (7500 BP)	0.73	5	6	(Locat et al. 2004; Normark et al. 2004)
Storegga, Norway (8200 BP)	2400	150	100	(Haflidason et al. 2005)
Alika, Hawaii, USA (100 000 BP)	400	100	100	(McMurtry et al. 2004)
Sumba, Indonesia (unknown)	95	10	135	(This thesis, chapter 2)
Albemarle-Currituck, Virginia, USA (unknown)	150	100	100	(Driscoll et al. 2000)
Spitsbergen, Norway (possible)	1000	60	80	(This thesis, chapter 4)

Table 5.1 *Slide parameters used in Figure 5.8. The minimal distance to position a tiltmeter near a slide was associated with the distance to the coast. The Alika slide represents the first Alika event, however, the second Alika avalanche exhibited similar features (McMurtry et al. 2004). As the Oshima-Oshima volcanic avalanche was partly subaerial, the distance to the coast is effectively zero. We use a distance between virtual tiltmeter and slide center of 5 km, assuming that the tiltmeter is positioned on the distant side of the island.*

setting of each scenario. For simplification, however, we estimate approximate values: Detectability is guaranteed, if signal to noise ratios are large. Assuming an effective noise level of 20 nrad, signal to noise ratios of at least 10 are reached if tilt amplitudes exceed 200 nrad. We will use this value to approximate T_d.

To determine the invertibility threshold T_i, the inversion routine has to be applied to different tilt amplitudes. We therefore consider a series of scenarios that resemble the Storegga event, but involve different slide volumes. We modify the slide height, while the slide length, width, trajectory, and tiltmeter positions remain identical to the original Storegga scenario. 14 scenarios are considered, with volumes ranging between 165 km³ and 2400 km³. For every setup, we perform 100

inversions, each time with new white noise added to the signals. We consider an inversion successful, if the inverted tsunamigenic potential lies within ±20 % range of the original value. The percentage of successful inversions for each scenario is shown in Figure 5.7A. For small tilts, inversions are not reliable, though with growing size, the number of successful inversions increases rapidly and finally starts to saturate, if maximum tilt signals exceed ~1000 nrad. Generalizing this result, we will use that value from now on as invertibility threshold T_i.

For each scenario, Figure 5.7B depicts the maximum near shore tsunami heights of the virtual gauge at Sula (the gauge closest to the slide, see Figure 5.6). As expected, wave heights grow linearly with the tsunamigenic potential, which in this case depends on the volume only. T_i is exceeded for scenarios that induce more than 2.5 m tsunami amplitude. This means that in the Storegga case, good tsunami predictions based on tilt inversion are possible for all wave heights larger than 2.5 m. Although events with smaller tsunami amplitudes cannot be inverted, they can still be detected. For Storegga-like scenarios, the above discussed detectability threshold of 200 nrad implies the detection of events that induce more than 0.7 m wave amplitude.

Using these values for T_d and T_i, we estimate the scope of our landslide warning tool by applying it to many hypothetical events. For each event we address the question, if the detectability threshold or even the invertibility threshold is exceeded. The ensemble of events is characterized by the fundamental parameters slide volume, travel distance, and distance between slide and tiltmeter. We calculate the tilt amplitudes of numerous scenarios that cover a large range with respect to slide volume (0.1-3000 km³) and travel distance (1-1000 km). We use a simplified geometry, where the slide moves perpendicular to a straight coastline and one tiltmeter is positioned at the nearest coastal point. The slide shape is rotationally symmetrical and self-similar, analog to that described in section 5.2.2. Since the value of the shear modulus should be evaluated at a depth corresponding to the distance between slide and tiltmeter, we linearly approximate the shear modulus as a function of depth in a way that it is $4 \cdot 10^{10}$ Pa and $7 \cdot 10^{10}$ Pa in a depth of 10 km and 100 km, respectively.

For each scenario with given slide volume and travel distance, there exists a distance between tiltmeter and slide start, so that the tilt signal drops below the detectability or invertibility threshold. These distances are depicted as colored lines in Figure 5.8A and 5.8B, respectively. The distance-volume dependency is approximately linear in the double logarithmic plot, thus distance is proportional to volume to the power of a constant. As discussed above, the travel distance has crucial influence on the surface deformation. That is why lines representing long travel distances, e.g. translational slides, are located above lines of small dislocation which represent slumps. For long travel distances and small volumes,
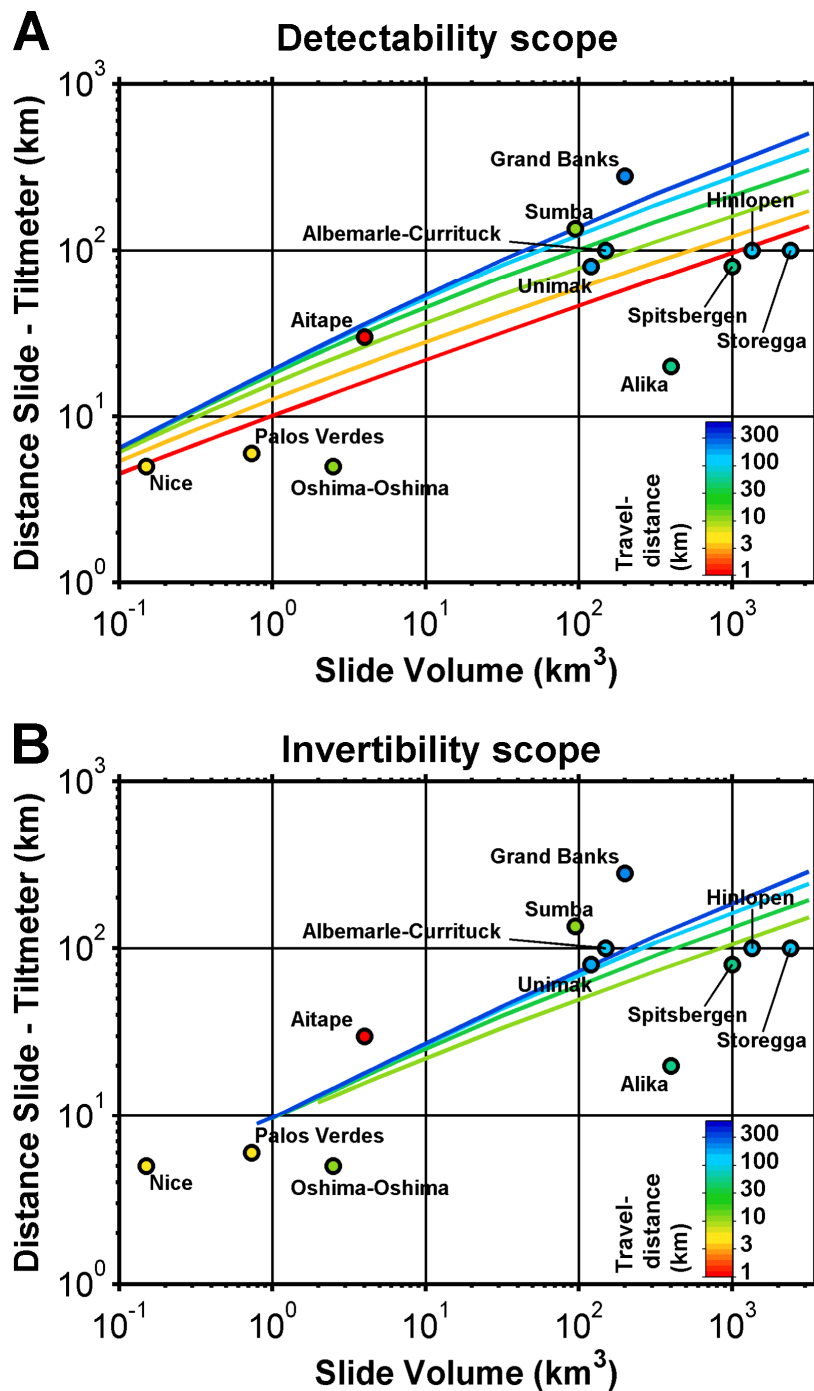
Figure 5.8 *Applicability scope (A) Scope of the detection method (B) Scope of the inversion. Data points depend on three parameters: slide volume, distance between slide center-of-mass to tilt station (nearest coastal point) and travel distance of the slide center (color-coded). Circles designate past or possible events (see Table 5.1). If a circle lies below the curve of corresponding color, the distance between slide and tiltmeter permits to detect/invert the event (Storegga, Hinlopen, Spitsbergen, Alika, Oshima-Oshima, Palos Verdes). Otherwise the distance between slide and coast is too large (Aitape, Grand Banks, Sumba).*

the final deformation does not depend on the dislocation of the slide anymore. Thus curves of big travel distance converge at small volumes. Scenarios that do not produce tilt signals which exceed the required threshold T_d or T_i are not shown.

This is the case in Figure 5.8B, for travel distances that are smaller than 10 km and for small volumes of the order of 1 km³ and below.

We superimpose parameters of historical and possible tsunamigenic landslide events onto Figure 5.8A, depicted as colored circles. Each event is represented by a triplet of data (volume, travel distances and distance to coast), shown in Table 5.1. If the circle lies above the curve of corresponding travel distance, the necessary distance for detection is not reached, and the slide could not have been detected. This is the case for the Aitape event of 1998, for the Grand Banks slide in 1929, as well as for the Sumba slide. If the circle is situated below the corresponding curve, the detection would have been possible, as for the Palos Verdes avalanche, the Oshima-Oshima volcanic landslide of 1741, the Hawaiian Alika debris avalanche, the Unimak event of 1946, as well as the Hinlopen and Storegga slide. The possible Spitsbergen event would be detectable as well. The Nice landslide of 1979 and the Albemarle-Currituck slide off the U.S. mid-Atlantic coast are situated very close to the detection boundary.

Applying the same procedure in Figure 5.8B, we see that the inversion of an event requires a smaller slide-tiltmeter distance than its detection. Inversion is clearly possible for the large tsunamigenic slides of the North Atlantic and Hawaii. Although the Unimak and the Albemarle-Currituck events are detectable, they are probably not invertible. The Nice slide and the Palos Verdes avalanche, due to their small travel distance of several kilometers, did not produce tilt signals larger than T_i.

In this publication, we focus on the remote detection of purely submarine landslides. However, smaller, partly subaerial landslides can be tsunamigenic as well: Corinth Gulf, 1963 (Papadopoulos et al. 2007b), Fatu Hiva, 1999 (Hebert et al. 2002) or Stromboli, 2002 (Maramai et al. 2005). In principle, our technique can be applied for these cases as well, although the distance between slide center and tiltmeter has to be quite small (in the order of 1 km). Our technique is not applicable if the required distance is smaller than a half slide length, as the tiltmeters have to be located outside the failure zone.

5.6 Conclusions
In the present study, we propose a method of using tiltmeters to detect submarine landslides. This is possible during the event, which allows for fast warning of a possible tsunami. Using a numerical modeling technique, we apply this method to the Storegga event, where resulting tilt amplitudes are in the order of several 1000 nrad at the nearest stations. As present day tiltmeter accuracy amounts to several nrad, a landslide of this size would be clearly detectable.

Tilt measurements can be inverted for tsunami relevant parameters. Inversions for the slide tsunamigenic potential (product of volume and maximum velocity) are in good agreement with original data if tiltmeter noise level stays below 50 nrad.

Consequently, inverted landslide parameters can be used to estimate near-coast tsunami wave heights. Tsunami predictions based on the inverted scenarios correspond well to the original tsunami with respect to arrival time and near-shore flow depth. Our inversion technique yields satisfying results for deforming slides as well as for elongated or circular slide geometries. Thus, the tsunami danger of a submarine landslide can be predicted with good accuracy, even if the explicit original geometry is not known.

We elaborate the conditions, under which the detection of submarine mass movements by means of tiltmeters is possible. Past events like the Hinlopen slide, the Storegga event, the Alika slide and the Oshima-Oshima avalanche could have been detected and inverted. In general, longer travel distances leading to larger deformations are favored by our method.

Chapter 6

Conclusions and outlook

6.1. Conclusions

This thesis provides the first detailed study of landslide generated tsunamis in the Sunda Arc off Indonesia. I identified larges slides with volumes reaching 20 km³ southwest of Sumba and comparatively small events off Sumatra. The large slope failures in the eastern part of the Sunda margin might have been facilitated by oversteepening of the slopes, due to subduction erosion.

I modeled the associated tsunamis of nine landslides. Maximal inundation heights reached 7 m at Sumba, more than 5 m at Sumbawa, 3 m at Lombok and 2 m south of Padang. These values designate the potential run-up due to a landslide. If a slide was triggered by an earthquake, run-up values might increase due to the superposition of landslide and earthquake tsunami. The run-up at Bali and Lombok for the discussed events did not exceed 2 m as the source was too far away. However, a worst case scenario consisting of a large slope failure, 250 km off Bali would result in 4 m run-up at Bali and Lombok.

It is a main result of this thesis, that submarine landslides at the Sunda Arc, especially in its eastern part, exhibit a serious potential of tsunami generation. Nevertheless, to estimate future tsunami hazard, the event ages and thus their recurrence rates must be known. The slides off Padang exhibit erosive features which excludes a recent failure. For the other events, the bathymetry data alone is unsuggestive. However, four slides off Sumba lie remarkably close to the epicenter of the tsunamigenic earthquake of 1977 (M_w=8.3). I analyzed the hypothesis of co-seismic landslide triggering during the event. By comparison of measured run-up data and modeling results, however, a relation between a slide and the earthquake could neither be verified, nor excluded.

A spatial hazard assessment was conducted for Padang. It shows the complex interplay of the parameters slide size, water depth, location and slide direction for the generation of dangerous tsunamis. Inside the fore-arc basin, slide volumes must exceed 0.5 km³ in proximity to Padang and 10 km³ for most parts of the basin to induce more than 2 m run-up. Outside the basin, volumes smaller than 25 km³ do not pose a danger for Padang.

In the second study area, the Atlantic of northwestern Europe, landslide volumes are more than one order of magnitude larger than in the Sunda Arc. This is caused by the efficient sediment supply during stadials. The geologic situation of the Kongsfjorden Trough Mouth Fan west of Spitsbergen is comparable to that of the Storegga slide area before the failure: Large quantities of sediments exist, where marine clays are inter-layered with glacial deposits. Further, the presence of active fluid flow systems and gas hydrates have been shown. Arctic warming might facilitate slope failure by several mechanisms: First, the melting of glaciers unloads the crust. This induces isostatic rebound leading to possibly significant earthquakes. Second, increased oceanic bottom temperatures melt gas hydrates and thus destabilize the slope.

According to my simulations, a large slide into the Fram Strait could generate tsunamis with near shore wave heights of about 6 m in Norway, 4 m at northern Iceland and 3 m at the Faroer and Shetland Islands. A smaller scenario yields 3 m, 2 m and 1 m at the respective locations. These wave heights could increase significantly upon run-up, especially in fjords. Slide volume, velocity and direction are shown to be main controlling parameters.

In this thesis, I proposed a new method of using tiltmeters to detect submarine landslides: Mass movements of the investigated size will induce a noticeable deformation of the earth's surface. Using the elastic half-space approximation, I estimated a tilt amplitude of at least 1000 nrad for each considered Spitsbergen scenario. Compared to present day tiltmeter accuracies of 1 nrad, the signal will be clearly detectable, as long as the surrounding noise is reduced by appropriate low-pass filtering.

I introduced an inversion routine which, based on an array of tiltmeters, computes location and tsunamigenic potential (product of volume and maximal velocity) of a landslide. This is possible during the event, which allows for fast warning of a possible tsunami. I tested the routine by applying it to the Storegga event. The inversion yields good results for solid and deforming mass movements as well as for elongated and circular slide shapes.

The inversion technique is applicable as long as effective noise amplitudes do not exceed 50 nrad. Thereby, the effective noise designates the residual perturbation of the tilt signal after subtraction of calculable signals like solid earth tides, and filtering for the low frequency domain. Tsunami calculations based on the inverted landslide parameters are shown to be in good correspondence to input scenario. Thus, even if the explicit original landslide geometry is not known, the tsunami of a submarine mass movement can be predicted with good accuracy.

I applied the inversion technique to historic tsunamigenic landslide events worldwide. Detection and inversion is possible for large events close to the coast

like Storegga, Hinlopen, Alika and the hypothetical Spitsbergen slide. I suggest that the installation of tiltmeters would be a valuable tool in future tsunami early warning systems.

6.2 Outlook

This study provides estimations of subrecent landslide-induced tsunami run-up for Indonesian communities at the Indian Ocean. I thereby applied a set of semi-empirical formulas for tsunami generation by slumps and a shallow water model to calculate wave propagation. The next step will be to model the tsunami generation in very deep water directly and with higher accuracy. Therefore, more advanced wave propagation codes like Reynolds averaged Navier-Stokes models (Yuk et al. 2006) or potential flow models (Grilli et al. 2002) are needed.

In this thesis, large translational mudflows like Storegga, and the hypothetical Spitsbergen slide have been modeled as moving solid bodies. Next, I take into account rheological slide properties. Viscoplastic qualities can be implemented into mudflow dynamics using the Bingham model (De Blasio et al. 2005). It introduces viscosity and yield strength, so that the material does not flow as long as the yield strength exceeds the applied shear stress. The numerical model of Imran et al. (2001) includes this property, but also comprises shear thinning and shear thickening, where the viscosity is a function of the shear rate. Reproducing the Storegga slide with more accuracy will provide better input for tsunami modeling, but will be especially interesting with respect to the inversion of tilt data.

Tiltmeter predictions that I effectuated under the assumption of an elastic half-space will be improved when a layered earth model is considered. In this case, however, the analytic solutions will have to be replaced by a numerical model. This will strongly affect calculation times and might impede a real-time inversion.

The efficiency of tiltmeters for the detection of submarine landslides strongly depends on the ability to exclude surrounding noise. The implementation of a tiltmeter at a specific site, for instance at Spitsbergen, could be used to evaluate the noise and to test noise reduction techniques. Finally, it might be promising to explore the possibility of using arrays of broad-band seismometers to detect large submarine landslides.

71

References

Arvidsson R (1996) Fennoscandian earthquakes: Whole crustal rupturing related to postglacial rebound. Science 274(5288):744-746, doi:710.1126/science.1274.5288.1744

Assier-Rzadkiewicz S, P Heinrich, PC. Sabatier, B Savoye and JF Bourillet, (2000), Numerical Modelling of a Landslide-generated Tsunami: The 1979 Nice Event, Pure Appl Geophys., 157:1707–1727

Baptista MA., S Heitor, JM Miranda, P Miranda, L Mendes Victor (1998) The 1755 Lisbon tsunami; evaluation of the tsunami parameters. J Geodyn. 25(1-2):143-157

Barrientos SE, SN Ward (1990) The 1960 Chile earthquake: inversion for slip distribution from surface deformation. Geophys J Int. 103:589-598

Bondevik S, F Løvholt, C Harbitz, J Mangerud, A Dawson, JI Svendsen (2005) The Storegga Slide tsunami - comparing field observations with numerical simulations. Mar Petrol Geol. 22:195–208

Borrero JC, Synolakis, CE, and Fritz, H (2006) Northern Sumatra field survey after the December 2004 Great Sumatra earthquake and Indian Ocean tsunami, Great Sumatra Earthquakes and Indian Ocean Tsunamis of December 26, 2004 and March 28, 2005. Earthq Spectra. 22

Boussinesq JV (1878) Équilibre d'élasticité d'un sol isotrope sans pesanteur, supportant différents poids. CR Math. Acad. Sci. Paris. 86:1260-1263

Bryn P, K Berg, CF Forsberg, A Solheim, TJ Kvalstad (2005) Explaining the Storegga Slide. Mar Petrol Geol. 22:11–19

Bugge T, S Befring, RH Belderson, T Eidvin, E Jansen, NH Kenyon, H Hoitedahi, HP Sejrup (1987) A Giant Three-Stage Submarine Slide Off Norway. Geo-Mar Lett. 7:191-198

Bünz S, J Petersen, S Hustoft, J Mienert (2008) Environmentally-sensitive gas hydrates on the W-Svalbard margin at the gateway to the Arctic Ocean, paper presented at Proceedings of the 6th International Conference on Gas Hydrates (ICGH 2008) July 6-10, Vancouver, British Columbia, Canada

Chesley SR, SN Ward (2006) A Quantitative Assessment of the Human and Economic Hazard from Impact-generated Tsunami. Nat Hazards. 38:355–374

Chlieh M, JP Avouac, K Sieh, DH Natawidjaja, J Galetzka (2008) Heterogeneous coupling of the Sumatran megathrust constrained by geodetic and paleogeodetic measurements. J Geophys Res. Doi:10.1029/2007JB004981

De Blasio FV, A Elverhøi, D Issler, CB Harbitz, P Bryn, R Lien (2005) On the dynamics of subaqueous clay rich gravity mass flows - the giant Storegga slide, Norway. Mar Petrol Geol. 22:179–186

D'Oreye NF, W Zürn (2005) Very high resolution long-baseline water-tube tiltmeter to record small signals from Earth free oscillations up to secular tilts. Rev Sci Instrum. 76:024501

Driscoll NW, JK Weissel, JA Goff (2000) Potential for large-scale submarine slope failure and tsunami generation along the U.S. mid-Atlantic coast. Geology 28(5):407–410

Ekström G, M Nettles, GA Abers (2003) Glacial earthquakes. Science 302(5654):622-624.

Eva C, M Cattaneo, F Merlanti (1988) Seismotectonics of the central segment of the Indonesian Arc. Tectonophys. 146:241-259

Fine IV, AB Rabinovich, BD Bornhold, RE Thomson, EA Kulikov (2005) The Grand Banks landslide-generated tsunami of November 18, 1929: preliminary analysis and numerical modeling. Mar Geol. 215:45-57

Fritz H, W Kongko, A Moore, B McAdoo, J Goff, C Harbitz, B Uslu, N Kaligeris, V Titov, CE Synolakis (2007) Extreme run-up from the 17 July 2006 Java tsunami. Geophys Res Abstr. 9, 10765

Gebauer A, T Jahr, G Jentzsch (2007) Recording and interpretation/analysis of tilt signals with five ASKANIA borehole tiltmeters at the KTB. Rev Sci Instrum. 78:054501

Grilli ST, P Watts (1999) Modeling of waves generated by a moving submerged body. Applications to underwater landslides. Eng Anal Bound Elem. 23:645–656

Grilli ST, S Vogelmann, P Watts (2002) Development of a 3D numerical wave tank for modeling tsunami generation by underwater landslides. Eng Anal Bound Elem. 26(4):301-313

Grilli ST, M ASCE, Watts, P (2005) Tsunami generation by submarine mass failure Part I: Modeling, Experimental Validation, and Sensitivity Analyses. J Waterway Port Coastal and Ocean Eng. 131(6):283-297

Haflidason H, HP Sejrup, A Nygård, J Mienert, P Bryn, R Lien, CF Forsberg, K Berg, D Masson (2004) The Storegga Slide: architecture, geometry and slide-development. Mar Geol. 213:201-234

Haflidason H, R Lien, HP Sejrup, CF Forsberg, PBryn (2005) The dating and morphometry of the Storegga Slide. Mar Petrol Geol. 22(1-2):123–136

Hall R (1997) Cenozoic plate tectonic reconstructions of SE Asia. Geological Society Special Publications 126:11-23.

Hamilton EL (1985) Sound velocity as a function of depth in marine sediments. J Acoust Soc Am. 78(4):1348-1355

Hampton MA, HJ Lee, J Locat (1996) Submarine landslides. Rev Geophys. 34:33-59

Hamzah L, NT Puspito, F Imamura (2000) Tsunami Catalog and Zones in Indonesia. J Nat Disaster Sci. 22(1):25-43

Harbitz CB (1992) Model simulations of tsunamis generated by the Storegga slides. Mar Geol. 105(1-4):1-21

Hébert H, A Piatanesi, P Heinrich, and F Schindelé (2002) Numerical modeling of the September 13, 1999 landslide and tsunami on Fatu Hiva Island (French Polynesia). Geophys Res Lett. 29(10):1484

Heine C, RD Müller and C Gaina (2004), Reconstructing the lost Thethys Ocean basin: Convergence history of the SE Asian margin and marine gateways. In: P Clift, P Wang, W Kuhnt and D Hayes (eds) Geophysical Monograph Series Vol 149: Continent-Ocean interactions within East Asian marginal seas, AGU, Washington DC, pp 37-54

Hoechner A, AY Babeyko, SV Sobolev (2008) Enhanced GPS inversion technique applied to the 2004 Sumatra earthquake and tsunami. Geophys Res Lett. 35, L08310, doi:10.1029/2007GL033133

Hornbach MJ, LL Lavier, CD Ruppel (2007) Triggering mechanism and tsunamogenic potential of the Cape Fear Slide complex, U.S. Atlantic margin. Geochem Geophys Geosys. 8 doi:10.1029/2007GC001722.

Hornbach MJ, SA Mondziel, NR Grindlay, C Frohlich, P Mann (2008) Did a submarine slide trigger the 1918 Puerto Rico tsunami? J Sci Tsunami Hazards. 27(2)

Imamura F, MMA Imteaz (1995) Long waves in two-layers: Governing equations and numerical model. J Sci Tsunami Hazards. 13:3-24

Imamura F, N Shuto, C Goto, Y Ogawa, (1997) IUGG/IOC Time Project IOC Manuals and Guides No.35, (UNESCO)

Imran J, P Harff, G Parker (2001) A numerical model of submarine debris flow with graphical user interface. Comp Geosci. 27:717–729

Imamura F, AC Yalciner, G Ozyurt (2006) Tsunami modelling manual. www.tsunami.civil.tohoku.ac.jp

IOC, IHO and BODC (2003) Centenary Edition of the GEBCO Digital Atlas, British Oceanographic Data Centre, Liverpool

ITDB/WLD (2007) Integrated Tsunami Database for the World Ocean, Version 6.51 of February 20, 2007. CD-ROM, Tsunami Laboratory, ICMMG SD RAS, Novosibirsk, Russia

ITIC (International Tsunami Information Center), Tsunami reports No. 1977-12

Kato K, Y Tsuji (1995) Tsunami of the Sumba earthquake of August 19, 1977. J Nat Disaster Sci. 17(2):87-100

Kattsov VM, E Källén, H Cattle, J Christensen (2004) Future climate change: Modeling and scenarios for the Arctic, in Arctic Climate Impact Assessment, edited, pp. 99-150, Cambridge University Press, Cambridge.

Knies J, E Damm, J Gutt, U Mann, L Pinturier (2004) Near-surface hydrocarbon anomalies in shelf sediments off Spitsbergen: Evidences for past seepages. Geochem Geophys Geosyst. 5 doi:10.1029/2003GC000687

Kopp H, N Kukowski (2003) Backstop geometry and accretionary mechanics of the Sunda margin. Tectonics 22(6):1072.

Kopp H, ER Flueh, CJ Petersen, W Weinrebe, A Wittwer, Meramex Scientists (2006) The Java margin revisited: Evidence for subduction erosion off Java. Earth Planet Sci Lett. 242:130–142

Krüger F, M Ohrberger (2005) Tracking the rupture of the Mw 5 9.3 Sumatra earthquake over 1,150 km at teleseismic distance. 435 doi:10.1038/nature03696

Kukowski N, A Hampel, S Hoth, J Bialas (2008) Morphotectonic and morphometric analysis of the Nazca plate and the adjacent offshore Peruvian continental slope - Implications for submarine landscape evolution. Mar Geol. 254:107-120

Kvalstad TJ, L Andresen, CF Forsberg, K Berg, P Bryn, M Wangen (2005) The Storegga slide: evaluation of triggering sources and slide mechanics. Mar Petrol Geol. 22(1-2):245-256

Laberg JS, TO Vorren (1993) A Late Pleistocene submarine slide on the Bear Island Trough Mouth Fan. Geo-Mar Lett. 13:227-234

Laberg JS, TO Vorren, JA Dowdeswell, NH Kenyon, J Taylor (2000) The Andøya Slide and the Andøya Canyon, north-eastern Norwegian-Greenland Sea. Mar Geol. 162:259-275

Laberg JS, TO Vorren, J Mienert, P Bryn, R Lien (2002) The Trænadjupet Slide: a large slope failure affecting the continental margin of Norway 4,000 years ago. Geo-Mar Lett. 22:19–24

Lagarias JC, JA Reeds, MH Wright, PE Wright (1998) Convergence Properties of the Nelder-Mead Simplex Method in Low Dimensions. SIAM J Optim. 9(1):112-147

Lavigne F, C Gomez, M Giffo, P Wassmer, C Hoebreck, D Mardiatno, J Prioyono, R Paris (2007) Field observations of the 17 July 2006 Tsunami in Java. Nat Hazards Earth Syst Sci. 7:177–183

Lindberg B, JS Laberg, TO Vorren (2004) The Nyk Slide-morphology, progression, and age of a partly buried submarine slide offshore northern Norway. Mar Geol. 213(1-4):277-289

Locat J, HJ Lee, P Locat, J Imran (2004) Numerical analysis of the mobility of the Palos Verdes debris avalanche, California, and its implication for the generation of tsunamis. Mar Geol. 203:269-280

Lomax A, A Michelini, A Piatanesi (2007) An energy-duration procedure for rapid determination of earthquake magnitude and tsunamigenic potential.Geophys J Int. 170:195-1209

Lorito S, F Romano, A Piatanesi, E Boschi (2008) Source process of the September 12, 2007, MW 8.4 southern Sumatra earthquake from tsunami tide gauge record inversion. Geophys Res Lett. Doi:10.1029/2007GL032661

Løvholt F, CB Harbitz, KB Haugen, (2005), A parametric study of tsunamis generated by submarine slides in the Ormen Lange/Storegga area off western Norway, Mar. Petrol. Geol., 22, 219–231

Lüschen E, C Müller, H Kopp, M Engels, R Lutz, L Planert, A Shulgin, YS Djajadihardja (2009) Structure, Evolution and Tectonic Activity of the Eastern Sunda Forearc, Indonesia, from Marine Seismic Investigations. Submitted

Luthcke SB, HJ Zwally, W Abdalati, DD Rowlands, RD Ray, RS Nerem, FG Lemoine, JJ McCarthy, DS Chinn (2006) Recent Greenland ice mass loss by drainage system from satellite gravity observations. Science. 314(5803):1286-1289; DOI: 1210.1126/science.1130776

Lynett P, PLF Liu (2002) A numerical study of submarine-landslide-generated waves and run-up. Proc R Soc A. 458:2885

Lynett PJ, JC Borerro, PLF Liu, and CE Synolakis (2003) Field Survey and Numerical Simulations: A Review of the 1998 Papua New Guinea Tsunami. Pure Appl Geophys. 160:2119–2146

Lynett P, PLF Liu (2005) A numerical study of the run-up generated by three-dimensional landslides. J Geophys Res. Doi: 10.1029/2004JC002443

Lynnes CS, T Lay (1988) Source Process of the Great 1977 Sumba Earthquake. J Geophys Res. 93(Bll):13,407-13,420

Maramai A, L Graziani, G Alessio, P Burrato, L Colini, L Cucci, R Nappi, A Nardi, G Vilardo (2005) Near- and far-field survey report of the 30 December 2002 Stromboli (Southern Italy) tsunami. Mar Geol. 215:93-106

Masson DG, LM Parson, J Milsom, G Nichols, N Sikumbang, B Dwiyanto, H Kallagher (1990) Subduction of seamounts at the Java Trench: a view with long-range sidescan sonar. Tectonophys. 185:51– 65

Masson DG, CB Harbitz, RB Wynn, G Pedersen, F Løvholt (2006) Submarine landslides: processes, triggers and hazard prediction. Phil. Trans R Soc A. 364:2009-2039

Matlab Version 7.1, Copyright 1984-2005, The MathWorks, Inc.

Matsumoto T (2007) An underwater landslide or slump on an active submarine fault - A possible source of a devastating tsunami? Eos Trans AGU. 88(52), Fall Meet. Suppl., Abstract S53A-1018

McAdoo BG, LF Pratson, DL Orange (2000) Submarine landslide geomorphology, US continental slope. Mar Geol. 169 (2000):103–136

McAdoo B, G Simpson (2005) Morphometric dating of submarine landslide scarps. Geophys Res Abstr 7, Abstract 00629

McCarthy D, and Petit G (eds). (2004). IERS Conventions (2003). IERS Technical Note No 32, Verlag des Bundesamts für Kartographie und Geodäsie, Frankfurt am Main, 127 pp

McCloskey J, A Antonioli, A Piatanesi, K Sieh, S Steacy, S Nalbant, M Cocco, C Giunchi , JD Huang, P Dunlop (2008) Tsunami threat in the Indian Ocean from a future megathrust earthquake west of Sumatra. Earth Planet Sci Lett. 265:61-81

McMurtry GM, P Watts, GJ Fryer, JR Smith, F Imamura (2004) Giant landslides, mega-tsunamis, and paleo-sea level in the Hawaiian Islands. Mar Geol. 203:219-233

Melchior P (1966), The Earth Tides, Pergamon Press, Oxford.

Micallef A, DG Masson, C Berndt, DAV Stow (in press), Development and mass movement processes of the north-eastern Storegga Slide, Quatern. Sci. Rev..

Moran K, D Tappin (2006) SEATOS 2005 Cruise Report: Sumatra Earthquake and Tsunami Off shore Survey (SEATOS). 92 pp. (Online) available at http://ocean.oce.uri.edu/seatos.

Müller C, H Kopp, YS Djajadihardja, U Barckhausen, Ehrhardt A, Engels M, Flueh ER, Gaedicke C, Keppler H, Lutz R, Lüschen E, Neben S, Seeber L, Dzulkarnaen DPS (2008) From subduction to collision; The Sunda-Banda Arc transition. Eos, Transactions, American Geophysical Union 89:49-50

Natawidjaja DH, K Sieh, M Chlieh, J Galetzka, BW Suwargadi, H Cheng, RL Edwards, JP Avouac, SN Ward (2006) Source parameters of the great Sumatran megathrust earthquakes of 1797 and 1833 inferred from coral microatolls. J Geophys Res Solid Earth. Doi:10.1029/2005JB004025

Neben S, C Gaedicke (2006) Cruise Report, BGR Cruise SO189 Leg 1, Project SUMATRA, The Hydrocarbon System of the Sumatra Forearc, Bundesanstalt für Geowissenschaften und Rohstoffe, 126 pp

Normark WR, M McGann, R Sliter (2004) Age of Palos Verdes submarine debris avalanche, southern California. Mar Geol. 203:247-259

Okada Y (1985) Surface deformation due to shear and tensile faults in a half-space. Bull Seism Soc Am. 75(4):1135-1154

Okal EA (2003) T Waves from the 1998 Papua New Guinea Earthquake and its Aftershocks: Timing the Tsunamigenic Slump. Pure Appl Geophys. 160:1843–1863

Okal EA, CE Synolakis (2003) A Theoretical Comparison of Tsunamis from Dislocations and Landslides. Pure Appl Geophys. 160:2177–2188

Okal EA., G Plafker, CE Synolakis, JC Borrero (2003) Near-Field Survey of the 1946 Aleutian Tsunami on Unimak and Sanak Islands. Bull Seism Soc Am. 93(3):1226–1234

Papadopoulos GA, F Imamura (2001) A proposal for a new tsunami intensity scale, ITS 2001 Proceedings, Session 5, Number 5-1

Papadopoulos GA, E Daskalaki, A Fokaefs, (2007a), Tsunamis generated by coastal and submarine landslides in the Mediterranean Sea, in: Submarine Mass Movements and Their Consequences, Adv Nat Tech Hazards Res., vol 27, edited by V Lykousis, D Sakellariou, J Locat, Springer, Dordrecht, pp 327-336

Papadopoulos GA, LI Lobkovsky, RK Mazova, IA Garagash, V Karastathis, LY Kataeva, VG Kaz'min (2007b) Numerical Modeling of Sediment Mass Sliding and Tsunami Generation: The Case of February 7, 1963, in Corinth Gulf, Greece. Mar Geodesy. 30(4):315-331

Pelinovsky E (2001) Analytical Models Of Tsunami Generation By Submarine Landslides. In: AC Yalçiner, E Pelinovsky, E Okal, C E Synolakis (eds) Submarine Landslides and Tsunamis, 2003 Kluwer Academic Publishers, pp 111-128

Pelinovsky E, Kurkin A, Zaytsev A, Yalciner A, Imamura F (2006) AVI-NAMI Version 1.2

Rignot E and P Kanagaratnam (2006) Changes in the velocity structure of the Greenland Ice Sheet. Science. 311:986-990, DOI: 10.1126/science.1121381

Rynn J (2002) A preliminary assessment of tsunami hazard and risk in the Indonesian region. Sci Tsunami Hazard. 20(4):193

Satake K (1988) Effects of Bathymetry on Tsunami Propagation: Application of Ray Tracing to Tsunamis. Pure Appl Geophys. 126(1):27-36

Satake K, Y Kato (2001) The 1741 Oshima-Oshima Eruption: Extent and Volume of Submarine Debris Avalanche. Geophys Res Lett. 28(3):427-430

Sato T, J Okuno, J Hinderer, DS MacMillan, HP Plag, O Francis, R Falk, Y Fukuda (2006) A geophysical interpretation of the secular displacement and gravity rates observed at Ny-Ålesund, Svalbard in the Arctic; effects of post-glacial rebound and present-day ice melting. Geophys J Intern. 165(3):729-743

Schlueter HU, C Gaedicke, HA Roeser, B Schreckenberger, H Meyer, C Reichert, Y Djajadihardja, A Prexl (2002) Tectonic features of the southern Sumatra-western Java forearc of Indonesia. Tectonics 21(5):15.

Simons WJF, A Socquet, C Vigny, BAC Ambrosius, S Haji Abu, C Promthong, C Subarya, DA Sarsito, S Matheussen, P Morgan, W Spakman (2007) A decade of GPS in Southeast Asia: Resolving Sundaland motion and boundaries. J Geophys Res 112.

Sobolev SV, AY Babeyko, R Wang, A Hoechner, R Galas, M Rothacher, DV Sein, J. Schröter, J Lauterjung, C Subarya (2007) Tsunami early warning using GPS-Shield arrays. J Geophys Res. 112 B08415, doi:10.1029/2006JB004640

Solheim A, P Bryn, HP Sejrup, J Mienert, K Berg (2005a) Ormen Lange - an integrated study for the safe development of a deep-water gas field within the Storegga Slide Complex, NE Atlantic continental margin; executive summary. Mar Petrol Geol. 22:1–9

Solheim A, K Berg, CF Forsberg, P Bryn (2005b) The Storegga Slide complex: repetitive large scale sliding with similar cause and development. Mar Petrol Geol. 22(1-2):97-107.

Spence W (1986) The 1977 Sumba Earthquake Series: Evidence for Slab Pull Force Acting at a Subduction Zone. J Geophys Res. 91:7225-7239

Stein, S, EA Okal (2005) Size and speed of the Sumatra earthquake. Nature 434:581

Sultan N, P Cochonat, JP Foucher, J Mienert (2004) Effect of gas hydrate melting on seafloor slope instability. Mar Geol. 213(1-4):379-401

Turpeinen H, A Hampel, T Karow, G Maniatis (2008) Effect of ice sheet growth and melting on the slip evolution of thrust faults. Earth Planet Sci Lett. 269(1-2):230-241

Susilohadi S, C Gaedicke and A Ehrhardt (2005) Neogene structure and sedimentation history along the Sunda forearc basins off southwest Sumatra and southwest Java Marine Geology. Mar Geo. Doi: 10.1016/j.margeo.2005.05.001.

Sweet S, and EA Silver (2003) Tectonics and Slumping in the Source Region of the 1998 Papua New Guinea Tsunami from Seismic Reflection Images. Pure Appl Geophys. 160:1945–1968

Synolakis CE, JP Bardet, JC Borrero, HL Davies, EA Okal, EA Silver, S Sweet and DR Tappin (2002) The slump origin of the 1998 Papua New Guinea Tsunami. Proc R Soc Lond A. 458:763–789

Synolakis CE, L Kong (2006) Runup Measurements of the December 2004 Indian Ocean Tsunami. Earthq Spectr. 22(S3):S67–S91

Tappin DR, T Matsumoto, P Watts, K Satake, GM McMurtry, M Matsuyama, Y Lafoy, and Y Tsuji (1999) Sediment slump likely caused 1998 Papua New Guinea tsunami. Eos Trans AGU. 80(30):329

Tappin DR, P Watts, GM McMurtry, Y Lafoy, T Matsumoto (2001) The Sissano, Papua New Guinea tsunami of July 1998-offshore evidence on the source mechanism. Mar Geol. 175:1-23

Tappin DR, LC McNeil, T Henstock, D Mosher (2007) Mass wasting processes - offshore Sumatra. In: V Lykousis, D Sakellariou, J Locat (eds) Advances in Natural and Technological Hazards Research Vol 27: Submarine Mass Movements and Their Consequences, Springer, Dordrecht, pp 327-336

Tinti S, E Bortolucci, C Vannini (1997) A Block-Based Theoretical Model Suited to Gravitational Sliding. Nat Hazards. 16:1–28

Tinti S, A Maramai, L Graziani (2004) The new catalogue of Italian tsunamis Source. Nat Hazards. 33(3):439-465

Trifunac MD, MI Todorovska (2002) A note on differences in tsunami source parameters for submarine slides and earthquakes. Soil Dyn Earthq Eng. 22:143:155

Trifunac MD, A Hayir, MI Todorovska (2002) Was Grand Banks event of 1929 a slump spreading in two directions? Soil Dyn Earthq Eng. 22:349:360

Tsuji Y, F Imamura, H Matsutomi, CE Synolakis (1995a) Field Survey of the East Java Earthquake and Tsunami of June 3, 1994. Pure Appl Geophys. 144(3/4):839

Tsuji Y, H Matsutomi, F Imamura, M Takeo (1995b) Damage to Coastal Villages due to the 1992 Flores Island Earthquake Tsunami. Pure Appl Geophys. 144(3/4):481

Tsuji Y, Y Namegaya, H Matsumoto, SI Iwasaki, W Kanbua, M Sriwichai, V Meesuk (2006) The 2004 Indian tsunami in Thailand: Surveyed runup heights and tide gauge records. Earth Planet Space. 58:223-232

UHSLC (University of Hawai, Sea Level Center) 2008 http://ilikai.soest.hawaii.edu/

van der Werff W (1995) Structure and morphotectonics of the accretionary prism along the Eastern Sunda-Western Banda Arc. J Southeast Asian Earth Sci. 11:309-322

Vanneste M, S Guidard, J Mienert (2005) Bottom-simulating reflections and geothermal gradients across the western Svalbard margin. Terra Nova. 17(6):510-516.

Vanneste M, J Mienert, S Bünz (2006) The Hinlopen Slide: A giant, submarine slope failure on the northern Svalbard margin, Arctic Ocean. Earth Planet Sci Lett. 245(1-2):373–388

Ward SN (2001) Landslide tsunami. J Geophys Res.,106(6):11,201-11,215

Ward SN, E Asphaug (2003) Asteroid impact tsunami of 16 March, 2880. Geophys J Int. 153:F6–F10

Watts P, ST Grilli, JT Kirby, GJ Fryer, and DR Tappin (2003) Landslide tsunami case studies using a Boussinesq model and a fully nonlinear tsunami generation model. Nat Hazards Earth Sys Sci. 3:391-402

Watts P, ST Grilli, DR Tappin, GJ Fryer (2005) Tsunami Generation by Submarine Mass Failure. I: Modeling, Experimental Validation, and Sensitivity Analyses. J Wtrwy Port Coast Oc Eng. 131:283

Wells DL, KJ Coppersmith (1994) New Empirical Relationships among Magnitude, Rupture Length, Rupture Width, Rupture Area, and Surface Displacement. Bull Seism Soc Am. 84(4):974-1002

Westbrook GK, S Chand, G Rossi, C Long, S Bünz, A Camerlenghi, JM Carcione, S Dean, JP Foucher, E Flueh, D Gei, RR Haacke, G Madrussani, J Mienert, TA Minshull, H Nouzé, S Peacock, TJ Reston, M Vanneste, M Zillmer (2008a) Estimation of gas hydrate concentration from multi-component seismic data at sites on the continental margins of NW Svalbard and the Storegga region of Norway. Mar Petrol Geol. 25(8):744-758

Westbrook GK, Minshull T, Berndt C, R James, H Paelike, E Rohling, A Chabert, R Fisher, D Green, V Huehnerbach, M Lanoiselle, K Thatcher, A Burchell, A Piotrowski, A Aquilina, A Crocker, C Bolton, A Osbourne (2008b) Active gas Venting at the Landward Limit of Hydrate Stability Offshore Svalbard. Eos Trans. AGU, 89(53), Fall Meet. Suppl., Abstract OS31D-03

Winkelmann D, W Jokat, F Niessen, R Stein, A Winkler (2006) Age and extent of the Yermak Slide north of Spitsbergen, Arctic Ocean. Geochem Geophys Geosys. 7(6) doi:10.1029/2005GC001130

Yalçiner AC, E Pelinovsky, E Okal, CE Synolakis (2003) Submarine Landslides and Tsunamis. NATO Sci Ser. Ser. IV, vol. 21, 327 pp. Kluwer Acad., Norwell, Mass.

Yuk D, SC Yim, PLF Liu (2006) Numerical modeling of submarine mass-movement generated waves using RANS model. Comput Geosci. 32:927–935

List of figures

List of tables